INSTITUT DE MICROTECHNIQUE
UNIVERSITÉ DE NEUCHÂTEL

Integration of Organic Optoelectronic Devices for Biosensing Applications

Thèse présentée à la faculté des sciences
Institut de Microtechnique
Université de Neuchâtel

Pour l'obtention du grade de docteur ès sciences

Par

Marc Ramuz

Acceptée sur proposition du jury :

Prof. Peter Seitz, directeur de thèse

Prof. Hans Peter Herzig, Prof. Philipp Aebi,

Prof. Beat Ruhstaller, rapporteurs

Soutenue le 11 Décembre 2009

Université de Neuchâtel

Université de Neuchâtel

FACULTE DES SCIENCES
Secrétariat-Décanat de la faculté
- Rue Emile-Argand 11
- CP 158
- CH-2009 Neuchâtel

IMPRIMATUR POUR LA THESE

Integration of organic optoelectronic devices for biosensing application

Marc RAMUZ

UNIVERSITE DE NEUCHATEL

FACULTE DES SCIENCES

La Faculté des sciences de l'Université de Neuchâtel,
sur le rapport des membres du jury

MM. P. Seitz, directeur de thèse (UniNe et IMT-EPFL),
H.P. Herzig (UniNe et IMT-EPFL), P. Aebi (Université de Fribourg)
et B. Ruhstaller (ZHAW-HES, Winterthur)

autorise l'impression de la présente thèse.

Neuchâtel, le 14 décembre 2009

Le doyen :
F. Kessler

UNIVERSITE DE NEUCHATEL
FACULTE DES SCIENCES
Secrétariat - décanat de la faculté
Rue Emile-Argand 11 - CP 158
CH-2009 Neuchâtel

■ Téléphone : +41 32 718 21 00 ■ E-mail : secretariat.sciences@unine.ch ■ www.unine.ch/sciences

To my family

Preface

This work presents the application of organic optoelectronics devices for sensing application. The following thesis is the result of my research at the "Centre Suisse d'Electronique et de Microtechnique" (CSEM), in the Zurich and Basel center, within the polymer optoelectronic group. Of course, this work could not have been done without the great support of many persons that I wish to warmly and sincerely thank.

Many thanks go to Prof. Dr. Peter Seitz, Professor at the IMT in Neuchâtel and head of the CSEM Nanomedecine division in Landquart, for advising my thesis and for helpful discussions.

I would like to acknowledge the support, guidance and professionalism offered to me by my supervisors Dr. Lukas Bürgi and Dr. David Leuenberger. Their good, optimistic and helpful temperament allowed me to strive for excellence. They were always present to help me in case of need and I benefited a lot from them. I owe a particular thank to Dr. L. Bürgi who introduced me to the field of organic electronic. His impressive knowledge and know-how in this domain provided the basis of many results show in this thesis.

I also would like to acknowledge Dr. Carsten Winnewisser for giving me the opportunity to work at CSEM, for receiving me well in his group and for his positive attitude towards my work. I would like to thank our new group leader – Dr. Giovanni Nisato – who encouraged and supported me in the difficult phase of the writing and correcting of the thesis manuscript.

I would like to thank all my group colleagues of the polymer optoelectronic group during the last years. Especially I thank:

- Reto Pfeiffer for his various help ranging from electronic design to device fabrication.
- Tilman Beierlein and Adrian Von Mühlenen for their support in the area of programming and computation. I also acknowledge them for general discussions concerning the field of organic electronic.
- Mario Mücklich, Bernhard Blöchliger and Jürg Schleuniger for their collaboration done within the laboratory.
- Michael Kiy, Neeraj Adsul, Marek Chrapa, Zbigniew Szamel and Ton Offerman for the fruitful discussion we had.
- Many thanks to Guillaume Basset who always gave precise and valuable advices.

I also thank all the colleagues of the Photonics division, especially Marc Schnieper, M'Hamed Ali El Mechat, Sebastien Mader, Christian Zschokke, Laurent Davoine for the great time I spent with them either during ski session or around a good meal.

I would like to acknowledge all CSEM employees for the friendly climate which prevails in this laboratory. I will certainly miss a lot this great atmosphere together with the excellent working conditions within CSEM.

I appreciated my colleagues from the European project SEMOFS, which was a stimulating and a good framework for this thesis. I particularly thank Guy Voirin and Rino Kunz for their collaboration linked to the use of the biological compounds.

Finally I would like to thank my friends, my family and in particular my wife and my son for supporting my work in many ways, e.g. for the moral support, patience and encouragement during the last four years.

Marc Ramuz

Basel, December 2009

Contents

Abstract

The integration of organic optoelectronic devices – such as polymer light emitting diodes (PLEDs) and polymer photodiodes (PPDs) – onto a biochip is investigated. The biochip consists of a glass substrate, a planar single-mode waveguide and an optical grating to out-couple the guided light. Solution-processing of organic electronic devices allow to deposit PLEDs and PPDs by additive processes such as ink-jet printing, for example. This processing is compatible with roll-to-roll production and could contribute to the cost-effective fabrication of miniaturized biosensors.

Evanescent coupling is used to couple light from an organic Lambertian emitter into the single-mode waveguide. Either a PLED is deposited right on top of the waveguide; or a PLED – located on the backside of the substrate – pumps a photoluminescent (PL) material layer located directly on top of the waveguide.

In the first configuration, due to the waveguide's proximity, the emission zone of the PLED and the waveguide mode overlap substantially, so that the PLED can directly excite the mode. An additional spacer layer between PLED and waveguide is shown to improve the coupling efficiency by about a factor of 5. For iridium-based diodes, PLED-to-waveguide coupling efficiencies as high as 3.2% have been obtained.

The second configuration, using a PL material, offers several advantages such as facilitating the production process or improving the coupled light intensity. The coupling mechanism relies on direct excitation of the waveguide mode by the evanescent field of the co-planar PL material. In summary, both configurations are based on evanescent field coupling, but in the first and second configuration, the evanescent field is generated by electrical and optical excitation, respectively.

At the out-coupling grating stage, a fully organic mini-spectrometer compatible with monolithic integration on optical biochips has been developed. It consists of a single-mode waveguide with integrated diffraction grating and a dense array of PPDs as sensing element. An organic mini-spectrometer represents an important building block for disposable low-cost bio- and chemical sensors. A spectral resolution of down to 5 nm could be achieved with an integrated optoelectronic system.

Finally, absorption-based bio-tests with fully organic optical devices were demonstrated. The different building blocks were integrated in a resonant system – based on surface plasmon resonance – which opens the route toward sensitive, cost-effective and disposable lab-on-a-chip biosensors.

Keywords: organic electronic, integration, single-mode waveguide, evanescent coupling, low cost biosensor, spectrometer.

Résumé

L'intégration de composants optoélectroniques organiques – tels que les diodes électroluminescentes (DEL) organique et les photodiodes (PD) organiques – sur des bio-puces est étudiée. La bio-puce se décompose en un substrat de verre, un guide d'onde monomode et un réseau de diffraction optique pour coupler hors du guide la lumière. La nature soluble des composants de l'électronique organique permet une déposition des DEL et des PD organique par des procédés additifs tels que l'impression par jet d'encre. Ce procédé est compatible avec l'impression en grande production du type presse typographique; ce qui peut contribuer à la fabrication de capteurs biologiques miniatures peu chers.

Le couplage évanescent est utilisé pour injecter la lumière d'un émetteur organique Lambertien dans un guide d'onde monomode. Soit une DEL organique est déposée directement sur le guide d'onde; ou une DEL organique – située de l'autre côté du substrat – pompe une couche photoluminescente située directement sur le guide d'onde.

Dans la première configuration, grâce de la proximité du guide d'onde, la zone d'émission de la DEL organique se superpose avec le mode du guide d'onde. Ainsi, la diode organique peut directement exciter le mode. L'ajout d'une couche d'espacement entre la diode organique et le guide d'onde a engendré une amélioration de l'efficacité de couplage par un facteur 5. Pour une DEL à base d'iridium, une efficacité de couplage – de la DEL organique dans le guide d'onde – de l'ordre de 3.2% a été obtenue.

La seconde configuration, utilisant un matériau photoluminescent, présente plusieurs avantages tel que la plus grande simplicité de production ou l'augmentation de l'intensité de la lumière couplée dans le guide d'onde. Le mécanisme de couplage repose sur l'excitation direct du mode du guide d'onde par un champ évanescent généré par la couche photoluminescente. En résumé, les deux configurations sont basées sur le couplage évanescent, mais ce champ évanescent est généré par une excitation électrique ou optique selon la première ou la seconde configuration envisagée.

Au niveau du réseau de sortie, un mini spectromètre organique compatible avec une intégration monolithique sur des capteurs biologiques a été développé. Ceci consiste en un guide d'onde monomode équipé d'un réseau de diffraction intégré et d'une juxtaposition à forte densité de PD organique en tant que détecteur optique. Ce mini spectromètre organique représente une partie importante pouvant être utilisé pour les capteurs biologiques et / ou chimiques jetables et peu chers. Une résolution spectrale de 5 nm a été atteinte avec ce système optoélectronique intégré.

Finalement, un test d'absorption biologique – utilisant cette plateforme à base de composants optiques organiques – a été réalisé avec succès. Une version de ce système de mesure a été intégré avec un système résonant – basé sur les plasmons de surface – permettant d'ouvrir la route vers des capteurs et / ou puces biologique très sensibles et peu chers.

Mot clés: électronique organique, intégration, guide optique monomode, couplage évanescent, capteur biologique à faible coût, spectromètre.

Glossary

Symbols

$\Re$	responsivity
D^*	specific detectivity
Λ	grating period
$\frac{dP}{d\Omega}$	power per unit solid angle
n_{eff}	effective refractive index
μ_*	mobility prefactor
A	dipole emission
B	bandwidth
C	power coupled into waveguide per unit length
d	thickness organic layer
d_p	penetration depth
$d\lambda/dz$	linear dispersion
E	electric field
e^-	electron
E_{ex}	exciton energy
E_{gap}	gap energy
F_{OLED}	OLED power per unit area
h	horizontal dipole
h	Planck's constant
h^+	hole
I	current
i_D	dark leakage current
I_N	noise current
I_s	shot noise dark current
J	current density
J_{FN}	Fowler-Nordheim current
J_{SCLC}	space charge limited current
J_{th}	thermionic current
k	Boltzmann's constant
k	wavevector
k_{SP}	surface plasmon wavevector
L	thickness of the active layer
L_A	absorption length
L_D	exciton diffusion length
L_{loss}	waveguide loss length
L_{OLED}	OLED length
L_v	luminance
m^*	effective mass
m_o	mass of the free electron
η	coupling efficiency
n_{pix}	number of effective pixels
p	transverse magnetic polarization
$P_{Grating}$	optical power at the grating stage
P_{inc}	incident power
P_{ph}	intensity of the incident light
P_{PLED}	optical power at the PLED stage
Q	cavity quality factor
q	elementary charge
r	amplitude reflection coefficient
r_{st}	fraction of excitons formed as singlet
s	transverse electric polarization
S_0	fundamental state
S_1	excited state
S_{CO}	chemo-optical sensitivity
T	temperature
t	amplitude transmission coefficient
T_1	transition state
V	applied voltage
v	vertical dipole
$V(\lambda)$	photopic vision function
w	width of the organic photodiode pixel
W_{OLED}	OLED width
α	absorption coefficient
α_L	waveguide loss
β	electric-field coefficient to the mobility
γ	ratio of exciton formation events
Δ	triangular barrier between LUMO and Fermi level of the contact
ΔJ	photocurrent density
$\Delta\Gamma$	mass adsorption to the surface
$\delta\Gamma_{adv}$	device sensitivity
$\Delta\lambda$	spectral resolution
$\delta\lambda_{adv}$	dip position determination accuracy
ε	permittivity
η_A	photon absorption
η_{CC}	collection of the free charge carriers
η_{CT}	exciton dissociation
η_{ED}	diffusion of the exciton to the DA interface
η_{EQE}	external quantum efficiency
η_{int}	internal quantum efficiency
η_{IQE}	internal quantum efficiency
η_p	power conversion efficiency
θ	out-coupling angle
θ_j	angle between the wavevector and the reference axis
κ	coupling efficiency of the grating
λ	wavelength

μ	mobility
ξ	fraction of the guided light without waveguide losses
π	double carbon-carbon bonds
ρ	efficiency of radiative decay
σ	single carbon-carbon bonds
σ	standard deviation
τ	transit time
τ_{CT}	charge-transfer time
φ_{e-}	electron flux
$\varphi_{luminance}$	Luminance efficiency
$\varphi_{luminous}$	Luminous efficiency
φ_{photon}	photon flux
n	refractive index
Π	power flux

Abbreviations

α-mIgG	anti-mouse IgG with fluorescent marker
AWACSS	automated water analyser computer supported system
C_{60}	buckminsterfullerene
CFU	colony forming unit
CMOS	complementary metal oxide semiconductor
CSEM	Centre Suisse d'Electonique et de Microtechnique
CT	charge-transfer
CuPc	copper phthalocyanine
Cy5	fluorophore marker
DA	donor-acceptor
DIC	differential interference contrast
DNA	deoxyribonucleic acid
EA	electron affinity
ED	exciton diffusion
EL	electroluminescence
EQE	external quantum efficiency
ETL	electron-transport layer
F8BT	poly(9,9-di-n-octylfluorene-alt-benzothiadiazole)
FWHM	full-width-at-half-maximum
HCl	hydrochloric acid
HOMO	highest occupied molecular orbital
HTL	hole-transport layer
IgG	anti-mouse immunoglobulin G
IP	ionization potential
IR	infrared
$Ir(mppy)_3$	iridium (III) tris(2-(4-totyl)pyridinato-N,C2)
ISC	intersystem crossing
ITO	indium tin oxide
LOC	lab-on-a-chip
LOD	limit of detection
lOW	integrated optical waveguide
LUMO	lowest unoccupied molecular orbital
MDMO-PPV	poly[2-methoxy-5-(3,7-dimethyloctyloxy)-1,4-phenylenevinylene]
MEH-PPV	poly[2-methoxy-5-(2-ethyl-hexyloxy)-1,4-phenylene-vinylene]
mIgG	mouse immunoglobulin G
NA	numerical aperture
NEP	noise equivalent power
OFET	organic field effect transistor
OLED	organic light emitting diode
OPD	organic photodiode
OPV	organic photovoltaic
P3HT	poly(3-hexylthiophene)
PBD	2-(4-Biphenylyl)-5-(4-tert-butylphenyl)-1,3,4-oxadiazole
PCBM	[6,6]-phenyl-C_{61}-butyric acid methyl ester
PCE	power conversion efficiency
PECVD	plasma-enhanced chemical vapor deposition
PEDOT:PSS	poly(3,4-ethylenedioxy thiophene) poly(styrene sulfonate)
PL	photoluminescent
PLED	polymer light emitting diode
PMMA	poly(methyl methacrylate)
POC	point-of-care
POCT	point-of-care testing
PPD	polymer photodiode
PVK	poly(9-vinylcarbazole)
RI	refractive index
RIANA	river analyser
RifS	reflectometric interference spectroscopy
RIU	refractive index units

RNA	ribonucleic acid
SAR	scanning angle reflectometry
SCLC	space charge limited current
SEMOFS	Surface Enhanced Micro Optical Fluidic Systems
SiO_2	silicon dioxide
SMOLED	small molecules organic emitting diode
SP	surface plasmon
SPR	surface plasmon resonance
Ta_2O_5	tantalum pentoxide
TE	transverse electric polarization
TIRF	total internal reflection fluorescence
TM	transverse magnetic polarization
TPD	N,N'-Bis(3-methylphenyl)-N,N'-diphenylbenzidine
UV	ultraviolet

I. Introduction

1. Goal

The primary application of photonic integrated circuits lies in the area of fiber-optic communication. Nevertheless, applications in other fields, such as biomedical sensing for which price per device is often a critical issue, are gaining in importance too. By far the most commonly used light sources in all of today's applications are inorganic lasers or light emitting diodes. CSEM has developed an alternative, monolithically integrated solution based on polymer light emitting diodes (PLEDs). At the detection stage, instead of a non-integrated silicon photodiode, photomultiplier or complementary metal oxide semiconductor (CMOS) sensor; an array of integrated polymer photodiodes (PPDs) is used. This integrated approach keeps the promise of reducing the overall circuit costs to a point where currently cost-sensitive markets – such as point-of-care (POC) diagnostics, for example – might become accessible.
The past few years have seen great advances in lab-on-a-chip (LOC) technologies for genomic, proteomic, and enzymatic analysis [1]. The need for low-cost and disposable medical devices has driven the development of these LOC systems for point-of-care testing (POCT).
POCT is defined as diagnostic testing at or near the site of patient care [2]. The driving notion behind POCT is to bring the test conveniently and immediately to the patient. This increases the likelihood that the patient will receive the results in a timely manner. POCT is accomplished through the use of transportable, portable, and handheld instruments (e.g., blood glucose meter, nerve conduction study device) and test kits (e.g., HIV salivary assay). Cheaper, smaller, faster, and smarter devices have increased the use of POCT approaches by making it cost-effective for many diseases.
Major benefits are obtained when the output of a POCT device is made available immediately within an electronic medical record. Results can be shared instantaneously with all members of the medical team through the software interface enhancing communication by decreasing turnaround time. A reduction in morbidity and mortality has been associated with goal-directed therapy techniques when used in conjunction with POCT and the electronic medical record.
Disposable biosensors are required because of the irreversible sensor response after the analyte adsorption and the possible contamination after each examination.
These systems should be inexpensive, but still accurate, reliable and portable. By integrating different functional units for separation, reaction and detection, with a single microfluidic channel network, it could become feasible to realize one microchip comprising all features of a complete lab and could be used to perform complex reactions and analyses.

Organic optoelectronic devices – due to their potential ease of use especially in regard to production processes – make them highly attractive for integrated, cost-effective and niche LOC applications. A major strength of organic optoelectronics, particularly polymer optoelectronics based on solution processing, is the possibility to deposit such semi-conducting inks by additive print processes in defined patterns and areas forming the desired integrated systems.
Organic semiconductors offer other important benefits beside low fabrication cost. In polymers, the semiconducting properties arise from overlap in electron orbits along carbon chains where single and double bonds alternate. In these conjugated systems both emission and absorption bands are inherently wide, and wavelength ranges can be tuned by selecting the proper compounds making up the polymer.
Although many researchers are publishing results for discrete organic light emitting diodes (OLEDs), organic field effect transistors (OFETs), and organic photodiodes (OPDs), little

work has been done in developing a process-flow for the integration of these components toward monolithic systems. However, one of the major challenges in carrying organic electronics from research labs into the industrial world is developing a simple process flow.

2. Context of this work

This work was supported by the European project SEMOFS [3] (Surface Enhanced Micro Optical Fluidic Systems). The aim of the SEMOFS project was to develop a radically new concept for biosensors: a polymer-based card type integrated ”plasmon enhanced” sensor. It is based on waveguide design.
The integration of sensing functionality as well as assay functionality into a compact device offers the opportunity for a fully integrated cartridge-like device and would allow transferring complexity from the macro system (readout-system) to the micro system, leading to a LOC. The aim is to develop technologies, demonstrators and bioprotocols for the polymer based integrated probe card. It employs label-free optical detection based on surface plasmon resonance (SPR). Both active and passive optical components (light source, waveguide, and detector) as well as fluidic elements for active liquid transport and immobilized biological material (e.g. antibodies) will be integrated in the card. The final product shall be manufactured with large-scale, mass-production techniques. The card will therefore be very inexpensive and disposable while providing increased sensitivity and diagnosis possibilities.
This new type of biosensor concept will go far beyond the existing technology platforms and will provide increased sensitivity and simpler diagnosis possibilities, cost effectiveness and disposability.

3. Definition and state-of-the-art biosensors

The field of organic optoelectronic is becoming active in the domain of biosensors. However more mature devices – based on inorganic technology – are already occupying the market and exhibit very desirable properties such as large robustness and high sensitivity. This section will summarize the best technologies in competition with the biosensor developed within this work.

a. Biosensors

Biosensors use a biochemical reaction to measure the concentration of a particular substance and to differentiate it from other substances present in the sample. The measurement device is composed of three components: a biochemical component (enzymes, nucleic acids, antibodies, bacteria, animal or vegetable tissues etc.) of appropriate specificity for the analyte; a transducer to convert the recognition event into a suitable physical signal (electrical, optical etc.), and a detection and recording system, including analysis and processing, which is usually electrical or computer controlled [4].
Biosensors comprise a large variety of concepts and devices. There are electrochemical sensors (amperometric sensors, potentiometric sensors, conductometric sensors), nanomechanical sensors (piezoelectric mass sensors, micro-cantilever sensors) and optical sensors (label-based or label-free optical biosensors). Optical biosensors are powerful detection and analysis tools that have vast applications in biomedical research, healthcare, pharmaceuticals, environmental monitoring and combating biological threats [5]. The main advantage of optical biosensors over electrochemical biosensors is that they are resistant to electromagnetic interference, capable of performing remote sensing, and they can provide multiplexed detection within a single device. Generally, there are two broad detection

protocols that can be implemented in optical biosensing: labeled (e.g., fluorescence-based detection) and label-free detection (SPR and bragg resonant grating).
This work aims at developing an optical biosensor platform based on evanescent wave interaction with labeled and label-free detection processes.

b. Biosensors for health diagnosis – the biological interactions

Recent research carried out in biology has led to the identification of thousands of genes involved in the development of pathological events. Thanks to the identification of the genes' functions, it is possible to use them in disease diagnosis protocols. The diagnosis is carried out by studying the biochemical reaction between a biological probe and a biological target, using a specific sensing technology.
To study the proteome, a technology similar to deoxyribonucleic acid (DNA) microarrays is being developed for identification and quantification of proteins from crude lysates. Although protein chips are developed mainly to study protein-protein interactions, the most promising approach for protein profiling is to use antibody microarrays. Antibody-based techniques which are also compatible with chip-based analyses, are likely to prove to be the most powerful approach to screening protein functions and relationships on a large scale. Similarly to the efforts made in genomics and structural genomics, the analysis of complete proteomes through the production of antibodies to manufacture high density microarrays is being undertaken by many groups [6]. Several approaches to produce antibodies or derived capturing molecules, based on production of libraries are being developed by a number of research groups.
Whereas DNA chips were first developed to study, in research labs, whole transcriptomes, before being used as a diagnostic tool, it seems that the opposite is happening for protein chips: "Protein chips could take an opposite course from that of DNA chips and be useful in the clinic laboratory before they make a big impact in the research lab" [7].
The possibility to perform a large number of miniaturize diagnostic tests in parallel will end up, in a near future, with a better medical follow-up and also with reduction of the cost per diagnostic test. "Miniaturized and highly parallelized immunoassays will reduce costs by decreasing reagent consumption and improve efficiency by greatly increasing the number of assays that can be performed with a single serum sample. The system will significantly facilitate and accelerate the diagnostics of autoimmune diseases and can be adapted easily to any other kind of immunoassay" [7].

c. Optical biosensing technologies – expensive, non disposable, limited number of channels

Label-free and labeled optical methods [8] take advantage of the penetration depth of the evanescent wave into the sample under study to look at molecule binding at interfaces. The evanescent wave can be generated using the total internal reflection of a beam, a waveguide mode or a surface plasmon (SP) at a metallic interface.
Today, most label-free optical detection systems found on the market are based on surface plasmon resonance [9]. Biochemical interactions at the sensor surface are monitored by observing the resonant behavior of surface waves on a thin metal film. Companies currently selling instruments based on this effect include the market leader Biacore (Uppsala, Sweden [10]), HTS Biosystems (East Hartford, CT, USA) and Texas instruments (Dallas, TX, USA). Instruments based on other optical principles such as dielectric planar waveguides are still under development, for example by SRU Biosystems (Woburn, MA, USA) and Farfield Sensors (Manchester, UK). Other optical technologies found in publications or in development at University labs include resonant mirrors [11], reflectometric interference spectroscopy (RifS [12]) and scanning angle reflectometry (SAR [13]).

The most severe limitations of all of these approaches are the high price of the system (instrument and chips) and the large size of the equipment for chip-reading since the chip is interrogated optically (an optical beam propagates from the reader to the chip). In addition, the fluidic part is not integrated [14] (external pump, tubes and connections are needed). The difficulty for miniaturization is a serious drawback, especially for POC applications, for example in medicine.
In the following Table I-1, more detailed information about the different existing technologies are given.

	System/Technical characteristic	Advantage	Limitations
SPR commercially available	**Biacore SPR technology** Sensitivity: Approx. 6 pg/mm² (down to 0.3 pg/mm2 in certain cases) Cost: About **200€ + reader cost**	Label free SPR Patents pending on surface chemistry	Not integrated (light source outside) maximum 4 channels Very expensive reader Multimaterial (incl. Glass prism)
	Biacore: Flexchip (formerly HTS Biosystems) replicated grating-coupled SPR sensor chips	Label-free SPR Replicated chip	Not integrated Expensive reader
	Sensata Technologies (formerly Texas Instruments) Spreeta SPR sensor (also available from Nomadics) Classical LED + polariser Plastic prism Glass chip Dimensions: 1.5 cm x 0.7 cm x 3 cm Sensitivity: Approx. 10 pg/mm² Cost: About **100€ + reader cost**	Label free SPR Integrated	Expensive Not disposable Size reduction not possible Only 3 channels Only pipetting, no fluidics Multimaterial
	IBIS I-SPR Sensitivity: Approx. 10 pg/mm²	Imaging SPR	Not integrated
	Reichert Sensitivity down to 150 Da	Label-free SPR Wide operating temperature range: 10℃ below ambient to 90℃ Broad refractive index range (1.32 to 1.52)	Not integrated
	Biosensing Instrument (< 100 Daltons)	Label-free SPR	
	Proterion (acquired by Wyatt technology corporation)	SPR + Waveguide Patented technology Approx 1 pg/mm²	Not listed in the product list
Other optics	**SRU Biosystems:** BIND reader and biosensor Analysis of reflected light on dielectric waveguide grating	Simple chip: one grating on dielectric waveguide MTP 96 or MTP 384	Equipment cost (spectrometer) Sensitivity 0.3 ug/ml to 1 mg/ml (a few 10 pg/mm²) Not integrated
	Farfield scientific: AnaLight Bio Dual evanescent wave laser interferometry	Sensitivity < 1 pg/mm² molecular orientation monitoring possible	Equipment size & cost Not integrated
	Farfield group: neosensor (IAsys)	Resonant mirrors	Equipment cost, data processing (complexity of the signals) Not integrated
	Corning, EPIC System	Waveguide grating Label-free MTP 384	High equipment cost (spectrometer) Sensitivity 5 pg/mm^2 Not integrated
	Microvacuum: OWLS 110	Waveguide grating Label-free Polarisation TE & TM	4 channels Not integrated
	Dynetix: (CSEM)	Waveguide grating Label-free	Not integrated 8 channels Device sensitivity $\Delta\Gamma pp$ = 130 fg/mm^2
	ForteBio: Octet Biosensor Reflectometric interference spectroscopy (RifS [12])	MTP 96	Not integrated

SPR	**University of Southampton** [15] University of Florida Waveguide + gold layer	High sensitivity of 10^{-6} in refractive index change 1.2 ng/mL (hCG)	No source and detector integration
Publications	Automated Water Analyser Computer Supported System (AWACSS) and River Analyser (RIANA) ➔ European project	immunoassay 0.2 pg/mL fully automated	Label needed Not integrated
	Scanning angle reflectometry (SAR [13])	Direct study at the interface layer-substrate	Equipment cost, data processing (complexity of the signals)
Fluorescence	**Three fold sensor** Sub-picogram/mL in blood or urine	Real-time fiber optic sensing 6min	Label needed Not integrated
	Research international: Raptor 4 channels	Toxins <1.0 ng/ml bacteria100 Colony Forming Unit (CFU)/ml	Label needed Not integrated
	Research international: BioHawk 8 channels	1 to 10 ppb for toxins 100 to 100,000 CFU/ml for bacteria 10 min	Label needed Not integrated
	Zeptosens [16] Waveguide excitation of fluorescence, free space collection of fluorescent light	Ultrahigh sensitivity 20'000 points per hour	Label needed Not integrated

Table I-1: Comparison of commercially available or published optical biosensor technologies.

In contrary to the solutions detailed above, the biosensor platform referred to in this thesis is a completely integrated biochip (optics, microfluidics, sensing layer and detection). Only an electrical interface is additionally needed. Note that typical prices for one of the readers mentioned above are in the range of 80 k€ to 500 k€, which renders the use of such equipments for POCT unlikely.

d. Market analysis and derivation of industrial requirements

Overall in-vitro diagnostics market, DNA microarray market and protein microarray market have been studied. The market share for clinical trials and diagnostics, for which the biosensor is designed, is expected to grow very fast and reach about 200 mio USD in 2010. A market share of 2%, corresponding to a market volume of 4 mio USD, could be realistic for this biosensor at the present time. However, the successful market entrance is mainly depending on the product performance, the price and the versatility of the analyte panel. The following main requirements for the fully developed sensor ready to enter the market have been derived:

- Low sample volume (few microliters), ideally capillary blood
- Parallel detection of at least 10 relevant markers
- Short time to result (about 10 min)
- Minimized sample conditioning
- Detection limit ≈ 1 pg/ml

- Dynamic range of 4 orders of magnitude for marker concentration
- Competitive price: readout device about 1000€, disposable cartridge about 5€ per information

For POC diagnostics, fast and competitive diagnostic results are desired at an affordable price. The development of lab-on-chip devices for bio-analytical applications has increased tremendously during the past decade. As seen in Table I-1, most of these devices are fabricated using silicon or glass because processes for these materials are well known and their surface properties easily match the requirements of biotechnology. Processing costs as well as cost of the final sensing devices currently limit the extent of functionality that can be integrated on a disposable element. Thus, most of the functionality is currently transferred to the "reader" – the controlling unit – instead of being integrated into the chip. Use of advanced polymer materials, however, equally used as substrates as well as part of active components such as sensors and actuators, might allow to economically produce highly integrated measuring devices for single use.
The integration of sensing functionality as well as assay functionality into a compact device offers the opportunity for a fully-integrated cartridge-like device and would allow transferring complexity from the macro system (readout-system) to the micro system, leading to a "lab-on-a-chip" instead of a "chip-in-a-lab". Both active and passive optical components (light source, waveguide, and detector) as well as fluidic elements for active liquid transport and immobilized biological material (e.g. antibodies) will be integrated in the cartridge. Figure I.1 illustrates the different subsystems and interfaces between the components of a fully integrated micro-optical fluidic system. This new biosensor concept aims at providing increased sensitivity and simpler diagnosis possibilities, cost-effectiveness and disposability. Thus, the objectives reach far beyond the existing technology platforms and integration levels, hereby targeting the sensitivity at the leading edge of the state of the art (≈ 1 pg/mm²) and a parallel analysis with up to 10 channels / markers.

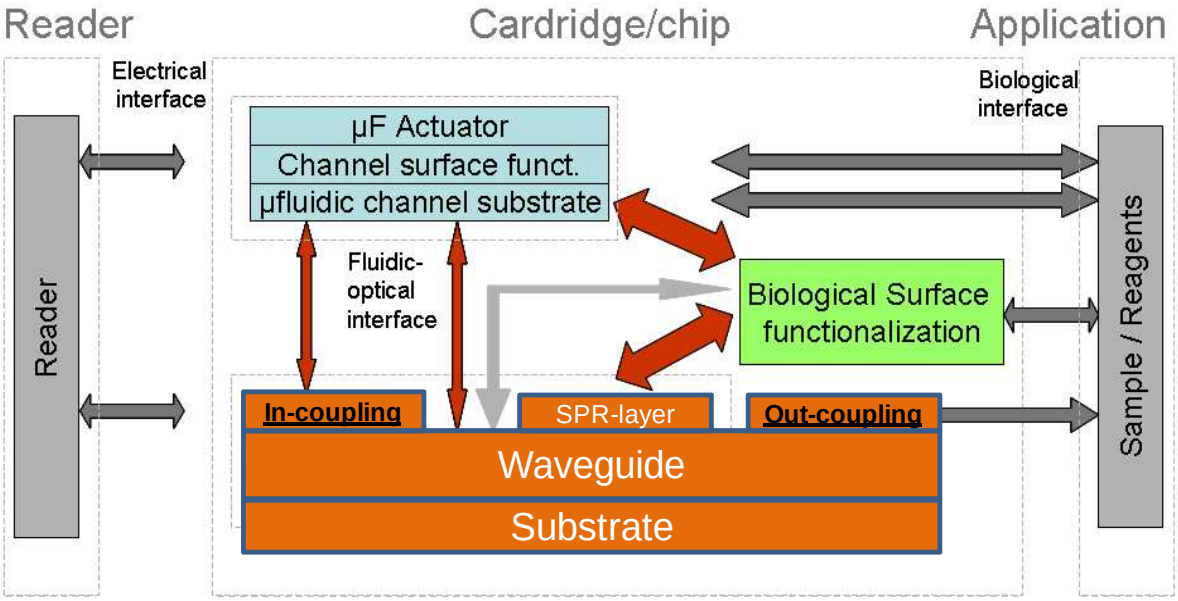

Figure I.1: Interfaces between the components of a fully integrated biosensor.

From Figure I.1, it can be seen that the cartridge consists of a microfluidics part and a micro-optics part, which are fabricated separately and are combined in a final process step. The fluidic used in this thesis work is much simpler compared to the design adopted within the SEMOFS project. The integration of optical components is split in two processing steps: the first step contains the waveguide, the SPR layer system and grating structures for out-coupling the light to external detectors; whereas tests of active optical components (PLED,

detector PPD) are initially carried out on separate substrates (hybrid integration). In a final step, the active components can be monolithically integrated onto the waveguide substrate.

4. State-of-the-art of optical system integration using organic photonics

This section presents an overview how far the system integration of organic photonics has advanced by inspecting some of the most interesting devices schemes used in biosensors and chemical sensors applications.
Only since recently, the integration of organic optoelectronic components into monolithic systems has been explored with examples such as the combination of OFETs with OLEDs [17-19], OFETs and OPDs [20,21], and OLEDs together with OPDs [22-24]. Integration of OLEDs and OPDs is very promising for novel application areas such as chemical sensing [25-27], bio-sensing [28], or integrated photonic systems [22].
Regarding the integration of organic photonics for lab-on-a-chip, two schemes are possible: (I) sandwich design and (II) waveguide design. The first scheme (Figure I.2) defines functional layers such as excitation, microfluidics and optical filtering layer and stacks them on top of each other. It has certain advantages such as wafer scale processing and parallelization in the detection. The second approach, which is the one pursued in this work, builds everything around a waveguide structure. It offers potentially better signal-to-noise ratio than the previous approach and is more flexible.
A simple, yet powerful scheme of type I (Figure I.2) for fluorescence-based assays has been proposed by Pais *et al.* [29,30]. It is based on a high-sensitivity, cost-effective, cross-polarization scheme to filter out excitation light from a fluorescent dye emission spectrum. The cross-polarizers they use, suppress the polarized excitation signal by 22 dB with respect to the randomly polarized fluorescent signal.

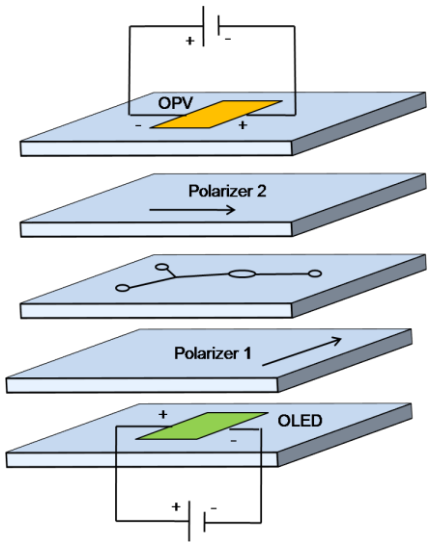

Figure I.2: Schematics of integrated excitation / detection system (figure adapted from Banerjee et al. [30]).

A similar but not exactly identical to scheme I approach is the back detection geometry chosen by Shinar *et al.* for sensing oxygen and biological agents [27,31]. OLEDs and OPDs are arranged in an interdigitated way in the same plane which is separated by an optical filter from the sensing layer. They measure multi-analyte concentration using the robust fluorescence decay technique with pulsed OLEDs.

On the other hand, Hofman *et al.* [26] have used CuPc-C_{60}-based thin-film small-molecule OPDs to successfully monitor chemoluminescence reactions. Their OPDs had an external quantum efficiency of ~ 30% in the 600 - 700 nm wavelength range and an active area of 2 x 8 mm^2.
Shin *et al.* [32] have demonstrated an integrated fluorescence-detection hybrid device with a silicon-based photodiode and an OLED, reaching a limit of detection of 1 µM.
Another example uses an integrated PPV-based OLED excitation source for microscale fluorescence detection [33]. OLEDs also have been used as excitation source in microscale capillary electrophoresis [34].
A company active in the LOC domain is BIOIDENT [35]. They have developed a PhotonicLab™ platform consisting of the combination of printed optoelectronic components with microfluidic systems. The novel concept allows integrating illumination and detection capabilities onto microfluidic-based devices by printing technologies (see Figure I.3).

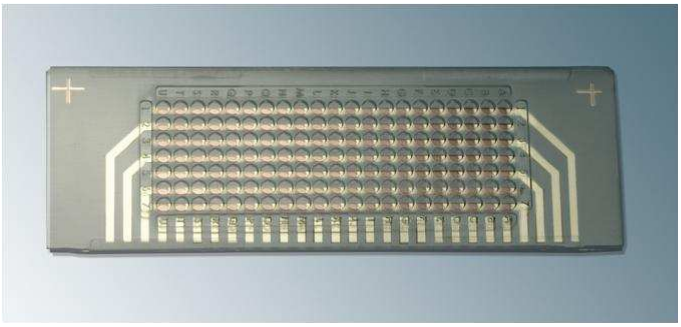

Figure I.3: Disposable nanotiterplate with fully integrated optical readout system [35].

The ultrathin photodiodes with an overall thickness of only 300 to 500 nm show quantum efficiencies better than 50% and linear light-response over 6 orders of magnitude. The pixel size can range from 50 to over 1000 µm and ink-jet fabrication allows tailoring the sensor layout to the needs of the specific application [36]. An equivalent OLED array can be manufactured using the same fabrication procedure but different organic materials. As a consequence, any combination of light emitting and light detecting diodes can be printed on a variety of substrates for sample illumination and signal detection.

5. Working principle of our biosensor

Figure I.4 illustrates the integration of active and passive organic components onto the opto-chip forming a hybrid photonic system which aims at the development of a fully integrated disposable biosensor. Polymer light emitting diodes and polymer photodiodes are integrated along a high refractive index single-mode waveguide. This LOC system has to be compatible with large-scale mass-production techniques in order to become a low-cost product. Light is coupled evanescently into a single-mode waveguide. Guided light interacts with the analyte located in the fluid sample and is finally coupled out by a grating. The detection scheme is based either on surface plasmon resonance or on absorption of the guided light by labeled bio-molecules, which will alter the guided light intensity as a function of wavelength. A grating diffracts the guided light to specific out-coupling angles according to its wavelength components. The integration of the PPD array onto the chip allows to track – in an easy and inexpensive way – the spectral changes due to the interaction with the analyte.
The SPR principle uses biochemical interactions at the sensor surface, which are monitored by observing the resonant behavior of surface waves at a thin metal film (usually Au). This resonant mode will couple with the waveguide mode for a particular wavelength for which the phase-matching condition between the waveguide and the surface mode is fulfilled, and an absorption peak will be observed at this wavelength in the transmitted light spectrum. When molecules are bound on the sensitive surface on top of the metal layer, the refractive index is

slightly changed. This leads to a shift of the absorption peak with respect to wavelength. The integrated micro-optical subsystem is based on a glass slide ("Zeptochip" from Zeptosens [16]). Furthermore, the chip – named opto-chip or biochip – includes a linear grating, which can be used for out-coupling of the light.
Grating couplers built into waveguides are very effective for interacting with guided light, either for in / out-coupling or for intra-waveguide reflection. Grating fabrication is a planar process that can be realized with microelectronic fabrication or replication technologies. Waveguide gratings have interesting properties for intra-waveguide optical processing: when guided light is incident at an angle onto the grating there will be only one wavelength under which light will be reflected (the Bragg wavelength).

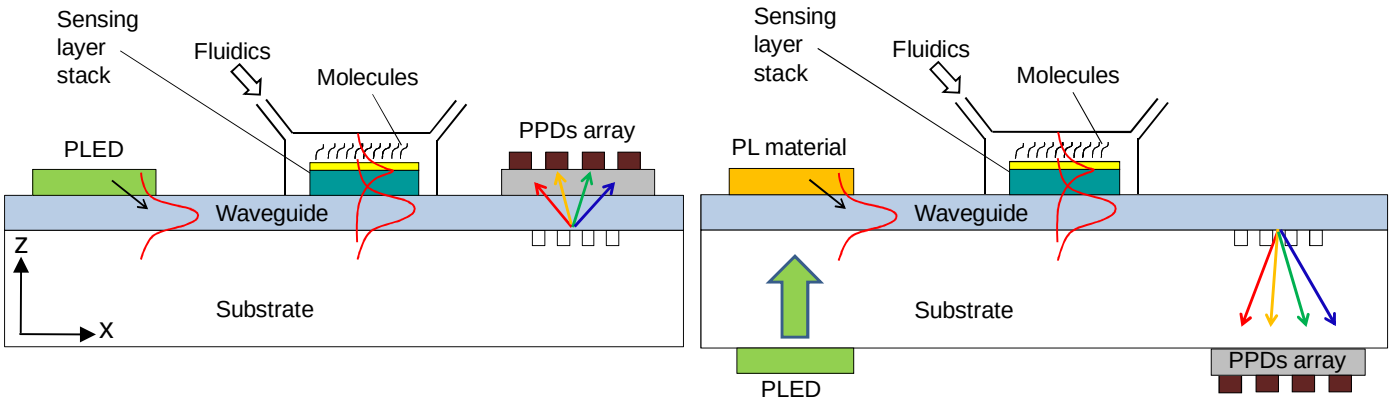

a) b)

Figure I.4: Working principle of the biochip developed within the SEMOFS project. Light is coupled into a single-mode waveguide (a) directly with an PLED or (b) indirectly by the intermediate of photoluminescent material, where it interacts with the analyte located inside the fluidic channel. Changes in the spectrum of the guided light are detected by an array of PPDs.

This thesis focusses on the in-coupling and out-coupling of light from polymer material into a high-index-contrast, single-mode waveguide. A biosensing test based on labelled molecules is presented. A SPR test is also demonstrated in the context of integration of the organic optoelectronic components.

II. Theory and sensing principle

This part describes the optoelectronics properties of organic devices such as OLED and OPD. Then, working principle description of optical biosensors is shown. Finally, the theory for the coupling of an OLED into a single-mode waveguide is described.

1. Organic light emitting diode and conduction in organic material

The word “organic” has several meanings. Its original meaning is "part of or derived from living matter". In chemistry, organic compounds are those compounds that contain carbon.
Electrically conductive properties of polymeric organic materials were studied in the late 1970s by Alan J. Heeger, Alan G. MacDiarmid and Hideki Shirakawa, who were jointly awarded the Nobel Prize in Chemistry in 2000.
Conjugated polymers have a backbone of alternating single and double carbon-carbon bonds. Single bonds are referred to as σ-bonds, and double bonds contain a σ-bond and a π-bond. Although the chemical structure of these materials is generally represented by alternating single and double bonds, in reality, the electrons that constitute the π-bonds are delocalized over many monomers. The π-bonds are at the origin of the semiconducting properties of organic semiconductors. The quantum mechanical overlap of p_z-orbitals actually produces two orbitals, a bonding (π) orbital and an anti-bonding (π*) orbital. The lower energy π-orbitals produce the valence band called “highest occupied molecular orbital” (HOMO), and the higher energy π*-orbitals form the conduction band called “lowest unoccupied molecular orbital” (LUMO). The difference in energy between the two levels produces the “band” gap that determines the electro-optical properties of the material.
Organic electronic devices are often divided into two broad categories according to the nature of their constituting materials. There are the organic materials based on small molecules and based on polymer materials, with preferential deposition techniques such as vacuum evaporation and solution processing approaches (spin coating, ink-jet, gravure printing…), respectively. In the following, the expressions PLED and PPD stand for polymer-based optoelectronic devices. Otherwise, the more general terms OLED and OPD are used. Basically, for the more general theoretical part, the terms “OLED” and “OPD” will be used in the text. For part III and IV, “PLED” and “PPD” will be mainly used since the experimental tests are based on polymer materials.

Organic electroluminescence (EL) is the electrically driven emission of light from organic materials, which was first observed in the 1960s [37,38]. In 1987, a team in Kodak introduced a double layer organic light-emitting device, which combined modern thin film deposition techniques with suitable materials and structure to give moderately low bias voltages and attractive efficiency [39,40]. In the following years, more and more research groups changed their direction toward organic materials. In recent years the speed of innovation increased dramatically. Both research results and commercial products have demonstrated that organic materials offer a very big potential for the future.
In 1990, the Cambridge group of professor Friend announced a conducting polymer-based LED [41,42]. Since then, research activity progress in this new field has been made in the improvements of color gamut, luminance efficiency and device reliability.
An OLED has an organic EL medium consisting of extremely thin layers (< 0.2 μm in combined thickness) sandwiched between two electrodes. In a basic two-layer OLED structure, one organic layer is specifically chosen to transport holes and the other organic layer is specifically chosen to transport electrons. The interface between the two layers provides an efficient site for the recombination of the injected hole-electron pair and resultant electroluminescence.

Indium tin oxide (ITO) deposited on glass substrate is usually chosen as the anode since it has a relatively high work function (~ 4.8 eV), and is therefore suitable for serving as a hole-injecting electrode (Figure II.1 a). In addition, the transparency of ITO allows the light produced within the active layer to exit the device through the substrate (bottom emission). The top electrode (cathode) is usually deposited onto the emissive layer via thermal evaporation of a metal. A low-work-function metal such as Al (~ 4.2 eV), Mg (~ 3.7 eV) or Ca (~ 2.9 eV) is selected as the cathode, which facilitates electron injection. In order to improve device performance, the hole transport layer and electron transport layer are incorporated into the device structure to form a multilayer OLED.

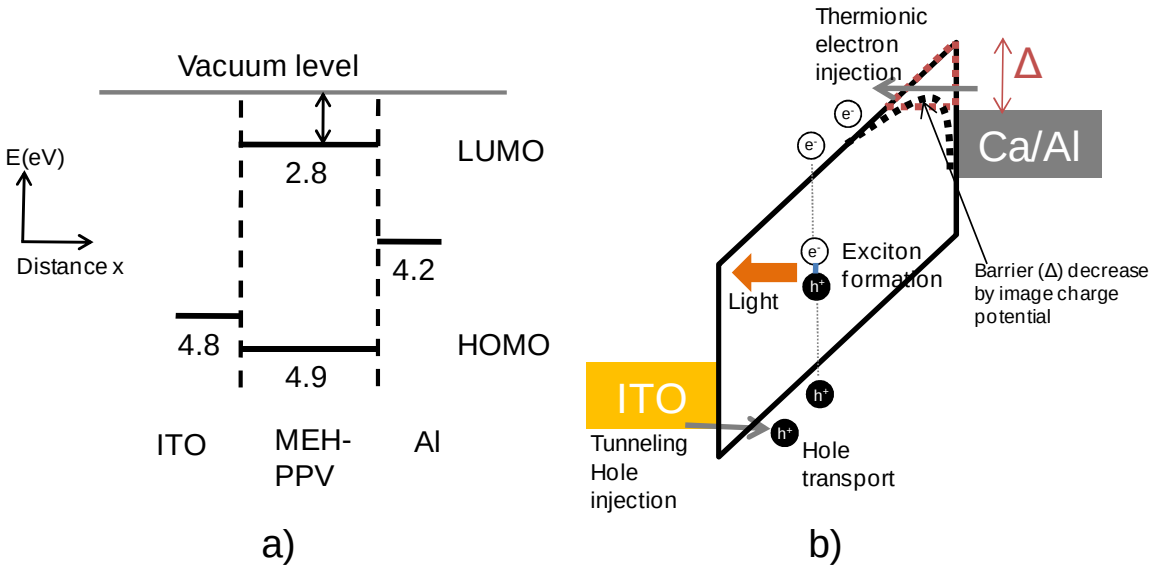

Figure II.1: (a) Energetic position, relative to the vacuum level, of the materials used in the device with a configuration of ITO/MEH-PPV/Al, (b) band diagram for the same device under forward bias with schematic representation of the tunneling (at the anode) and the thermionic (at the cathode) injection process.

a. Current flow inside an (organic) insulator

The organic materials discussed here are, in principle, insulators or at least wide-band-gap semiconductors [43]. Almost all organic semiconductors, whether small molecules or conjugated polymers, are low-conductance materials. Their hole and electron mobilities are typically 10^{-7} cm^2/(V.s) - 10^{1} cm^2/(V.s) and 10^{-8} cm^2/(V.s) - 10^{-2} cm^2/(V.s), respectively [44]. However, it is clear today that the low mobility is due to the disorder in the amorphous or polycrystalline materials. Indeed, in high quality single crystals of pentacene, $\mu_h \sim 1.5$ cm^2/(V.s) were obtained at room temperature [45]. In single crystals of oxygen-doped rubrene, $\mu_h \sim 20$ cm^2/(V.s) were obtained at room temperature [46].
Unlike inorganic semiconductors, the transport and injection properties of OLEDs are determined by intersite hopping of charge carriers (i.e. polarons) between localized states [47]. Amorphous organic materials can transport charge carriers within the molecules along conjugated bonds (alternating single / double bonds) and from molecule to molecule by hopping or tunneling.
The emissive layer consists of a conjugated polymer that has a structural framework of alternating single (σ) and double (π) carbon-carbon bonds. The π-bond is easily broken since the electrons in this bond are loosely bound. Actually, these π electrons are the conduction electrons in conjugated polymers.
The electronic states in most amorphous organic materials are determined by the molecular structure because the influence from neighboring molecules is weak. As a consequence,

localized electronic states with sharp energy levels are formed. Only the LUMO and the HOMO are usually considered for describing electronic charge transport. In amorphous organic materials the electronic states cannot be called “bands" as in crystalline inorganic semiconductors with band formation by periodicity. However, the HOMO and the LUMO can be compared to the valence band and the conduction band in crystalline inorganic semiconductors, respectively.
The actual transition rate of the carriers from one site to another depends on their energy difference and on the distance between them. Since carriers may hop to a site with a higher energy only upon absorbing a phonon of appropriate energy, this decreases the probability of transition to a localized state with higher energy. The energetically allowed hops to a distant site are limited also by the localization length [48]. The energy states involved in the hopping transport of the polarons form narrow bands around the HOMO and LUMO levels. The widths of these bands are determined by the intermolecular interactions and by the level of disorder.

b. Operation of an OLED

In the basic operation mode of an OLED, positive and negative charge carriers are injected from opposite electrodes when the device is sufficiently biased. Injection of holes occurs from the anode into the hole-transport layer (HTL), while electrons are injected from the cathode into the electron-transport layer (ETL). Driven by the applied electric field, holes and electrons move through the polymer over a certain distance until they bind to each other within the polymer layer to form excitons (neutrally bound excited states). Finally, luminous emission into the transparent anode and substrate takes place as a result of radiative decay. Therefore, OLED operation involves charge injection, charge transport, exciton formation and light emission, which is schematically illustrated in Figure II.1 b.
There is typically a triangular barrier Δ for both h^+ and e^- penetration into the EL layer (depicted in Figure II.1 b for the injection of electrons). The value of Δ is defined by the energetic position of the LUMO relative to the Fermi energy of the contact [49].

c. Injection limited current

If the transport capability is faster than the charge injection, the current flow inside the material is determined by the injection process.
When carriers are injected, there is typically an essentially triangular barrier for both hole and electron penetration from electrodes. In the lower-current regime, the current is determined by charge injection that is realized via two possible mechanisms, Schottky thermal injection and Fowler-Nordheim tunneling injection.

i. Large barrier heights: Fowler-Nordheim tunnelling

For large barrier heights the charge carriers can overcome the barrier by tunneling (Figure II.1 b). The tunneling distance and thus the injection probability are strongly dependent on the electric field.
In the Fowler-Nordheim tunneling mechanism, a charge carrier is injected with the assistance of a local high electric field (10^6 - 10^7 V/cm). The current flow is described [49,50] by

$$J_{FN} = \left(\frac{q^3 E^2 m_0}{8\pi\, h\Delta m^*}\right) exp\left(-\frac{4\sqrt{2m^*\Delta^3}}{3hqE}\right)$$

Equation II-1

Where m_o is the mass of the free electron, m^* is the effective mass, E is the electric field, h is Planck's constant, Δ is the barrier between the LUMO and Fermi level of the contact, and q the elementary charge.

ii. Low barrier height: thermionic injection / image charge potential

The height of a triangular barrier as described above is decreased in strong electric fields by the image charge potential [49].
The thermal energy can be sufficient to assist carrier injection from the contacts into materials with low injection barriers. Considering a decrease of the barrier height by image charge effects, the calculation of the current-density resulting from the thermal injection (also called "thermionic injection / emission") gives [50-53]:

$$J_{th} = \left(\frac{4\pi q m^* k}{h^3}\right) T^2 \, exp\left(-\frac{q\Delta}{kT}\right)\left[exp\left(\frac{qV}{kT}\right) - 1\right]$$

Equation II-2

where m^* is the effective mass of the electron (hole), k is Boltzmann's constant, h is Planck's constant, T is the temperature, q is the elementary charge, Δ is the barrier height, and V is the applied voltage [54].

d. Transport limited current

In the case of "ohmic-contacts", injection of charges carriers occurs at any voltage (without appearance of injection barriers), so that charges can be injected without any limits. Currents are limited by the transport processes in the organic layer.
The low mobility in these materials results from the disorder in the amorphous or polycrystalline materials. It is known that charge carrier mobility μ in conjugated polymers is field-dependent, which is described by

$$\mu = \mu_* \, exp\left(\frac{E_a}{kT}\right) exp\,(\beta\sqrt{E})$$

Equation II-3

where E_a is the activation energy, k denotes Boltzmann's constant, μ_* the mobility prefactor, and β the electric-field coefficient to the mobility due to the interaction between charge carriers and randomly distributed permanent dipoles in semiconducting polymers [55]. The coefficient β can be written according to the empirical relation:

$$\beta = \left(\frac{1}{kT} - \frac{1}{kT_0}\right) B$$

Equation II-4

where B and T_0 are constants [55].

e. Space-charge limited current

With an applied electric field of more than 10^5 V/cm and an injected current density larger than the polymer intrinsic charge density, the injected charge carriers accumulate near the polymer-electrode interface to form space charges by virtue of low carrier mobility. As a result, the internal electric field increases, and the current density *J* is determined by the space charge limited current (SCLC). For a single-carrier OLED device, the trap-free SCLC density is given by Child's law:

$$J_{SCLC} = \frac{9}{8}\varepsilon\mu\frac{E^2}{L}$$

Equation II-5

where ε is the permittivity of the polymer, μ is the charge carrier mobility, *E* is the electric field across the device, and *L* is the thickness of the active polymer [56].

f. Efficiency

The internal quantum efficiency η_{int}, defined as the ratio of the number of photons produced within the device to the number of electrons flowing in the external circuit, is given by

$$\eta_{int} = \gamma r_{st}\rho$$

Equation II-6

where γ is the ratio of the number of exciton formation events within the device to the number of electrons flowing in the external circuit, r_{st} is the fraction of excitons which are formed as singlets, and ρ is the efficiency of radiative decay of these singlet excitons.

Electroluminescent efficiencies are important characteristics of OLEDs, often quantified employing the external quantum efficiency (EQE), luminance efficiency, and luminous efficiency.

- External quantum efficiency: it gives the ratio of the number of useful light particles to the number of injected charge particles. EQE is calculated using

$$EQE = \frac{\pi q}{K_m hc}\frac{L_V}{J}\left[\frac{\int I(\lambda)d\lambda}{\int\left(\frac{1}{\lambda}\right)I(\lambda)V(\lambda)d\lambda}\right]$$

Equation II-7

Where L_v is the luminance (cd/m^2) of the device at a current density of *J* (A/m^2). K_m = 673 lm/W is a constant of the luminous efficiency at λ = 555 nm, and *V(λ)* is the photopic vision function which relates perceived (photometric) light levels to physical (radiometric) quantities.

- Luminance efficiency: it is given by

$$\Phi_{luminance} = \frac{L_V}{J}$$

Equation II-8

- Luminous efficiency: it is the luminous flux (Φ_V in lm) of the light source divided by the electrical input power. Luminous efficiency is defined as

$$\Phi_{luminous} = \frac{\Phi_V}{I \cdot V}$$

Equation II-9

Where the product I·V is the electrical input power of the device.

g. State-of-the-art in OLED research

The developments in both small molecules organic emitting diodes (SMOLEDs) and PLEDs since the past few years have been truly spectacular: from very dim devices with a lifetime of less than 1 min in air to red, green and blue OLEDs that can operate continuously, based on accelerated lifetime measurements, for over 200 000 hrs (~ 23 yrs, red and green) and 100 000 hrs (blue), at a brightness of 150 Cd/m^2 (i.e. slightly less than a typical TV or computer monitor) [57-59]. In pulsed operation, OLED brightness values exceeding 10^6 Cd/m^2 have been reported [60]. Indeed, the achieved performance characteristics of OLED devices have surpassed the ones of conventional light sources, so that major efforts are underway to develop OLEDs for general lighting applications. Recently, Kido and coworkers have demonstrated ~ 30 × 30 cm^2 white OLED panels with an efficiency of ~ 20 lm/W at a brightness of ~ 2000 Cd/m^2 [61].
In summary, the highest efficiency OLEDs now exhibit η_{EL} > 20% and η_{Power} > 50 lm/W [62], where 1 lm ≡ 1.46 mW at 555 nm (the wavelength to which the human eye is most sensitive) at a brightness of L_v ~ 150 Cd/m^2, where 1 Cd ≡ 1 lms^{-1}.
The remaining challenges in OLED technology are (i) to achieve higher efficiencies (i.e. η_{Power} > 100 lm/W) and longer lifetimes, well in excess of 10 000 hrs, at brightness levels which may exceed 5000 Cd/m^2, and (ii) to develop reliable, electrically pumped organic diode lasers.

2. Organic photodiode

Over the last few years several new architectures for organic photodetectors and photovoltaic devices have been proposed, which will eventually lead to higher conversion efficiencies. The best EQE, better than 70%, is most easily obtained in bulk heterojunctions. Note that the physics of OPDs is very close to the physics of organic solar cells. So far, most of the research has focused on organic solar cells. Despite this, their performance figures are still far behind competing technologies such as crystalline silicon. Nevertheless, the research activities in organic solar cells have opened the doors to other fields such as OPDs, which are becoming more and more interesting.
The numerous synthesis possibilities to obtain new organic materials with tuned electro-optical properties enhance the creative involvement of polymer chemists in this interdisciplinary field of research and therefore allows for a great diversity of photodetectors, optimized for each application.
However, OPDs show some limitations. As already mentioned, in semiconducting polymers, charge transport is limited by charge carrier hopping between localized states, rather than transport within a band. Charge trapping in defect states involves low mobilities, which range from 10^{-8} cm²/(V.s) to 10^1 cm²/(V.s). Low charge carrier mobilities limit the useful thickness of devices, and, consequently, limit light absorption and thus the photocurrent. Due to large exciton binding energies, the photocurrent is sensitive to temperature. Furthermore, a strong driving force, e.g. an electric field, must be present to break up the photogenerated excitons. Carbon compounds are extremely sensitive to heat, and generally decompose below 300℃.

Finally, many organic materials are susceptible to degradation in the presence of oxygen or water.

a. The photovoltaic effect

Figure II.2 shows the stack of layers of an organic photodiode / solar cell and a simplified diagram of the photovoltaic effect in a polymer heterojunction.

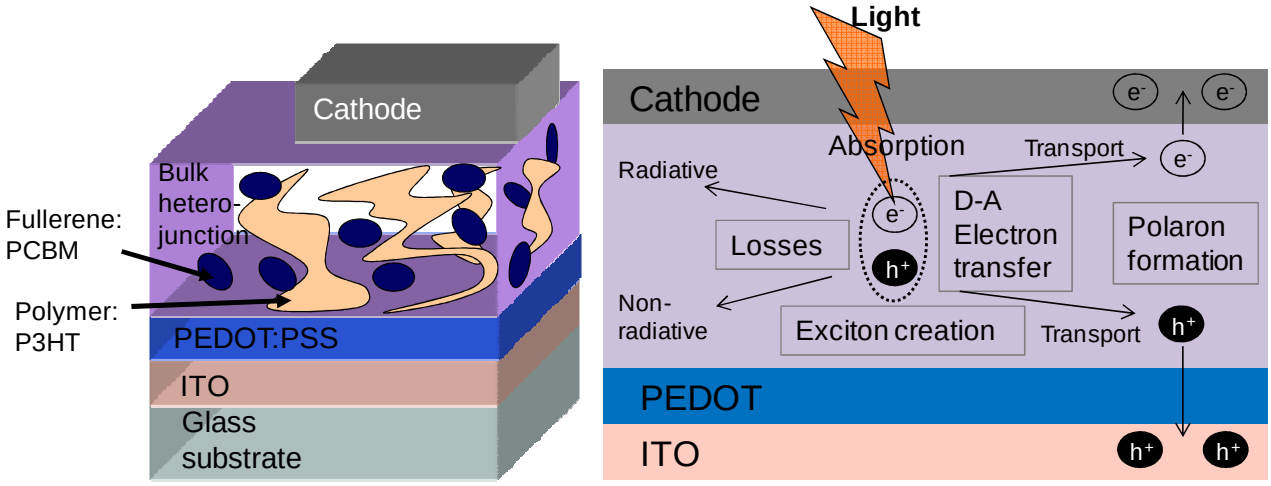

a) b)

Figure II.2: (a) Bulk heterojunction organic photodiode. (b) Simplified diagram showing the photovoltaic effect in a polymer heterojunction photodiode.

The steps involved are: absorption of a photon; exciton creation; exciton diffusion; electron-hole separation; carrier transport to the respective electrodes; carrier extraction at the electrodes. It has been recognized that the most efficient exciton dissociation in organic materials occurs at a donor-acceptor (DA) interface [39]. At such an interface, the donor material with a low ionization potential (IP) forms a heterojunction with an acceptor material with a high electron affinity (EA) as illustrated in Figure II.3. Depending on the alignment of the energy levels of the donor and acceptor materials, the dissociation of the strongly bound excitons, i.e. 0.1 eV to 1 eV, occurs. This is in strong contrast to inorganic semiconductors, where the binding energy is much smaller. For this reason, dissociation can become energetically favorable at such an interface, leading to a free electron polaron in the acceptor material, and a free hole polaron in the donor, as illustrated in Figure II.2 and Equation II-10. The dissociation, or charge-transfer (CT) process, typically occurs over time scales τ_{CT} of a few hundred femtoseconds or less [63]. Since τ_{CT} is much shorter than any other competing process, the charge transfer efficiency approaches 100%.
A simple model for the charge transfer mechanism is the following sequence of events: first, the donors is excited, then the excitation is delocalized on the DA complex before charge transfer is initiated, leading to an ion radical pair. Finally, charge separation can be stabilized, possibly by carrier delocalization on the D^+ (or A^-) species by structural relaxation [64].

$$D^* + A \rightarrow (D - A)^* \rightarrow (D^+ - A^-) \rightarrow D^+ - A^-$$

Equation II-10

The energy level diagram for two DA heterojunctions is shown in Figure II.3. The exciton in the donor material has an energy E_{ex} which is smaller than the HOMO-LUMO gap E_{gap} by the

exciton binding energy. The charge-transfer state, with the electron in the acceptor and the hole in the donor has an energy IP_D-EA_A (the D and A subscripts refer to the donor and acceptor materials, respectively). Since for the left-hand DA junction $E_{ex} > IP_D$-EA_A the charge-transfer reaction will take place [65,66].
However, for the right-hand DA junction $E_{ex} < IP_D$-EA_A, implying that the charge-transfer reaction is energetically unfavorable.

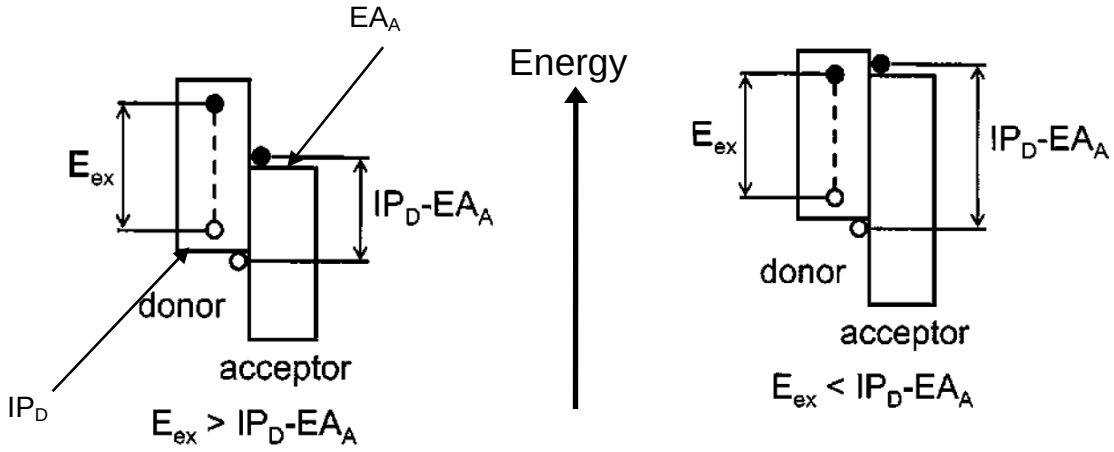

Figure II.3: Schematic illustration of the energy level alignment requirements for efficient charge transfer from the photoinduced state to take place: energetically favorable on the left side, and energetically unfavorable on the right side [67].

b. OPD architecture

As already mentioned, different organic photodetector structures have been explored during the last twenty years. Specific aspects of organic semiconductors have to be taken into account when designing a photodetector architecture. First, the exciton diffusion length (L_D) is low in organic semiconductors, from 10 Å to 100 Å. Second, the exciton binding energy in organic semiconductors is generally large (0.1 - 1 eV) compared to silicon, such that the built-in electric fields (of the order of 10^6 - 10^7 V/m) are usually not large enough to dissociate excitons directly [67]. And third, the charge carrier mobilities are low in organic semiconductors.
The first organic photodetectors were based on a single semiconducor layer with a Schottky barrier at the aluminum contact. In this structure, photogenerated excitons can only be dissociated in the thin depletion layer at the Schottky contact. Thus, the device is exciton diffusion and dissociation limited.
Bilayer devices, with a p-type and a n-type layer stacked together and forming a planar interface followed. Dissociation could be enhanced by an appropriate choice of donor and acceptor layers. However, only those excitons generated within an exciton diffusion length of the interface are dissociated in the thin layer at the heterojunction interface. On one hand, if one increased the layer thickness, the fraction of excitons that recombine without dissociating would become large. On the other hand, if one reduced the thickness to L_D, the absorption would be low. Thus, this structure is exciton diffusion limited.
The latest structure is the bulk heterojunction. The objective of the bulk heterojunction is to intimately mix the donor and acceptor components in a bulk volume so that each donor-acceptor interface is within a distance less than the exciton diffusion length of each absorbing site. Due to the interface being dispersed throughout the bulk, no loss due to the small exciton diffusion lengths is expected.

However, the bulk heterojunction (Figure II.2) requires percolated pathways for hole and electrons from the place of charge separation to the respective electrodes. In other words, the donor and acceptor phases have to form a bi-continuous and interpenetrating network. Therefore, the bulk heterojunction devices are very sensitive to the nanoscale morphology.
We conclude that the bulk heterojunction has proven to be the best concept to overcome the short exciton diffusion length of polymer semiconductors and results in the most efficient OPDs. We stress the fact that in this structure, the nanoscale morphology is of outermost importance to ensure complete exciton dissociation as well as efficient charge carrier pathways to the electrodes.

c. Best literature results

Table II-1 summarizes best results of organic photodetectors and solar cells obtained by various researchers so far.

Active layer structure	J_{sc} (mA/cm²)	η_p (%)	P_{inc} (mW/cm²)	EQE (%)	Ref.
MEH-PPV:PCBM	2	~1.5	20		[68]
MDMO-PPV:PCBM (1:4)	3.16	4.3	27	30	[69]
MDMO-PPV:PCBM/LiF/Al (1:4)	5.25	2.5	80		[70]
MDMO-PPV:PCBM (1:4)	7.2	3.1	100		[71]
P3HT:PCBM (1:3)	8.7	2.8	100	76 at 550nm	[72]
P3HT:PCBM	8.5	3.5	100	70 at 500nm	[73]
p-m-MDATA/ZnPc:C_{60}/n-MPP	1.5	3.37	10		[74]
P3HT:PCBM (1:1)	10.6	4.4	100	63 at 550nm	[75]
P3HT:PCBM/TiOx (1:1)	12	5		90 at 500nm	[76]
pBBTDPP2:(C_{70})PCBM (1:2) low band gap material	11.5	4	100	40 [400 - 750]nm	[77]
PCPDTBT:(C_{71})PCBM low band gap material	16.2	5.5	100	50 [400 - 800]nm	[78]
PCDTBT:(C_{70})PCBM	10.6	6.1	100		[79]
low band gap polymer:PCBM	14.3	6.3	100	60 [400 - 750]nm	[80,81]

Table II-1: Overview of the state-of-the-art results in the field of bulk heterojunction organic solar cells and organic photodiodes.

Note that some reported results are a little misleading, especially for power conversion efficiency (PCE, η_p) which is the ratio of the maximum output electrical power density divided by the input light power density under "standard" test conditions (100 mW/cm²). With this I mean that one must relate this value to the incident power (P_{inc}). The PCE depends on the incident power and decreases with increasing power. The surface of illumination can also differ, and it should be noted that large area organic sensitive devices tend to be less efficient than smaller ones, due to the greater number of defects per device.
Within 7 years, solution process organic photovoltaic (OPV) power efficiency (measured under the same illumination conditions) increased by a factor of 2 and reached 6.3%.
Evaporated double heterostructure OPV also show high power efficiency of 5.7% [82]. Nevertheless, production costs are much less advantageous compared to the solution process bulk heterojunction.

d. Increase of charge carrier mobility

Charge carrier mobilities in bulk heterojunctions can be improved by controlling the film morphology such that the two phases form percolating paths along which the photogenerated carriers can be readily transported to their respective electrodes. Charge carrier mobilities in films of molecules and conjugated polymers often depend on the nanoscopic order, which can be influenced by the preparation conditions. For example, a preferential orientation of polymer backbones parallel to the substrate gives rise to anisotropic charge transport. The choice of solvent, atmosphere and substrate temperature can also be very influential. For example, (6,6)-phenyl-C61-butiric acid methyl ester (PCBM) – detailed more precisely in part III – is better soluble in chlorobenzene than in toluene. As a result, the short-circuit current density, and thus the efficiency is higher in the case of chlorobenzene. This can be explained by increased charge carrier mobility. Indeed, the tendency of the PCBM molecules to phase segregate into clusters is suppressed when chlorobenzene is used as the solvent [70].
By annealing the film after spin coating or exposing it to solvent vapour for several minutes it is also possible to influence the morphology of the blend and to reduce phase separation into discrete domains. For example, it was possible to enhance the performance of P3HT:PCBM devices dramatically in this way [73,83].
Generation of electric current under light illumination in organic semiconductors can also be very efficient. The photoresponse of semiconducting polymers can be further enhanced by photoinduced CT, which assists the separation of electrons and holes [84]. The discovery of photoinduced CT in composites of conducting polymers – which acts as donor – and buckminsterfullerene, C_{60}, and its derivatives – which acts as acceptor – provided a molecular approach to high-efficiency solar cells and high-sensitivity photodetectors. Since the time scale for photoinduced CT is below picoseconds (faster than all competing processes), the quantum efficiency of charge separation between donor and acceptor is close to unity in these systems.
A successful photodetector must have high photosensitivity or EQE at the operating wavelengths, high response speed, low noise, low dark current and, finally, long lifetime. In addition, the photodetector should be compact, use low biasing voltages or currents, and be reliable under the required operating conditions.
Most semiconducting polymers have band gaps that lie in the range 1.5 – 3 eV, which makes them ideally suited as optoelectronic materials for applications in the visible spectral range. Current OPD show EQE close or similar to ones obtains with inorganic semiconductors (Figure II.4).

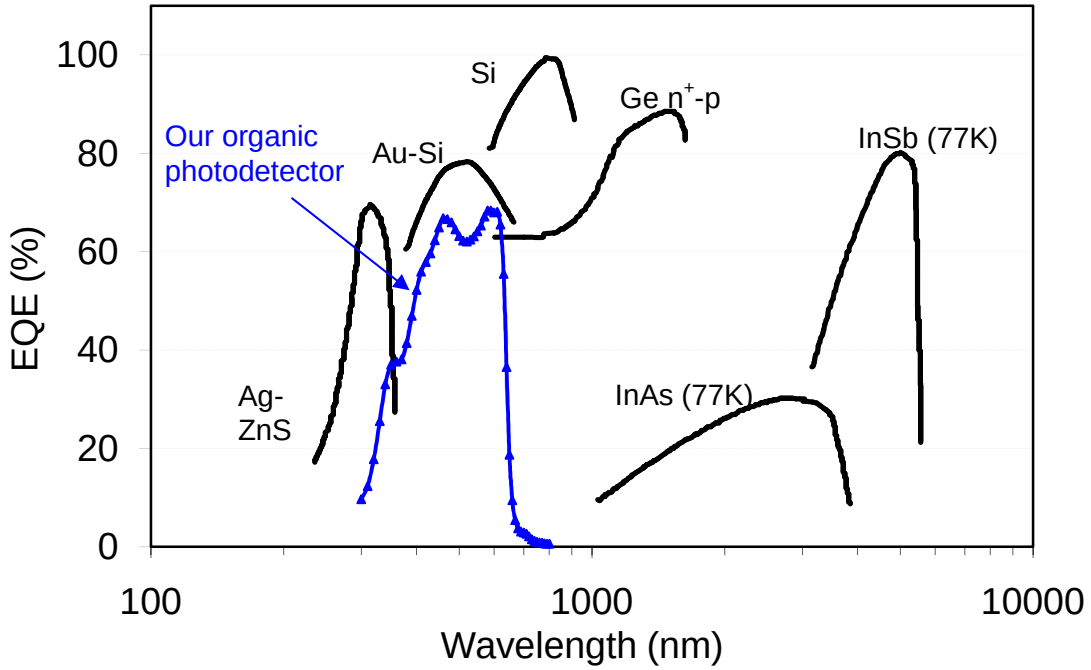

Figure II.4: Quantum efficiency versus wavelength for various inorganic photodetectors [85] and the organic photodetector developed in this work.

e. Relevant parameters

The EQE is the primary parameter reflecting the fundamental detection and charge transport properties of a photodetector. The external quantum efficiency, η_{EQE}, is defined as the number of electrons flowing in the external circuit per photon incident on the OPD, as shown in Equation II-11:

$$\eta_{EQE} = \frac{\Phi_{e^-}}{\Phi_{photon}} = \frac{\frac{\Delta J}{e}}{\frac{P_{ph}}{h \cdot \nu}} = \frac{\Delta J \cdot h \cdot c}{P_{ph} \cdot e \cdot \lambda}$$

Equation II-11

Here, P_{ph} is the intensity of the incident light (W/m²) and ΔJ the photocurrent density (A/m²) in the external circuit. The latter is usually determined by taking the difference between current measured under illumination and in the dark.
For a device based on exciton dissociation by charge transfer at a DA interface, the external quantum efficiency η_{EQE} is the product of the efficiencies of four sequential steps schematically illustrated in Figure II.2 and Equation II-12:

- photon absorption leading to the generation of an exciton η_A
- diffusion of the exciton to the DA interface η_{ED}
- exciton dissociation by CT at a DA interface η_{CT}, and
- collection of the free charge carriers at the electrodes η_{CC}

In summary,

$$\eta_{EQE} = \eta_A \cdot \eta_{IQE} = \eta_A \cdot \eta_{ED} \cdot \eta_{CT} \cdot \eta_{CC}$$

Equation II-12

where η_{IQE} is the internal quantum efficiency defined as the ratio of the number of carriers collected at an electrode to the number of photons absorbed in the device. The exciton diffusion (ED) efficiency η_{ED} is the probability that the photogenerated exciton diffuses to a DA interface before it recombines. Since the exciton diffusion length (L_D ~ 50 Å) [86] is typically shorter than the optical absorption length (L_A ~ 500 - 1000 Å), this step is often efficiency limiting. The charge transfer probability η_{CT} is close to 100% for the material systems used here [65]. Hence, Equation II-12 simply becomes $\eta_{EQE} \approx \eta_A.\eta_{ED}.\eta_{CC}$.
Both η_A and η_{ED} are functions of the optoelectronic parameters including optical properties of the materials employed, excitation wavelength λ, layer thicknesses and layer configuration; thus interference effect.

The on/off ratio is the ratio between the current under illumination and the dark current (Figure II.5). A prerequisite for a good photodetector is a low dark current. One of our goals was to reduce the off current in the polymer heterojunction diodes to acceptable levels (~ 100 nA/cm^2). The off current depends critically on the polymer layer thickness as well as on the residual dopants (and thus purity) in the polymers.

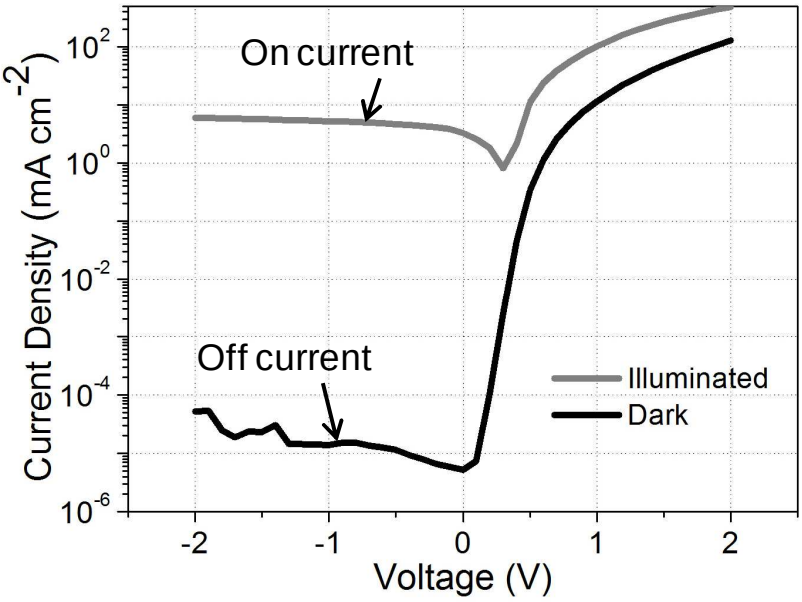

Figure II.5: I-V characteristic of a typical organic PD. Device structure is ITO/PEDOT:PSS/PCBM:P3HT/Ca-Ag.

f. Summary on OPD

To obtain a high photosensitivity, exciton dissociation at a DA interface must be preceded by efficient transport of the photogenerated excitons toward this interface, and followed by efficient charge extraction at low bias. Nearly complete transport of excitons to the DA interface is achieved by establishing an intimate contact between the donor and acceptor materials through blending. Bulk heterojunctions have proven to be a very successful concept to overcome the short exciton diffusion length of organic semiconductors. However, this structure enhances the disorder and hampers collection of photogenerated charge

carriers. Carrier mobilities are reduced, and charge-trap densities are increased. This appears to be a common property of ‘‘blended’’ materials where crystalline order and high purity are difficult to achieve.
Therefore, creating a bi-continuous and interpenetrating network between the donor and acceptor phase is of key importance. The use of high boiling point solvents and low spin speeds turned out to be a successful approach to increase the molecular order and thus the collection efficiency of charge carriers [87].

3. Photoluminescent materials

Photoluminescence (PL) is a process in which a substance absorbs and then re-radiates photons of lower energy.
By absorbing a photon or by applying an electric field, an electron of the outer-shell is excited to a higher energy level (excitation). When the electron drops back to the ground state, a photon of lower energy is re-emitted (de-excitation). The material will radiate as long as atoms are in the excited states, even if the pump-light source is off. This photoluminescence decays with the individual PL lifetime according to the de-excitation process.
The PL process can be divided in two broad categories: fluorescence and phosphorescence.

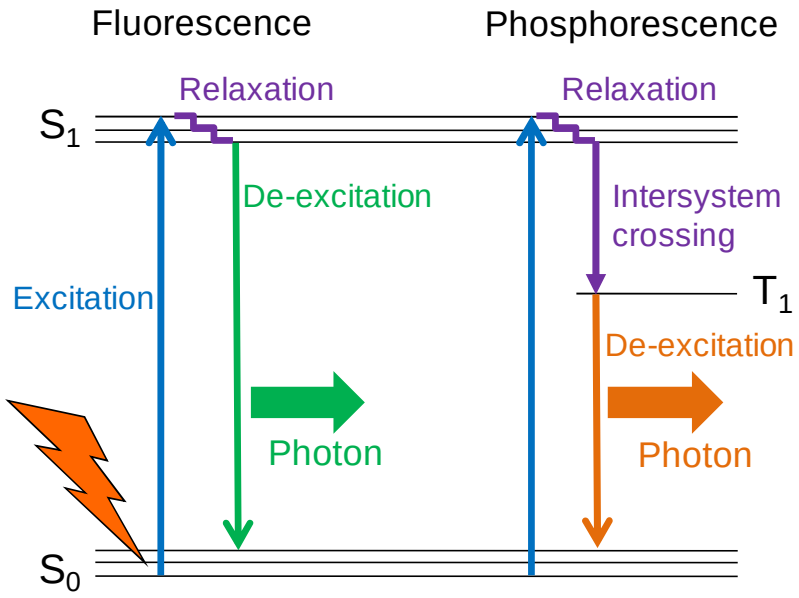

Figure II.6: Left: Fluorescence process. Right: Phosphorescence process.

a. *Fluorescence*

In the case of fluorescence (Figure II.6 and Equation II-13) – typically a fast process – excited charges undergo relaxation before de-excitation in which some of the original energy is dissipated so that the emitted light photons are of lower energy than those absorbed. The generated photon in this case is said to be red shifted, referring to the loss of energy as described.

$$S_0 + h\nu \rightarrow S_1 \rightarrow S_0 + h\nu$$

Equation II-13

For the fluorescence, fundamental state (S_0) and excited state (S_1) are both singlet states, since all electrons of spin +1/2 are combined to form a state of total spin 0. The energy state toward the excited system is also a singlet state, thus the electron can de-excite directly to the fundamental state. The timescale of this process is typically tens of nanoseconds.

b. Phosphorescence

In the case of phosphorescence (Figure II.6 and Equation II-14), the energy from absorbed photons undergoes intersystem crossing (ISC) into a state of higher spin multiplicity, usually a triplet state. Once the energy is trapped in the triplet state, transition back to the lower singlet energy states is quantum mechanically forbidden, meaning that it happens much more slowly than other transitions.

$$S_0 + h\nu \rightarrow S_1 \rightarrow \mathrm{T}_1 \rightarrow S_0 + h\nu$$

Equation II-14

From the meta-stable excited state (S_1), electron drop back to the ground state via the intermediate / transition state (T_1) which is a triplet state. To do so, electrons have to change their spin (from singlet to triplet). This process is known as intersystem crossing. A pair of electrons is thus separated, and 2 electrons are not bound, which gives three possible spin states named triplet. This ISC is energetically favorable (since it decrease the system energy), but very slow because involved energetic levels have a long lifetime. To drop back from the triplet state to the ground state (singlet), electrons have to change their spin again. As a consequence, phosphorescence is a slow process, measured in a few milliseconds to hours.

4. Biosensor working principle

Biosensors encompass two important features [88]: the molecular recognition element and the signal transduction mechanism. The molecular recognition element can take the form of a biomolecule (antibody, enzyme, or nucleic acid), biological system (membranes, tissues, or whole cells), or biomimetic component (synthetic bioreceptors) and imparts specificity to the system. The signal transduction mechanism is the process by which the biochemical recognition event is converted into a measurable signal, the intensity of which is proportional to the analyte concentration [89].
Biosensing materials, including enzymes, antibodies, nucleic acid probes, cells, tissues, and organelles, are able to selectively recognize target analytes. Transducers, including electrochemical, optical, piezoelectric, thermal, and magnetic devices, can quantitatively monitor the biochemical reaction. Biosensors, integrated with new technologies in molecular biology, microfluidics, and nanomaterials, have applications in agricultural production, food processing, and environmental monitoring for rapid, specific, sensitive, inexpensive, in-field, on-line and / or real-time detection of pesticides, antibiotics, pathogens, toxins, proteins, nutrilites, odors, microbes, and more in plants, animals, foods, soil, air, and water.
Optical biosensors can be divided in two broad categories: labeled and label-free sytems. In contrast to label-free, labeled configurations use a fluorophore – linked to the analyte – that will interact with the detection system chosen.
This chapter focuses on planar waveguide biosensors for labeled and label-free system along the lines of the group's research.

a. Fluorescent sensor

i. Principle

In the case of planar waveguide-based biosensors, the molecular recognition event results in the binding of a fluorophore at the surface of the planar waveguide. The planar waveguide provides the localized excitation light to generate a signal from fluorophores at the surface, but is not usually used to collect the light. Biosensor technology has the potential to both address fundamental scientific questions and to develop sensing systems for a variety of practical applications. However, in order to successfully develop commercial biosensors, the final product must offer a number of advantages over existing technology, such as the ability to perform faster, more sensitive, multi-analyte and real-time measurements, preferably with a portable, easy-to-use, stand-alone device.

For biosensor applications, total internal reflection fluorescence (TIRF) excitation of planar waveguides is the most utilized optical configuration [90,91]. With a history deeply rooted in the field of fiber optics, planar waveguide TIRF is a means of selectively exciting the fluorescence emission of fluorophores present near the surface of a waveguide and is relatively immune to bulk matrix effects. This technique has found numerous applications in the field of biosensors, in particular immunosensors and sensors for genetic analysis. TIRF biosensor-based systems take advantage of the waveguiding properties of the planar substrate, they are surface-selective in nature, and they excite only fluorophores present near the waveguide / sample interface to reduce background signals and to improve sensitivity.

The majority of the fluorescence microscopy-based techniques have until now been used to study biological processes and interactions rather than for the development of biosensing systems for commercial applications. Also, the instrumentation is often large and bulky and, while perfectly suitable for the laboratory, lacks the portability and stand-alone capability required for many biosensing applications.

There are several types of sensors that, under the condition of total internal reflectance, use the interaction of the resulting evanescent wave with the surface-bound species for signal transduction: attenuated total reflectance monitors alterations in the IR, visible, and UV regions; SPR and interferometric techniques measure variations in refractive index; and TIRF monitors changes in fluorescence [92]. The basic arrangement of the TIRF system is shown in Figure II.7.

Integrated optical waveguides, used frequently in TIRF studies, are single-mode and are prepared by depositing a thin film of high-refractive index material onto the surface of a glass substrate. These thin films are typically 80 - 200 nm in thickness and consist of inorganic metal oxide compounds such as tin oxide [93], indium tin oxide [94], silicon oxynitride [95], and tantalium pentoxide [96].

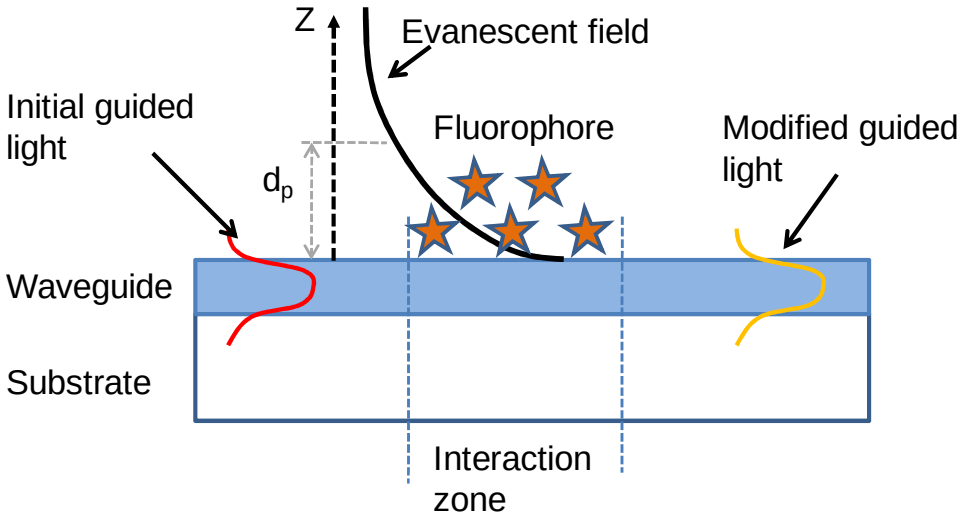

Figure II.7: The basic experimental arrangement of a system based on the principle of reflectance, with detection of the emitted fluorescence measured at right angles to the interface.

The light is coupled into these integrated optical waveguides (IOWs) via a prism or grating arrangement. The guided light is modified by the presence of the fluorophore located on the waveguide, within the penetration depth (d_p) of the evanescent field (Figure II.7). Studies comparing internal reflection element and IOW-based waveguides concluded that the integrated optics improves the sensitivity of the system by a factor of 100 [97].

ii. The molecular recognition element

The different types of binding events that are typically monitored via fluorescence measurements in affinity-based sensors include antibody-antigen interactions, nucleic acid hybridization (DNA / RNA), and receptor-ligand binding [98]. Affinity assays were originally performed using radio-labeled species; however, fluorescent markers are now the more common label of choice due to safety, longer shelf lives, lower cost, and ease of preparation, bio-conjugation, and disposal. Although a number of bio-molecules contain some intrinsic fluorescence in the form of amino acid residues or co-factors, often this fluorescence has weak intensity and low quantum yields. Therefore, extrinsic fluorescent probes are more often incorporated into one of the binding partners. The introduction of an extrinsic fluorescence probe, such a rhodamine, coumarin, cyanine, or fluorescein dyes, allows both: site and spectral selection. These commercial fluorescent dyes are available with a variety of reactive groups that permit simple attachment to the desired species. The Invitrogen handbook, “a Guide to Fluorescent Probes and Labeling Technologies” [99], is an excellent resource for choosing appropriate extrinsic fluorescent probes and suitable bio-conjugation techniques. The use of fluorescent markers is also favored over enzyme labels due to increased stability and because no additional substrates are required.
Antibodies and antibody fragments, because of their selectivity and sensitivity, have been the most popular choice of selective recognition elements for many biosensor applications. Monoclonal and polyclonal antibodies offer different level of affinities and specificities.
To date, immunoassays are the best-characterized systems employed in biosensors based on TIRF. The assays carried out using antibody-antigen systems can be divided into six main categories (Figure II.8): direct, competitive, displacement, sandwich, inhibition and ELISA immunoassays, of which competitive and sandwich are the most popular for TIRF biosensing.

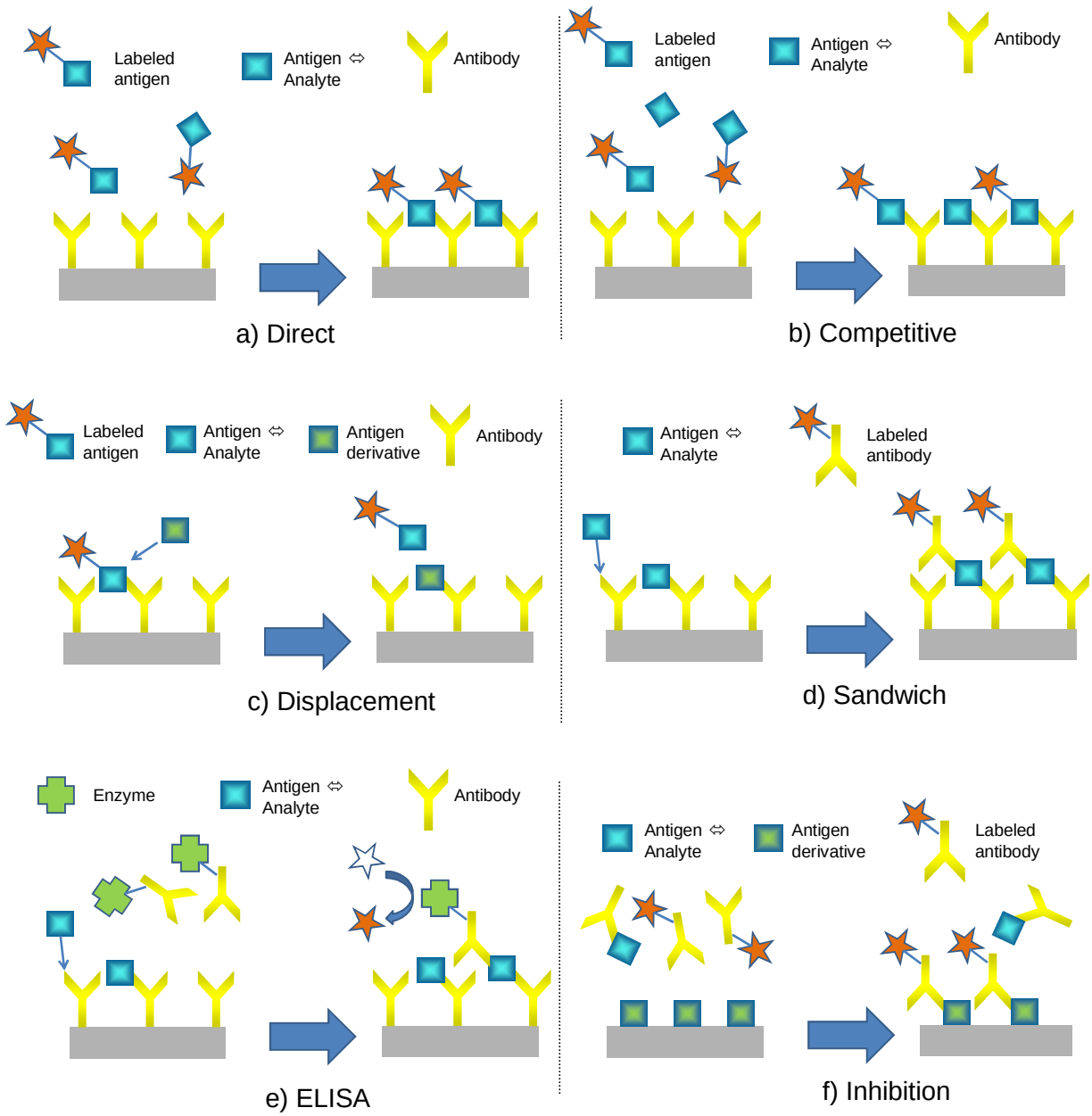

Figure II.8: Schematic representation of the six main categories of solid-phase immunoassays. (a) Direct assay measuring antigen captured from solution. (b) Competitive assays: (i) competition between a known concentration of the fluorescently labeled antigen and an unknown concentration of unlabeled antigen for binding sites on the immobilized antibody or (ii) competition for binding sites on the fluorescently labeled antibody between an unlabeled antigen in solution and immobilized antigen. (c) Displacement assay: fluorescently labeled antigen is pre-incubated with the immobilized antibody and is then displaced by unlabeled antigen from the solution. (d) Sandwich assay: the amount of immobilized antigen is determined by passing a second fluorescently labeled antibody over the antibody-bound antigen. (e) The ELISA: an assay in which the signal-generating partner is typically labeled with an enzyme. Addition of the appropriate substrate produces an absorbing, fluorescent or chemiluminescent signal. (f) In an inhibition assay, the sample is incubated with a fixed concentration of antibody. This incubation solution is then passed across a surface of immobilized analyte. Free antibody binds to the sensor surface, creating an inverse relationship between concentration of analyte in the sample and sensor response [88].

iii. Immobilization of the bio-molecule to the transducer

Various methods exist in which the biological component of a biosensing system can be immobilized onto the surface of the transducer, including physical adsorption, covalent bonding and entrapment in polymer matrices. Two important prerequisites of all immobilization techniques are that the functional integrity of the biomolecule is preserved and that the active site remains accessible to the binding partner. Each immobilization procedure has various advantages and disadvantages; however, physical adsorption and covalent binding to functionalized surfaces are the most commonly used in TIRF measurements. Physical adsorption of a biomolecule to a surface occurs via dipole-dipole interactions, van der Waals forces, or hydrogen bonding, depending on the nature of the substrate surface and the adsorbate. However, physical adsorption in general is not only strongly influenced by changes in the ambient conditions, such as pH and the solvent used, but may also be a reversible process. Furthermore, adsorption may not provide as high density of immobilized biomolecules as covalent immobilization [100]. Physical adsorption usually occurs in a random molecular orientation, resulting in the inaccessibility of the active binding site in at least a subpopulation of the immobilized molecules. Initial adsorption of a biomolecule can be followed by surface-induced denaturation and tighter attachment, with concomitant decrease in function.
On the other hand, covalent immobilization provides surfaces with reproducibly attached biomolecules at relatively high densities (e.g. 2 ng/mm^2 [101]). Most methods of covalent immobilization involve the activation of the surface (e.g., using silane or thiol self-assembled monolayers), followed by covalent linkage of the biomolecule either directly or by using a crosslinker.

iv. History

A number of the researchers currently involved in developing planar waveguide TIRF carried out much of their initial research in the field of fiber optics, including: Herron, Christensen, and Reichert (USA); Duveneck, Ehrat, and Neuschafer (Switzerland); Ligler (USA) and Bilitewski (Germany) and their coworkers.
Much of the history of planar waveguide fluorescence-based biosensors has involved development of both the technical components, including the optical design of the instrument used for surface analysis, and the biomolecule immobilization onto waveguide surfaces, both discussed in a previous paragraph. The evanescent wave excitation of a surface-bound fluorophore has been studied for a number of years using fiber optic technology. There are a number of advantages to use a planar waveguide instead of optical fibers, including the relative ease of preparation and integration into fluidic systems.
Planar waveguide TIRF is a sensitive technique with a limit of detection (LOD) typically between 0.1 and 200 ng/ml for proteins [96,102] and 10^3 - 10^5 cfu/ml (colony forming unit) for bacterial targets.
Depending on the target, these LODs are often found to be comparable with standard measurement techniques, such as ELISA, and yet the TIRF immunoassay can be carried out in a much shorter time, e.g., 10 - 45 min (TIRF) versus 2 h (ELISA).

b. Surface plasmon resonance

i. Principle

The potential of surface plasmons (SPs) for optical sensing was recognized in the early 1980s when SPs, excited in the Kretschmann geometry of the attenuated total reflection method, were used to probe processes at the surfaces of metals [103] and to detect gases [104]. Since then, numerous SPR sensors have been reported.

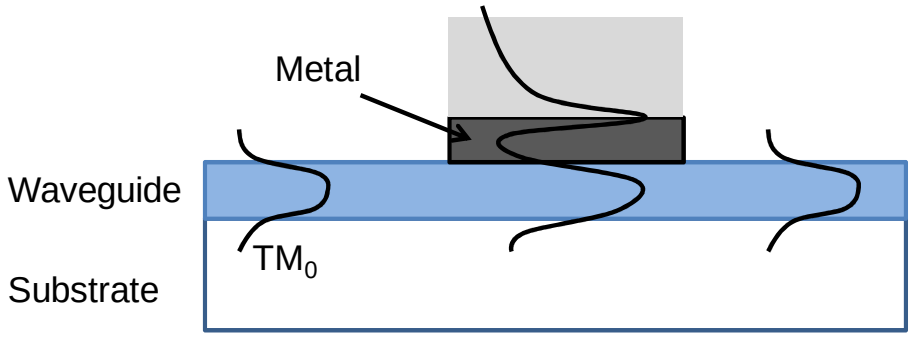

Figure II.9: Excitation of surface plasmons by a mode of a dielectric waveguide.

A SPR sensor instrument consists of an optical system, supporting electronics, and a sensor data acquisition and processing system. In the optical system, surface plasmons are optically excited, and the output light wave with an information-carrying SPR signal is detected. The signal from the detector is processed to yield a sensor output. SPR biosensors also incorporate a bio-recognition coating that interacts with target molecules in a liquid sample, and a sample preparation and handling system, as illustrated in Figure II.9.
In the optical system of an SPR sensor, surface plasmons are excited by a light wave. The excitation of surface plasmons in the SPR sensor results in a change in one of the characteristics of the light wave. Based on which characteristic of the light wave is modulated and used as a sensor output, SPR sensors can be classified as SPR with (i) angular, (ii) wavelength, (iii) intensity, (iv) phase, or (v) polarization modulation. The first three types of modulation are used most frequently in today's SPR sensors.
SPR-based biosensors can measure the interactions of biomolecules directly without the need for fluorescent labeling. This feature has allowed these analytical instruments to become essential tools for characterizing molecular interactions. The ability to directly measure interactions in real time allows us to quantitatively determine kinetic parameters, thermodynamics, and concentration, or qualitatively characterize relationships between ligands and analytes. Due to the fast response and high sensitivity of SPR-based biosensors compared to other technologies such as enzyme or radiolabeling methods, biosensors can be used to study a large variety of biomolecular mechanisms, ranging from protein-protein, antibody-antigen, and receptor-ligand interactions to the characterization of even low molecular weight compounds. Progress in surface chemistry enables the use of SPR-based platforms to facilitate capture of hydrophobic compounds such as lipids to study membrane-associated receptors.

ii. Detection Format

In SPR biosensors for detection of chemical and biological analytes, detection formats need to be chosen depending on the size of target analyte and whether detection or continuous monitoring is needed. Detection of analytes can be performed using either direct detection methods or indirect detection methods. In the case of direct detection methods, an analyte or

parts of an analyte are bound to the sensing surface producing the sensor response. Direct detection methods include direct detection of the analyte, sandwich assays, and competitive assays. In indirect detection methods, the analyte induces a change in the state of a secondary system component, which subsequently induces a sensor response. The most commonly used indirect detection method is the inhibition assay.
In a sandwich assay, as shown in Figure II.8 d, one antibody is immobilized on the sensor surface. The analyte-containing solution is then flowed over the sensor surface and analytes are captured by the immobilized antibodies. Following analyte capture, binding of a second antibody (normally a polyclonal antibody) to the analyte at the sensor surface is measured. This amplification has a twofold effect: improvement of lower detection limits and verification of the bound analyte (specificity).
Competitive assays, as shown in Figure II.8 b, are based on two analytes competing for the same recognition site at the sensor surface. One of the analytes is free and the other is typically conjugated to a larger protein, usually bovine serum albumin or casein. The concentration of the conjugated analyte is fixed from solution to solution. The two analytes are mixed in a solution and passed across the sensing surface. The sensor response will be inversely proportional to the concentration of analyte in the target solution.
In an inhibition assay, as shown in Figure II.8 f, the analyzed sample is pre-incubated with an antibody for the targeted analyte. Subsequently, the mixture is injected in the SPR sensor with an analyte derivative immobilized on the sensor surface, and the binding of the unreacted antibody to the analyte derivative is measured. As with the competitive assay, the sensor response is inversely proportional to the concentration of target analyte in the incubation solution.
Detection of medium-sized and large analytes (> 10000 Da) is usually performed directly [105]. Since direct binding of low molecular weight analytes at the sensor surface does not usually produce sufficient refractive index change, they are typically detected using a competition assay [106], sandwich assay [107], or inhibition assay [108].
SPR biosensors for rapid detection of chemical and biological analytes usually use direct or indirect assays in conjunction with high-affinity biorecognition elements. For these elements, their interaction with an analyte is, under normal conditions, irreversible. In SPR immunosensors, typically tens of regeneration-detection cycles are possible without significant reduction of activity of the biorecognition elements.

iii. Coupling to surface plasmons

The interaction between the surface charges and the electromagnetic field that constitutes the SP has two consequences. First, the interaction between the surface charge density and the electromagnetic field results in the momentum of the SP mode being greater than that of a free-space photon of the same frequency. Solving Maxwell's equations under the appropriate boundary conditions yields the SP dispersion relation [109,110], that is, the frequency-dependent SP wavevector, k_{SP}:

$$k_{SP} = k_0 \sqrt{\frac{\epsilon_d \epsilon_m}{\epsilon_d + \epsilon_m}}$$

Equation II-15

The frequency-dependent permittivity of the metal, ε_m, and the dielectric material, ε_d, must have opposite signs if SPs are to be possible at such an interface. This condition is satisfied for metals because ε_m is both negative and complex (the latter corresponding to absorption in the metal). As an example, using Equation II-15, the SP wavevector for a silver-air interface in the red part of the visible spectrum is found to be $k_{SP} \approx 1.03 \cdot k_0$. This increase in momentum is associated with the binding of the SP to the surface, and the resulting

momentum mismatch between light and SPs of the same frequency must be bridged if light is to be used to generate SPs.
The second consequence of the interaction between the surface charges and the electromagnetic field is that, in contrast to the propagating nature of SPs along the surface, the field perpendicular to the surface decays exponentially with distance from the surface. The field in this perpendicular direction is said to be evanescent or near-field in nature and is a consequence of the bound, non-radiative nature of SPs, which prevents power from propagating away from the surface.

c. Performance assessment of optical biosensors

The basic characteristic of a biosensor are:

- **Sensitivity:** the signal response of the sensor as a function of a change in substrate concentration.
- **Selectivity:** the ratio of the sensor response to a change in the concentration of analyte molecules compared with the response to a change in the concentration of other, interfering molecules. A biosensor of high sensitivity is of little use if the selectivity is low, since a change in signal level could be caused by a variation of the analyte molecule concentration as well as by a change of the concentration of the interfering molecules.
- **Linearity:** maximum linear value of the sensor calibration curve. Linearity of the sensor must be high for quantitative concentration detection.
- **Response time:** the time required for obtaining 95% of the signal response.
- **Stability:** the high selectivity and sensitivity of complex biological molecules is often counterbalanced by their inherent instability.

We detail here the two first parameters, sensitivity and selectivity.

i. Sensitivity

There are large differences in sensitivity and resolution between different detection approaches that are determined by the detailed characteristics of the biosensor evanescent field and optical losses in the sensor materials, among other considerations. The suitability of an optical biosensor for a particular application depends upon its performance across a variety of metrics. In this section, we will define some of the methods used to compare optical biosensors. Technological performance of an optical biosensor can be split into three main parts: sensitivity, assay sensitivity and limit of detection [111].

Sensitivity is defined as the amount of change in sensor output response resulting from a unit change in mass density on the sensor surface. The sensitivity in pg/mm^2 represents the sensitivity of the sensing device only, i.e. it represents the number of molecules you need per surface area of your sensor to have a signal above the background. It does not include any contribution from either the biology or the fluidics. Thus, it is not dependent upon the affinity between the analyte being detected and the immobilized ligand. It represents how efficiently the electromagnetic field associated with the optical transducer couples to biomolecules in contact with the sensor surface. Fundamentally, sensitivity is determined by the strength of light-matter interaction.
To determine this value, the background noise and the signal are measured for a known surface concentration and result in the signal to noise ratio. The surface sensitivity is then given by the value of the surface coverage which is 3 times above the background.
Sensitivity in immunoassay is the minimum detectable concentration of target in a sample and, practically, the amount of analyte required to obtain a signal above the background plus 3 times the standard deviations (σ). Assay sensitivity is typically defined in units of moles/volume or mass/volume of the analyte. Unlike mass sensitivity, assay sensitivity

depends on other factors besides the biosensor, such as surface chemistry, the affinity of the analyte for the immobilized ligand, buffer conditions, and the molecular weight of the analyte. Therefore, the sensitivity of a device is directly calculated from the concentration of the analyte that was necessary to obtain a signal.
Limit of detection in immunoassay terms is the minimum concentration that can be detected (not quantify) for the entire immunoassay. Experimentally, a dose-response curve with a known starting concentration for the analyte is used to determinate this parameter. The biosensor is coated with capture agent at maximum surface coverage. A sigmoid curve is obtained for the signal as a function of the analyte concentration. If one defines a signal to be detectable if the signal has a magnitude of 3σ, then the LOD, defined as the smallest measurable mass density change of the sensor, is LOD = 3σ/(sensitivity).

The sensitivity and the resolution are related but are entirely different figures of merit. Sensitivity is used to define the lowest value determined above zero concentration while the resolution describes the minimum resolvable difference between two measurements at any concentration.
Moreover, since all these sensors are sensitive to the refractive index (RI) change in bulk solution (or induced by molecules binding), LOD in units of refractive index units (RIU) is naturally and often used to quantify the sensor performance, which enables a rough comparison of the sensing capability among different optical technologies and structures.

ii. Selectivity

The basic operation of a biosensor relies on a two-step process: firstly, a chemical reaction between the analyte molecule and a well-controlled receptor or reporter molecule takes place. Secondly, the result of this chemical reaction is determined with a physical measurement technique. Because of the sensitivity, simplicity, speed and low cost of working with photons, many biosensors employ optical measurement techniques for this second step. Indeed, it has been shown that the presence of a single analyte molecule binding to a receptor molecule on a surface can be detected with optical means [112].
In biological specimens, a large number of different molecules in hugely variable concentrations are present. As an example, human plasma contains several hundred different proteins with a dynamic range in concentration of more than 10 orders of magnitude [113]. It is therefore of most importance that a biosensor's change in signal level is caused by the presence of the analyte molecule of interest and not by one of the many other molecules present. For this reason, the diagnostic value of a biosensor critically depends on the selectivity of the sensing principle. A large part of this selectivity is rooted in the selectivity of the chemical reaction, which must be exceedingly well chosen for a biosensor of practical relevance.
This chemical selectivity of biosensors is provided by enzymes, proteins, antibodies, DNA fragments, etc. These are complex molecules, but each with a unique and highly specific key-in-lock recognition of particular analytes. The technologies now found in simple biosensors are the same breakthroughs that have given us biochips [114]. Improvement in the selectivity of biosensors may be sought at two levels; the interface between the transducer and the biological receptor may be made more exclusive thus reducing interference, and new receptors can be developed with improved or new affinities.
The practical reliability of biosensors for given samples depends both on their selectivity and their reproducibility. It has to be determined under actual operating conditions, i.e. in the presence of possibly interfering substance. In order to be reliable for an analyst, the biosensor response should be directly related to the analyte concentration and should not vary with fluctuations of concentrations of interfering substances within the sample matrix. Thus, for each type of biosensor and sample matrix, one should clearly state the reasonable interference that should be considered and how its influence should be quantified. This reliability determination is necessary for accuracy assessment for each application [115].

5. Evanescent in-coupling theory from Lambertian emitter into single-mode waveguide

In this section, the theory of coupling OLED radiation into a single-mode waveguide is detailed. An OLED is a Lambertian, incoherent, thin-film light source. Channeling light from this “large-area” emitter into a waveguide of typically a few 100 nm thickness is a challenging task. Using standard approaches such as focusing the light source onto an end face of the waveguide yield poor coupling efficiencies in the case of OLEDs due to the fact that it is impossible to focus the light of the “large-area” OLED to a satisfactory degree. This is the reason why an evanescent coupling scheme has been chosen, where the OLED is brought into close vicinity of the waveguide (Figure I.4 a).
No commercial calculation tools are available to calculate coupling efficiencies of OLED emission to waveguide modes in a straightforward manner. Therefore, a method of calculation has been developed, which allows predicting how the emission from local oscillator couples evanescently into the modes of a waveguide.
A summary of the theoretical basis is presented here, with special emphasis on the calculation of evanescent emission into an adjacent waveguide. Further details and references can be found in the cited articles. This part is based on a publication made during this thesis [116].
The method can be summarized as follows:

1. The emission is expressed in the form of vertical or horizontal dipoles.
2. The dipole emission is expressed in a plane wave expansion in two polarizations, TE (s) and TM (p).
3. The effect of the environment is included in the waves reflected back to the source. This is usually carried out using the transfer matrix formalism which is suitable for arbitrary multilayer stacks.
4. Converting the electric field to the emitted power, the effect of refraction has to be taken into account along with the change of the solid angle in the changing medium.
5. Guided waves lead to poles in the expression for a lossless medium; however any loss widens this pole so that the modes become visible.
6. Finally, the emission is normalized with respect to the total emitted power.

This approach is quite general and can treat on an equal footing propagating plane waves, guided modes, surface plasmons, the change in spontaneous emission rate (Purcell effect), and radiative damping of a nearby metal.
Most of the following is adapted from Benisty *et al.* [117], which gives the basic theory underlying the model we used, with the exception of Equation II-28 and Equation II-30 which are a crucial development for the modeling of OLED emission into high index waveguides. This theoretical model has been established for the SEMOFS project and for my thesis with generous cooperation and participation of Ross Stanley from CSEM Neuchâtel.
For every application, the various material indices and thicknesses, as well as source peculiarities imposed by technology have to be taken into account. In this context, transfer-matrix techniques are widely used tools for calculating the optics of layered systems, usually with respect to externally impinging plane waves [118].
However, dipole emission requires a somewhat different treatment due to the possible coupling of the dipole near-field to electromagnetic modes with arbitrarily large wave vectors. It was extensively studied for simple cases with few interfaces [119-122]. Use of the Hertz vector dominates the initial literature [120], with the inconvenience of not separating explicitly the s (TE) and p (TM) polarizations. More convenient formulations in this respect are those of Lukosz & Kunz [123-126], as well as Ford & Weber [121,127].

a. Source terms for plane waves

Source terms are introduced as an additive discontinuity of the (scalar) fields chosen to represent electromagnetic waves in a given TE or TM polarization across the dipole layer according to the general form:

$$\begin{pmatrix} E_{12\uparrow}(\theta_1) \\ E_{12\downarrow(\theta_1)} \end{pmatrix} - \begin{pmatrix} E_{10\uparrow}(\theta_1) \\ E_{10\downarrow}(\theta_1) \end{pmatrix} = \begin{pmatrix} A_{\uparrow}(\theta_1) \\ A_{\downarrow}(\theta_1) \end{pmatrix}$$

Equation II-16

where subscript arrows ↑,↓ denote the +*z* and -*z* (Figure II.10) side of the dipole layer (*z* is the layer common axis), and all parentheses contain some adequate (2 x 1) representation of waves of a given $k_{//}$ and polarization. *A*↑ and *A*↓ represent dipole emission in +*z* and -*z*, respectively. θ_j is the angle taken between the wavevector and the *z* axis.

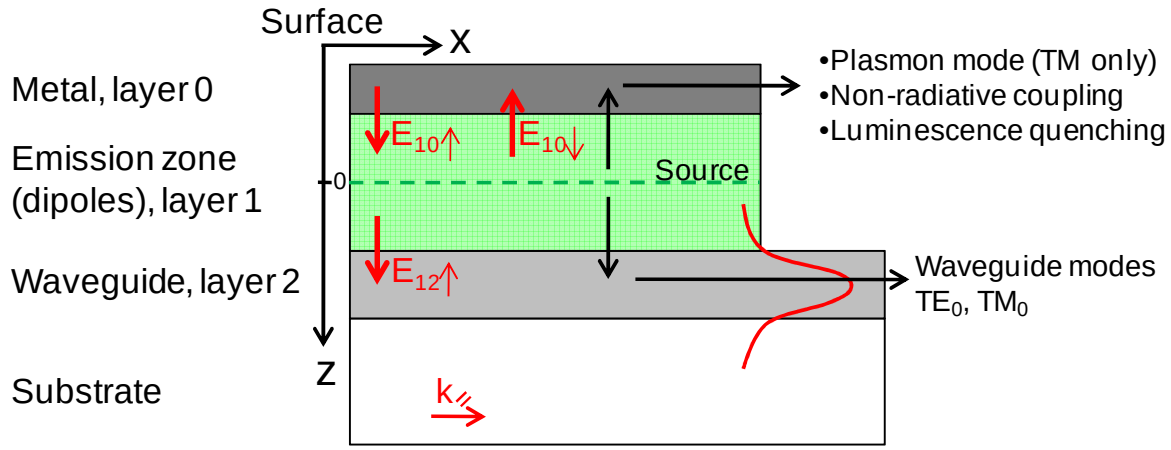

Figure II.10: Electric field (and the related power flow) representation in a PLED for evanescent waves emitted by the source. Plasmon mode at metal/PLED interface, non-radiative coupling or quenching due to the metal which occurs only when the source is close (< 20 nm) from the metal, and waveguide modes in the Ta_2O_5 waveguide are represented.

In the plane-wave basis, fields depend on layer indices n_j only through their complex *z*-wavevector component $k_{z,j}$, which obeys the wave equation:

$$k_{z,j}^{\,2} + k_{//}^{\,2} = \frac{\omega^2}{c^2} n_j^{\,2}$$

Equation II-17

These quantities are related to the following reduced variables:

$$\gamma_j^{\,2} + n_{eff}^{\,2} = n_j^{\,2}$$

Equation II-18

of which the effective index n_{eff} is often used to characterize guided modes. We shall however express our results directly in terms of wave vectors. For propagating waves, $k_{z,j}$ is real ($k_{z,j} = \omega \cdot n_j \cdot \cos\theta_j / c$, with angles θ_j taken between the wavevector and the *z* axis) and becomes purely imaginary for evanescent waves in a lossless dielectric. The root sign in

Equation II-17 is chosen to give a positive (or zero) real and imaginary part for the +*z* direction for a lossless or absorbing media. The use of $k_{z,j}$ is thus convenient to treat plane and evanescent wave on the same footing and $k_{//}$, is conserved throughout all interfaces.
Plane waves (both propagating and evanescent) are subject to reflections, transmissions, etc., which can be calculated, without any approximations, if the Fresnel coefficients are taken as a function of dielectric constants **ε**'s and k_z's rather than the usual angles [124].

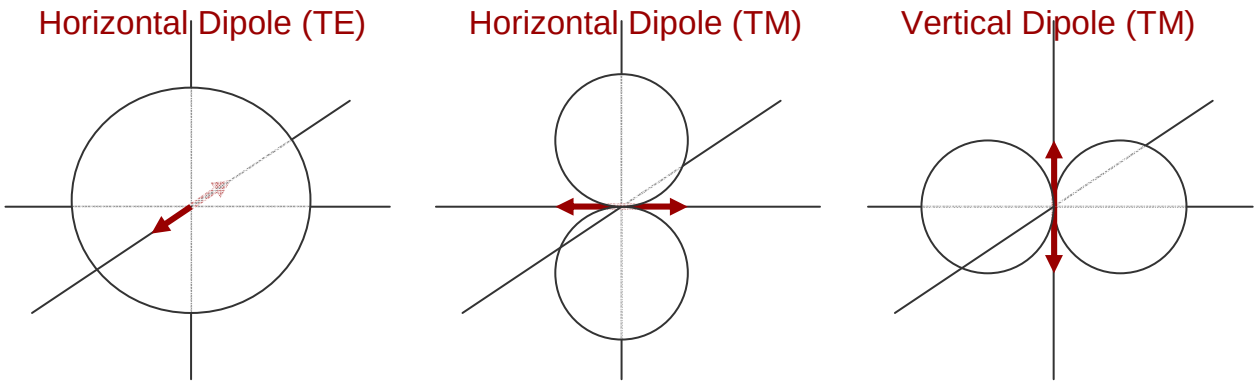

Figure II.11: Emission diagram for vertical and horizontal dipoles.

For electric dipoles, there are three basic configurations of interest. In Figure II.11, the simplest case, the vertical dipole denoted (*v*) radiates only *p* (TM) waves with a normalized pattern (power per unit solid angle) [117,124]:

$$\left(\frac{dP}{d\Omega}\right)^{(\mathrm{v})} = \frac{3}{8\pi}\sin^2\theta_1$$

Equation II-19

Where θ_1 is the off-normal emission angle and the total power through 4π steradians is unity. Subscript 1 refers to the emitter's medium and $\mathrm{k}_1 = n_1 \cdot \omega / c$.
For the horizontal dipole denoted (*h*), we take as a basis the two cases depicted in Figure II.11 for *s* (TE) and *p* (TM) polarizations. Normalization of the total (*s* + *p*) radiated power per (*h*) dipole gives:

$$\left(\frac{dP}{d\Omega}\right)^{(\mathrm{h}),\mathrm{s}} = \frac{3}{16\pi}$$

$$\left(\frac{dP}{d\Omega}\right)^{(\mathrm{h}),\mathrm{p}} = \frac{3}{16\pi}\cos^2\theta_1$$

Equation II-20

If we express the above source terms as a function of $k_{//}$ and $k_{z,1}$, and allow all values of $k_{z,1}$ required by the highest medium index in the multilayer (e.g. for evanescent waves in a lossless medium, by letting $k_{z,1}$ go from $n \cdot \omega / c$ to 0 from normal to grazing incidence, and beyond, for evanescent waves, from 0 to +∞) we will have the proper generalization of our source terms.

Let us start with the vertical (*v*) dipole layer located in the $z = 0$ plane and look for source terms of progressive waves propagating along $\pm z$ and with some value of $k_{//}$; such normalized terms are basically square root of power per unit solid angle, hence

$$A_{\uparrow,\downarrow}^{(\mathrm{v}),p} = \sqrt{\frac{3}{8\pi}} \sin\theta_1 = \sqrt{\frac{3}{8\pi}} \frac{k_{//}}{k_1}$$
$$A_{\uparrow,\downarrow}^{(\mathrm{v}),s} = 0$$

Equation II-21

where we substituted $k_{//} / k_1$ for $sin\,\theta_1$ and we denote $\uparrow,\downarrow$ for $+z$ and $-z$ directions.
The horizontal dipole has the following source terms (note: the direction signs are reversed):

$$A_{\downarrow,\uparrow}^{(\mathrm{h}),s} = \pm \sqrt{\frac{3}{16\pi}}$$
$$A_{\downarrow,\uparrow}^{(\mathrm{h}),p} = \pm \sqrt{\frac{3}{16\pi}} \cos\theta_1 = \pm \sqrt{\frac{3}{16\pi}} \frac{k_{\mathrm{z},1}}{k_1}$$

Equation II-22

We briefly recall that the field in layer *j* from z_j to z_{j+1} can be represented by a (2 x 1) vector as a sum of two waves according to

$$E(z) = E_{j\uparrow}^{s,p} \exp(ik_{\mathrm{z},j}(z - z_j)) + E_{j\downarrow}^{s,p} \exp(-ik_{\mathrm{z},j}(z - z_j)) \equiv \begin{pmatrix} E_{j\uparrow} \\ E_{j\downarrow} \end{pmatrix}_{s,p}$$

Equation II-23

separately for each polarization and the $exp\left(i\left(k_x \cdot x + k_y \cdot y - \omega t\right)\right)$ factors have been dropped.

b. Transfer matrix formalism for the calculation of the outside field

Let us write down the algebraic solution of the matrix propagation method in order to determinate the outside field from reflection and transmission coefficients. Additive source terms ($A\uparrow$, $A\downarrow$) impose the required additional relation between field-vectors on each side of the source layer:

$$\begin{pmatrix} E_{12\uparrow}(\theta_1) \\ E_{12\downarrow(\theta_1)} \end{pmatrix} - \begin{pmatrix} E_{10\uparrow}(\theta_1) \\ E_{10\downarrow}(\theta_1) \end{pmatrix} = \begin{pmatrix} A_{\uparrow}(\theta_1) \\ A_{\downarrow}(\theta_1) \end{pmatrix}$$

Equation II-24

With angles θ_j taken between the wave vector and the *z* axis.

Outside fields are easily calculated for the desired modes by writing down the matrix relations:

$$\begin{pmatrix} a_{11} & a_{12} \\ a_{21} & a_{22} \end{pmatrix}\begin{pmatrix} 0 \\ E_0(\theta_0) \end{pmatrix} = \begin{pmatrix} E_{10\uparrow} \\ E_{10\downarrow} \end{pmatrix} \quad ; \quad \begin{pmatrix} b_{11} & b_{12} \\ b_{21} & b_{22} \end{pmatrix}\begin{pmatrix} E_2(\theta_2) \\ 0 \end{pmatrix} = \begin{pmatrix} E_{12\uparrow} \\ E_{12\downarrow} \end{pmatrix}$$

Equation II-25

One finds by e.g. the left outside field E_0:

$$E_0 = \frac{b_{21}A_\uparrow - b_{11}A_\downarrow}{a_{22}b_{11} - b_{21}a_{12}} = \frac{t_0(r_2A_\uparrow - A_\downarrow)}{1 - r_0\, r_2}$$

Equation II-26

With t_j, r_j respectively the amplitude transmission and reflection coefficient in layer *j*.
The physical interpretation now becomes clear. The outgoing electric field on the top side (E_0) of the structure is due to the down (+*z*) going source reflected off the down side (Figure II.10) of the structure, added to the top (-*z*) going source term transmitted through the top side of the structure. The denominator is related to the cavity quality factor *Q* (in the classical resonator framework) and gives the enhancement / inhibition effects of the multilayer structure. Note that for lossless guided waves, we have $r_0=r_2=1$, so that this equation diverges.
To calculate the full problem, we look at the flux at the source but to either side of the source layer itself:

$$E_{10} = \frac{(1-r_0)(r_2A_\uparrow - A_\downarrow)}{1-r_0r_2}\ ,\ E_{12} = \frac{(1-r_2)(r_0A_\downarrow - A_\uparrow)}{1-r_0r_2}$$

Equation II-27

For propagating waves the flux is just $|E_{10}|^2$, $|E_{12}|^2$. For evanescent waves the power is related to the work done by the electric field at the dipole. This is related to the electric field reflected from back to the dipole which needs to have the right phase for contributing to the overall generated power. This can be included by using the following equations, where sgn($k_{||}$) is the sign of $k_{||}$.

$$Flux_{01}(plane) = |1-r_0|\left|\frac{(r_2A_\uparrow - A_\downarrow)}{1-r_0r_2}\right|^2$$

$$Flux_{01}(evanescent) = 2im(r_0)\left|\frac{(r_2A_\uparrow - A_\downarrow)}{1-r_0r_2}\right|^2$$

$$Flux_{01} = \mathrm{Re}\left(\mathrm{sgn}(k_{||})(1-r_0)(1+r_0^*)\right)\left|\frac{(r_2A_\uparrow - A_\downarrow)}{1-r_0r_2}\right|^2$$

Equation II-28

The last line of Equation II-28 is the most general and is used in all our calculations and allows us to correctly deal with all guided modes and all near-field effects of metals such as surface plasmons and non-radiative damping.

To treat non-averaged emission patterns in the (*h*) dipole case, see [124]. For a completely isotropic source (isotropic dipole matrix element: bulk semiconductors, etc.), we have the obvious rule:

$$P^{(\mathrm{iso})} = \frac{2}{3} P^{(\mathrm{h})} + \frac{1}{3} P^{(\mathrm{v})}$$

Equation II-29

Spectral spread of the source (line shape) may be accounted for by summation of normalized patterns at each wavelength with adequate weighing.
In either a mono- or a polychromatic case, integration of the power flux (Π) according to

$$P_{\mathrm{extracted}} = \int_0^{\pi/2} 2\pi \ \Pi(\theta) \ \sin\theta \ d\theta$$

Equation II-30

yields the extracted power on the chosen side.

c. Guided modes

Calculation of such fluxes is very helpful to quantify power emitted into discrete guided modes of structures containing layers of higher index than the outside world. For such modes the field complex amplitude allows self-sustained waves in the absence of damping. Consequently, at angles (propagation constants) of these modes, the field response to any coupled source term diverges, for example the total field $E_{10\uparrow} + E_{10\downarrow}$ in our approach. Residues at these poles indeed scale like the coupling strength of source to each mode. However, as soon as damping is nonzero, fields remain finite.
The first step is to intentionally introduce a minute damping through absorption in a thin layer adjacent to the source on any side [128]. Then, power injected in guided modes necessarily and inevitably goes to the absorbers. It quantitatively appears through the unbalance of power fluxes at any location between the source layer and the absorber. If absorbers such as lossy metal layers (contacts...) exist in the original system, no artificial damping layer is needed, but only knowledge of the unbalance. The damping layer should be close to the source to ensure it has the same coupling to guided modes as the source: a damping layer close to a node of a mode would have a vanishing coupling and it would yield a still more delta-like power flux if the same mode is indeed coupled to the source.
Finally, a dipole will always couple non-radiatively to a metal through its near-field. In this approach, this is equivalent to evanescent waves which propagate power into the metal, especially at large wave vectors.

d. Distributed incoherent sources

This is the case where dipoles lie on a finite volume rather than on a sheet, across a thickness that cannot be neglected with respect to the internal wavelength. Dipoles may even be distributed among different layers, etc. A convenient procedure is to sum the emitted power from discrete sub-sources, with weighting coefficients if emitter concentration is not uniform along *z*.
The optical power toward the waveguide also shows a strong position-dependent effect (Figure II.12). At a distance below 100 nm of the source from the waveguide, the coupling efficiency rises dramatically with distance. Up to 45 % of the light can be coupled into an adjacent waveguide. The efficiency is high because the waveguide has a high index

(n = 2.2). The density of modes in free space follows n^2. In going from an index of 1.6 to 2.2 the ratio of modes is 52 % in the low index. For a single-mode waveguide the remaining 48 % are concentrated in this mode. Therefore a coupling efficiency of 45 % is consistent with the density of modes.

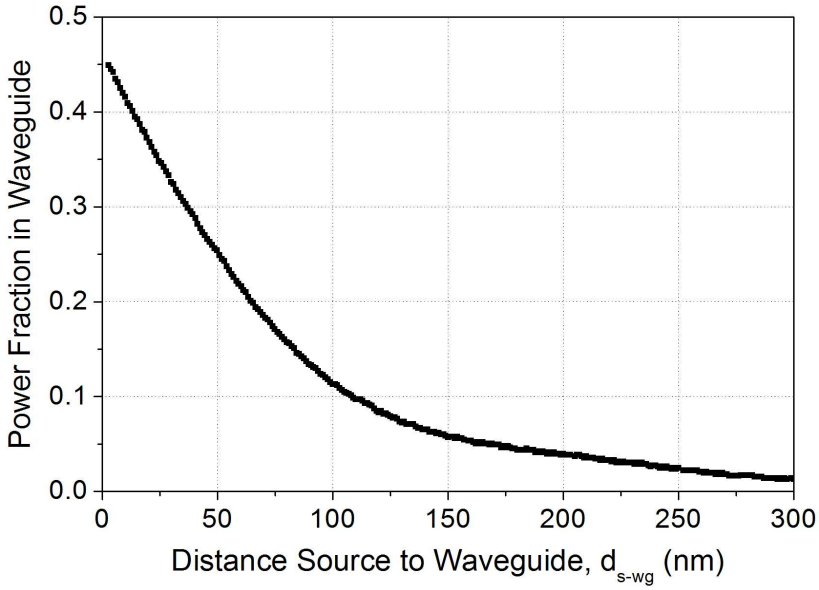

Figure II.12: Power fraction emitted into the waveguide as a function of distance between emission zone and waveguide for isotropic emitters.

The coupling scheme in this case is evanescent as the emitter is radiating into the evanescent field of the waveguide mode. It is this evanescent decay which dominates the coupling to the waveguide.
Therefore, it is possible to couple efficiently from an OLED to a single-mode waveguide using evanescent coupling.

e. Effect of ITO

A major challenge for OLED-to-waveguide coupling is the fact that an absorptive bottom electrode (ITO) is necessary in the OLED to inject / extract charges into / from the electroluminescent layers.
At 500 nm the refractive index of ITO is, $n_{ITO} = 1.97 + 0.04i$. The imaginary part corresponds to a material loss of 11 000 cm^{-1} or 1.1 μm^{-1}. This loss is low enough that for propagation perpendicular to the layer the loss is negligible. However, for propagation along the waveguide this loss is important. Indeed, in the case of a normal OLED the light traverses once the ITO layer vertically, but in a waveguide the light interacts with the ITO layer over the whole longitudinal distance.
We calculated the effective index of the mode with and without ITO:

Without ITO $N_{eff} = 2.04 + 6.90 \times 10^{-9} i$
40 nm ITO $N_{eff} = 2.06 + 2.68 \times 10^{-3} i$

Equation II-31

The loss is 6 orders of magnitude greater and corresponds to a modal loss of 680 cm^{-1}. The absorption length for this modal loss is 15 micron. Although we can couple light efficiently into the waveguide it is already completely absorbed after 30 micron. As a matter of fact only the last 20 - 30 micron of the OLED will effectively contribute to this coupling.

Bringing the emitters close to the waveguide – as required for efficient evanescent coupling – leads to increased waveguide losses. Therefore, one has to accept a trade-off between efficient coupling and acceptable waveguide losses. In practice, waveguide losses and coupling can be tuned by introducing an optical spacer layer between the waveguide and the bottom electrode of the OLED structure. A thicker spacer layer reduces the waveguide losses due to the presence of the bottom electrode of the OLED. On the other hand, it will result in a decreased evanescent coupling efficiency. A thinner spacer layer acts in the opposite way. In fact, it turns out from our simulations that the OLED-induced losses as well as the evanescent coupling efficiency both decrease approximately exponentially with increasing thickness of the spacer layer. Thus, it seems that nothing is to be gained by introducing a spacer layer. This is correct from a coupling efficiency point of view: placing the OLED at an increased distance from the waveguide indeed reduces losses, which, however, are cancelled by the reduced overlap of waveguide modes and OLED. From a practical point of view, on the other hand, the introduction of a spacer layer is advantageous or in some cases even a necessity, as shown in Figure II.13. The figure shows the loss of the waveguide as a function of the spacer layer thickness for a typical OLED-on-waveguide architecture. As seen from this figure, the losses of the waveguide underneath the OLED are of the order of 1000 cm^{-1} when no spacer layer is present. In other words, the intensity of the guided light is damped on a characteristic length scale of D = 10 µm. In other terms, only light coupled into the waveguide within 1 - 2 times D from the OLED edge survives. The residual light is being damped by the proximity of the OLED before it reaches the un-damped part of the waveguide not covered by the OLED. This implies that when no spacer layer is present, the edge of the OLED must be well defined on a length scale smaller than D. In conclusion, this implies that all the layers – especially the absorptive electrodes – must be patterned and aligned with respect to each other with a registration significantly better than D. In the absence of a spacer layer the registration would have to be 10 µm, i.e. a value not achievable with common deposition techniques used for OLED fabrication such as e.g. ink-jet printing and shadow mask evaporation. By introducing a spacer layer, the requirement in registration accuracy between the different OLED layers can be relaxed, which simplifies device fabrication considerably. For the model calculation depicted in Figure II.13, a spacer layer of about 130 nm reduces the waveguide losses to 10 cm^{-1}, which corresponds to a characteristic length D of 1 mm. In this situation a registration accuracy of 100 µm – a value that is easily achievable with standard OLED processing techniques – is fully sufficient.

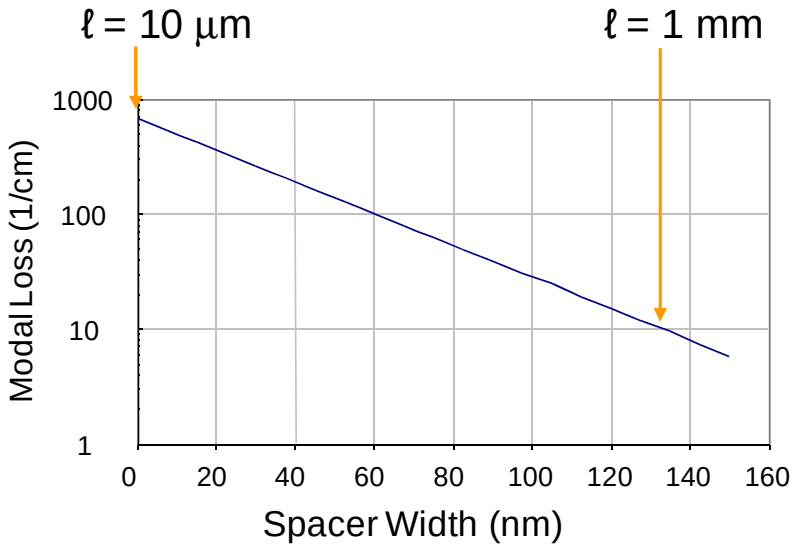

Figure II.13: Waveguide loss as a function of the thickness of the spacer layer between waveguide and OLED.

Within the model the magnitude of the coupling efficiency could be estimated as follows: let us assume an OLED of length L_{OLED} and width W_{OLED}, which emits F_{OLED} power per unit area. Neglecting dissipation in the absorptive anode, the coupling of the (electro-) luminescent layer shows a power efficiency $\eta_{w/o\ loss}$. The presence of the anode, however, induces a waveguide loss which damps the guided light on a characteristic length scale L_{loss}. Thus, the net power emitted into the waveguide can be estimated to:

$$P_{WG} \approx \eta_{w/o\ loss}\ F_{OLED}\ W_{OLED}\ L_{loss} \quad \text{if} \quad L_{loss} < L_{OLED}$$

$$P_{WG} \approx \eta_{w/o\ loss}\ F_{OLED}\ W_{OLED}\ L_{OLED} \quad \text{if} \quad L_{OLED} < L_{loss}$$

Equation II-32

In the former case only the part of the OLED that is within about L_{loss} of the OLED edge effectively contributes to the power in the waveguide. The overall coupling efficiency is thus

$$\eta = \frac{P_{WG}}{P_{OLED}} \approx \eta_{w/o\ loss} \frac{F_{OLED}\ W_{OLED}\ L_{loss}}{F_{OLED}\ W_{OLED}\ L_{OLED}} = \eta_{w/o\ loss} \frac{L_{loss}}{L_{OLED}} \quad \text{if} \quad L_{loss} < L_{OLED}$$

$$\eta \approx \eta_{w/o\ loss} \quad \text{if} \quad L_{OLED} < L_{loss}$$

Equation II-33

Let's first consider a device without spacer layer. In this case $\eta_{w/o\ loss}$ shows values of a few percent and $L_{loss} \approx 15$ µm. For the sake of this example, we set $\eta_{w/o\ loss} = 7.6$ %. With an experimentally realistic OLED length of $L_{OLED} = 200$ µm, we can therefore estimate the coupling efficiency to be $\eta \approx 0.6\ \%$.

By inserting a spacer layer into the device, the overall coupling efficiency does not alter significantly as explained above. This statement is only true as long as $L_{loss} < L_{OLED}$. Once the spacer layer surpasses a thickness for which the losses are diminished to such an extent that $L_{loss} > L_{OLED}$, the overall coupling would be reduced by about a factor L_{OLED}/L_{loss}.

6. Conclusions on the theoretical part

In conclusion, OLED and OPD theory is partially based on the inorganic counterpart theory. However, the amorphous structure of the organic devices makes the creation of a simple and unified theory difficult. As an example, the electron conduction band named HOMO (refer to the valence band for inorganic band theory) is not represented, in contrast to the inorganic case, by a discrete energy level. Doping, lattice deformation, geometric defects involve enlarging of the energetically band following a Gaussian behavior. Despite the low electrical conductivity of these materials, they exhibit interesting semiconductor properties. Their ease of processing – from solution – and the potential for low-cost production drive the research in this field with highest priority.

Another asset is the possibility to deposit such optoelectronic components in ultra thin layers at defined positions by additive process such as ink-jet printing. Thus integration of these devices is pretty simple. We have theoretically demonstrated the possibility to couple – by an evanescent scheme – OLED light into single-mode waveguides.

An overview of the biosensor working principle has been presented. Labeled and label-free are the main used techniques for optical biosensor. In this thesis, both are explored with the integration of organic components as light source and light detection.

Before using these organic devices, their performances were optimized in terms of efficiency, lifetime and deposition processes such as ink-jet printing.

III. Fabrication, characterization and optimization of the components used in the integrated biochip

As described in part I, the biochip consists of a single-mode waveguide, PLED, PL material, PPD, fluidic and plasmon stack. Each part will be presented in this chapter with special emphasis on PPD optimization and deposition process, as well as PL material and PLED architecture. Fabrication, optimization and integration of these organic components represent the main results of this work. As part of the description of the PLED, the ink-jet printing process will be closely examined. For the PPD, the spin coating process will be discussed in detail. Spin coating is mainly used for performing screening tests and ink-jet deposition for integration onto the biochip.

1. Waveguide substrate

At this stage, the only high-quality waveguide substrate commercially available in reasonable quantities is the opto-chip supplied to the SEMOFS consortium by the project partner Zeptosens [16] (now a division of Bayer). It is based on Ta_2O_5. Here we summarize those aspects of the opto-chip that are of particular relevance to the PLED-to-waveguide and PL material-to-waveguide coupling experiments described hereafter.
The opto-chip consists of a 14 mm x 57 mm x 0.7 mm AF45 glass substrate with a planar, 150 nm thick low-loss Ta_2O_5 waveguide. It also includes two identical 0.5 mm wide coupling gratings of 312 nm period and 12 nm depth etched into the substrate underneath the waveguide, as depicted in the schematic diagram of Figure III.1.

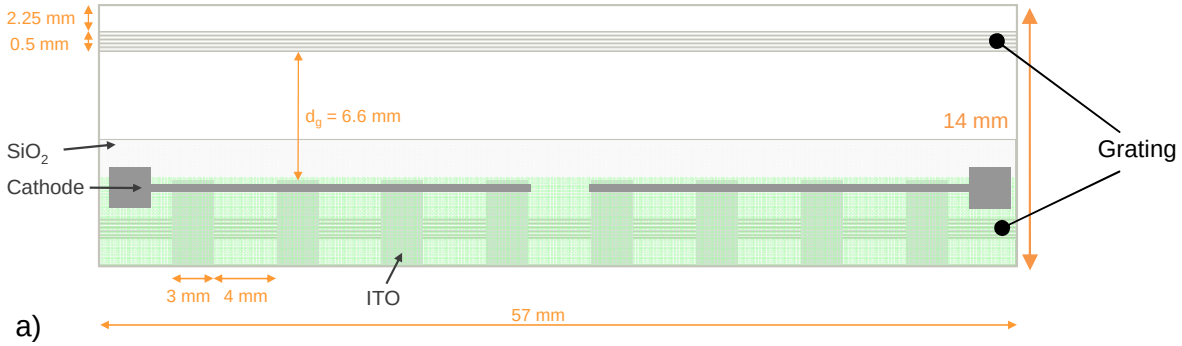

a)

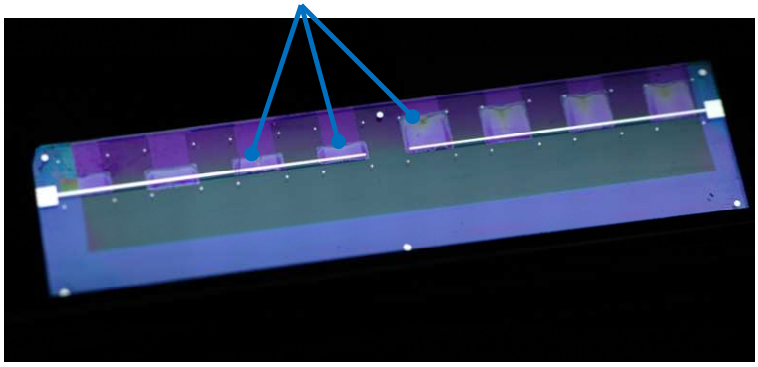

b)

Figure III.1: Opto-chip substrates with low-loss waveguides of tantalum pentoxide and in- / out-coupling gratings. (a) Top view. (b) Picture of the chip with printed PLED.

The 150 nm thick Ta_2O_5 layer results in a single-mode waveguide at visible wavelengths. The 8.5 mm propagation distances between the two gratings can be used to realize the sensor channels. Each opto-chip is divided into 8 individual sensors, defined by the PLED location. Instead of the PLED, a PL material was alternatively deposited at the same location.
The dispersion of the opto-chip waveguides is shown in Figure III.2. The waveguide characteristic effective refractive index N_{eff} curve for a 150 nm thin Ta_2O_5 layer has been calculated for the two fundamental modes under TE- and TM-polarization. The simulation software that has been used for these charts is based on textbook solutions of the waveguide mode equations. Based on the mode refractive indices, the coupling angles for the two modes are plotted as a function of wavelength. For the red He-Ne laser with 633 nm wavelength the coupling angles are -13.3° and -23.9 ° for TE and TM modes, respectively.
Onto the as-received opto-chip, a 50 - 130 nm thick SiO_2 layer was deposited (Figure III.10 for a cross view of the opto-chip with integrated PLED). This layer serves as the spacer layer described in the previous chapter in order to relax the requirements for registration accuracy for the different PLED layers. The SiO_2 was deposited by plasma-enhanced chemical vapor deposition (PECVD) at Comlab in Neuchatel, Switzerland, or by electron beam evaporation at CSEM. A subsequent, 2 hours annealing step at 450℃ turned out to be necessary in order to eliminate waveguide losses induced by the spacer layer.

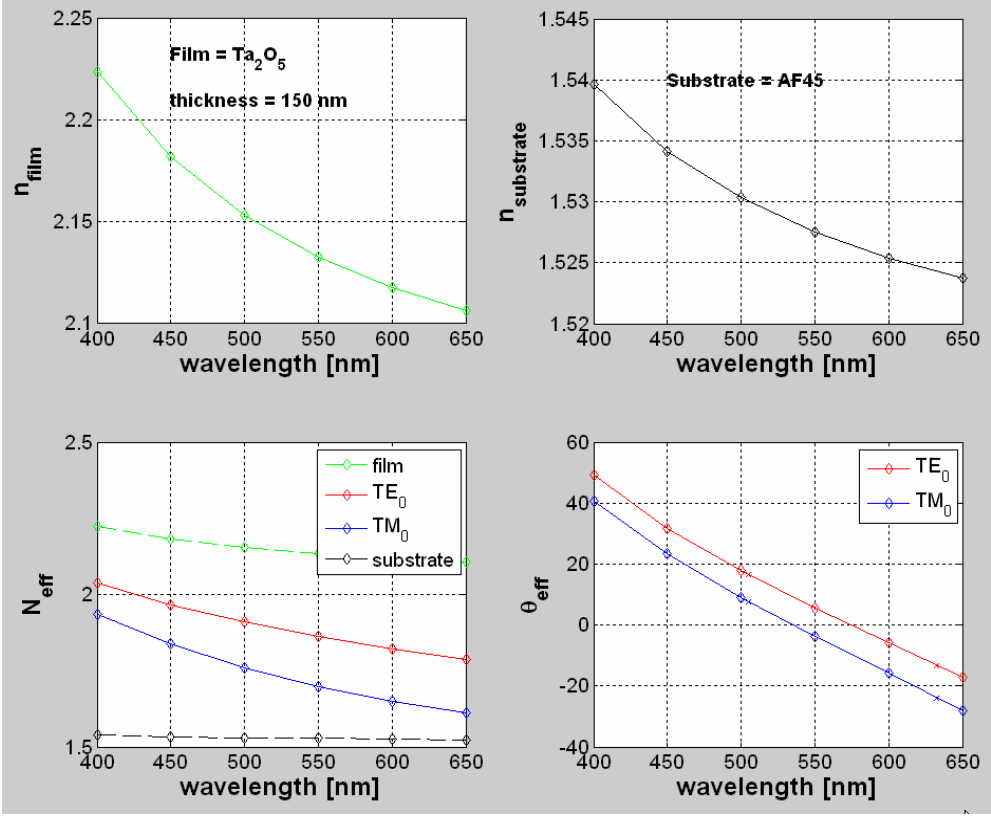

Figure III.2: Simulated waveguide characteristics of the opto-chip. Shown are the dispersion properties of the film refractive index (Ta_2O_5), the substrate refractive index (AF45 glass) as well as the effective refractive index values against wavelength and the grating coupling angles versus wavelength.

In order not to reduce the efficiency of the out-coupling grating, about a third of the width of the opto-chip was shadow-masked during the SiO_2 deposition, such that the out-coupling grating is not covered by the spacer layer.

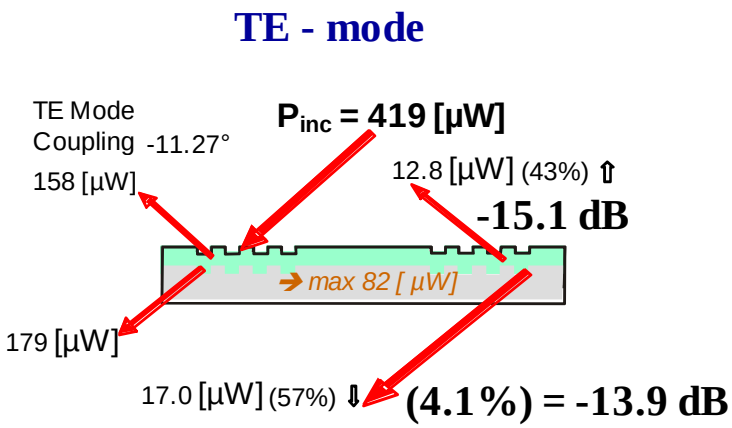

Figure III.3: Schematic diagram of the efficiency and loss measurements hybrid optical set-up using single wavelength He-Ne lasers and large area detectors.

Apart from the grating coupling angles the waveguide losses are another important key figure of the opto-chip waveguide system. Waveguide losses and grating coupling efficiencies of the as-received opto-chip as well as the modified opto-chip with spacer layer were carefully characterized using a laser beam. Table III-1 summarizes the results of these loss-characterization measurements and simulated losses.

		Simulated loss			
	Polarization	TE	TM	TE	TM
	Configuratoin: in-coupling out-coupling	cover cover		substrate substrate	
		[dB]	[dB]	[dB]	[dB]
	Beam diameter for in-coupling			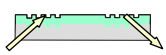	
150nm Ta2O5	0.5mm	**-12.96**	**-9.27**	**-9.14**	**-7.08**
	0.63mm	**-13.77**	**-9.57**	**-9.95**	**-7.32**
	1.3mm	**-16.63**	**-11.69**	**-12.80**	**-9.34**
		Measured loss			
150nm Ta2O5	0.63mm	**-15.10**	**-14.20**	**-16.23**	**-12.59**
		Simulated loss			
150nm Ta2O5 + inf. SiO2	0.5mm	**-9.43**	**-22.82**	**-9.03**	**-22.95**
	0.63mm	**-10.05**	**-23.00**	**-9.65**	**-23.12**
	1.3mm	**-12.58**	**-24.95**	**-12.19**	**-25.07**
		Measured loss			
150nm Ta2O5 + 500nm SiO2	0.63mm	**-15.91**	**-27.23**	**-12.59**	**-26.30**
150nm Ta2O5 + 150nm SiO2	0.63mm	**-14.40**	**-22.76**	**-10.82**	**-21.95**
150nm Ta2O5 + n=1.47 layer				**-14.91**	**-22.97**

Table III-1: Simulated and measured loss characteristics of opto-chips and opto-chips clad with silica layers under TE- and TM-polarisation. The loss characteristics have been simulated for two configurations with illumination and light collected from substrate or cover side and for different beam waist radii of the He-Ne lasers. The term inf. SiO_2 is an abbreviation for infinite SiO_2 and refers to a silica half-space on top of the waveguide.

The measured loss for the experimentally relevant system 150 nm Ta_2O_5 + 150 nm SiO_2 is

- -14 dB for TE polarization, cover-cover coupling
- -11 dB for TE polarization, substrate-substrate coupling
- -23 dB for TM polarization, cover-cover coupling
- -22 dB for TM polarization, substrate-substrate coupling

In the case of TE polarization the loss value is close to the one measured on the 150 nm Ta_2O_5 of the as-received opto-chip. This confirms that the annealed SiO_2 spacer layer does not induce significant additional waveguide losses.
In the case of TM polarization, the loss values measured on the SiO_2 covered opto-chip are substantially larger (by about 10 dB) than the ones obtained on the spacer-layer-free device. This is actually not due to enhanced waveguide losses for TM polarization, but originates from reduced coupling efficiencies of the SiO_2 covered gratings for TM-polarized light. From these measurements one concludes:

- A properly deposited and post-deposition-treated SiO_2 spacer layer does not significantly alter the waveguide losses in the opto-chip.
- In order not to lose grating coupling efficiency under TM polarization, the gratings must not be covered by the spacer layer.

The latter explains why the out-coupling grating was shadow-masked during the SiO_2 deposition.

2. Polymer light emitting diode fabrication on the biochip

Here, we present the deposition of the PLED onto the single-mode waveguide. This technique was the first in-coupling technique pursued within this thesis. Even if this technique presents some drawbacks, it is still a valuable step toward integration of organic optoelectronic devices. Moreover, it is the first time that such in-coupling – from Lambertian PLED emitter to single-mode waveguides – has been demonstrated.
As already mentioned, two types of OLEDs are under evaluation worldwide: OLEDs based on small molecular weight materials (SMOLEDs) and OLEDs based on polymeric light emitters, also referred to as PLEDs. Whereas the former are usually deposited by vacuum sublimation, the latter can be deposited from solution. This is generally believed to eventually lead to a cost-advantage of PLEDs over SMOLEDs, since PLED fabrication does not necessitate investment-intensive vacuum evaporation infrastructure. Additionally, solution processing offers completely new and attractive routes for monolithic integration in that a variety of different functional materials can be deposited by additive (print) processes in only those areas where their specific functionality is required, as exemplified by ink-jet printed red, green, and blue emitting pixels in polymer LED displays. In this sense, PLEDs are particularly suited for this work, which targets a disposable – and thus low-cost –, fully integrated sensor platform. All experiments described in this thesis have been performed using polymer light emitting devices.
The present work on PLED integration makes use of optimization results obtained by co-workers at CSEM. Here, we mainly focus on the integration of these PLEDs onto the biochip by using ink-jet printing techniques.
Onto the waveguide, a 50 - 130 nm thick SiO_2 layer was deposited. This layer serves as the spacer layer described previously. On top of the spacer, a PLED has been deposited. In a first step of the device fabrication, a 10 - 30 nm thick indium tin oxide (ITO) layer was magnetron sputtered. The ITO deposition has been performed at room-temperature under an atmosphere of 0.5 % oxygen in argon at a pressure of 5×10^{-3} Torr. The ITO deposition runs have been carried out by a partner at the Haute Ecole ARC in Le Locle, Switzerland. Next, the ITO was patterned using photolithography followed by wet etching. The ITO stripes serve as anode for the 8 PLEDs pixels (Figure III.1). After patterning, the substrates were carefully cleaned in ultrasonic baths of ultra-pure water and acetone. An oxygen plasma treatment

(Oxford Plasmalab, 80W, 20% partial pressure O_2) followed and the cleaning was finished by an ultrasonic bath of isopropanol. In a next step, the polymer layers were deposited. First, a 10 - 20 nm thin hole injection layer, poly(3,4-ethylenedioxythiophene) doped with poly-(styrenesulfonate), so called PEDOT:PSS, was deposited by spin coating at 2000 rounds per minute (rpm). The as-received PEDOT:PSS (BAYTRON P VP AI 4083 from H.C .Starck) was diluted 1:1 by volume with ultra-pure water. A self-adhesive polymer film was used to mask those areas of the chip that are not to be covered by the polymer films. After deposition the PEDOT:PSS was annealed at either 100℃ during 1 hou r or at 150℃ during 20 minutes.
The next layer of the integrated PLED is the electroluminescent (EL) polymer. Different green-emitting EL layers have been integrated onto the opto-chip, but the best results in terms of coupling efficiency and total optical power coupled into the waveguide have been obtained with a blend containing an iridium-complex emitter. Thus, only the details for the fabrication of this layer are given here. Within the SEMOFS project it was decided to work with green-emitting PLEDs. The reason for this is that among the organic EL materials currently available to CSEM, and not being subject to non-disclosure agreements with third parties, those emitting in the green exhibit significantly better quantum efficiencies and lifetimes compared to the ones emitting in the red and the blue. Moreover, simulation of this iridium based PLED – made with the program Setfos developed by Fluxim [129] – indicate an emission zone close to the ITO; which is a favorable case for the evanescent coupling.
This PLED is composed of a blend of four different materials as seen in Figure III.4, the electrophosphorescent metal complex iridium (III) tris(2-(4-totyl)pyridinato-N,C2) – $Ir(mppy)_3$ – from the American Dye Source; the hole transport material poly(9-vinylcarbazole) – PVK – from Aldrich; the hole transport material N,N'-Bis(3-methylphenyl)-N,N'-diphenylbenzidine – TPD – from Aldrich; and the electron transport material 2-(4-Biphenylyl)-5-(4-tert-butylphenyl)-1,3,4-oxadiazole – PBD – from Fluka. 5% : 47% : 22% : 26% by weight of $Ir(mppy)_3$: PVK : TPD : PBD have been dissolved in chlorobenzene to a total concentration of 23 mg/ml and 8 mg/ml for the deposition by spin coating and ink-jet printing, respectively.

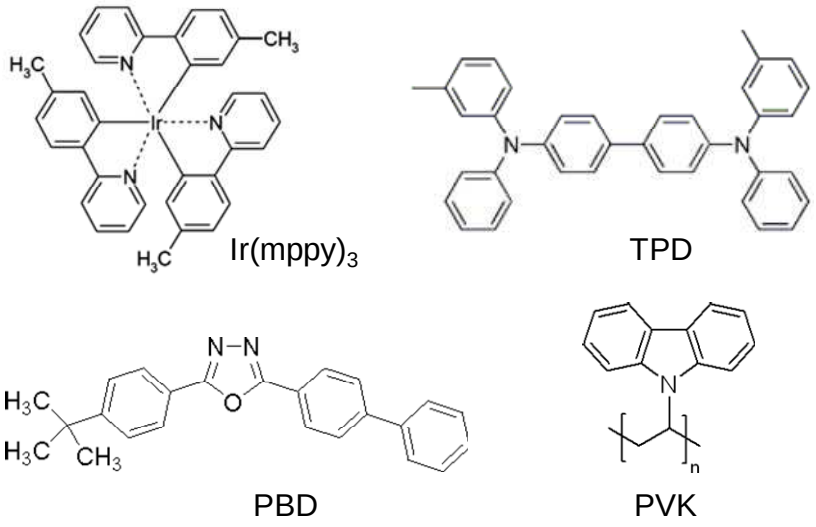

Figure III.4: Molecular structure of materials used in the active layer of the PLED.

Thus, two different deposition techniques have been used for the deposition of the EL polymer layer: spin coating and ink-jet printing. Spin coating of the electroluminescent polymer has been carried out using the same self-adhesive polymer mask as for the PEDOT:PSS structuring and a spin speed of 1000 rpm.

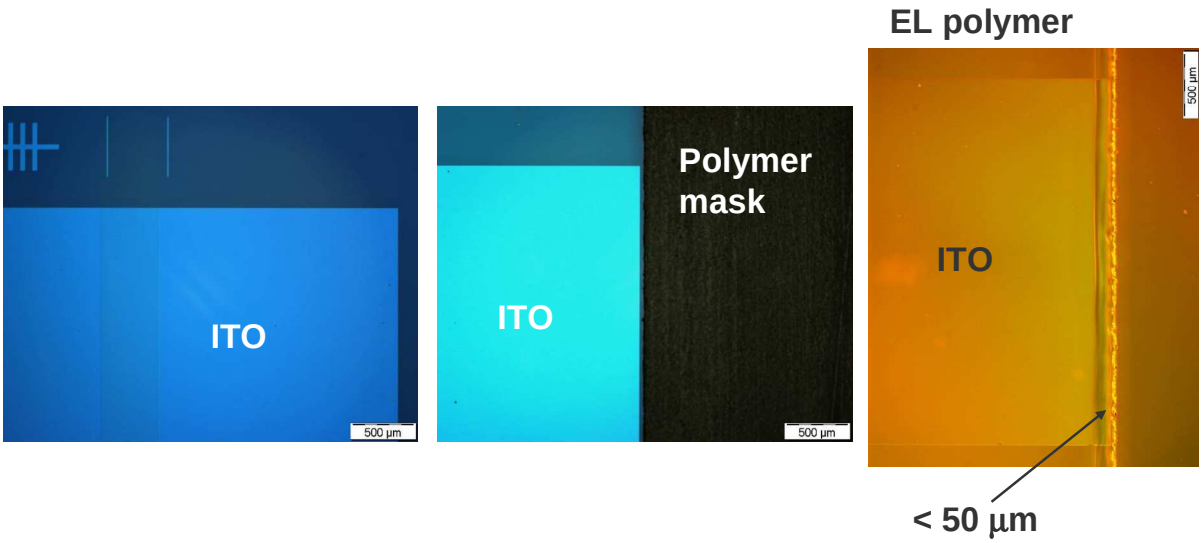

Figure III.5: Left: Micrograph of a patterned 30 nm ITO layer. The ITO shows in light blue. The vertical, 0.5 mm wide stripe faintly visible in the left part of the image is the coupling grating. Alignment marks for subsequent layers are seen at the top left. Center: Micrograph of an ITO pixel and the self-adhesive polymer mask used during PEDOT:PSS – and in some cases also the EL polymer – deposition. Right: ITO pixel covered with a PEDOT:PSS layer and the electroluminescent polymer film as deposited by spin coating. The edge of the polymer films can be clearly seen in the right part of the image. The registration of the polymer films with respect to the edge of the ITO pixel is better than 50 µm.

An Autodrop system (Figure III.6 a) with piezoelectric print heads from Microdrop [130] was used for ink-jet printing the EL polymers (as shown in Figure III.6 b). Droplets of 50 - 60 µm are generated by applying 80 - 100 V pulses to the piezoelectric actuator attached to the glass nozzle (inner diameter of 50 µm). The print head was positioned relative to alignment marks on the chip and the print layout was chosen such that the EL polymer overlaps the ITO edge by nominally 100 µm. By dispensing droplets close to one another with a precise x-y table, the thicknesses of the EL polymer layers deposited as described either by spin coating or ink-jet printing was around 50 nm.

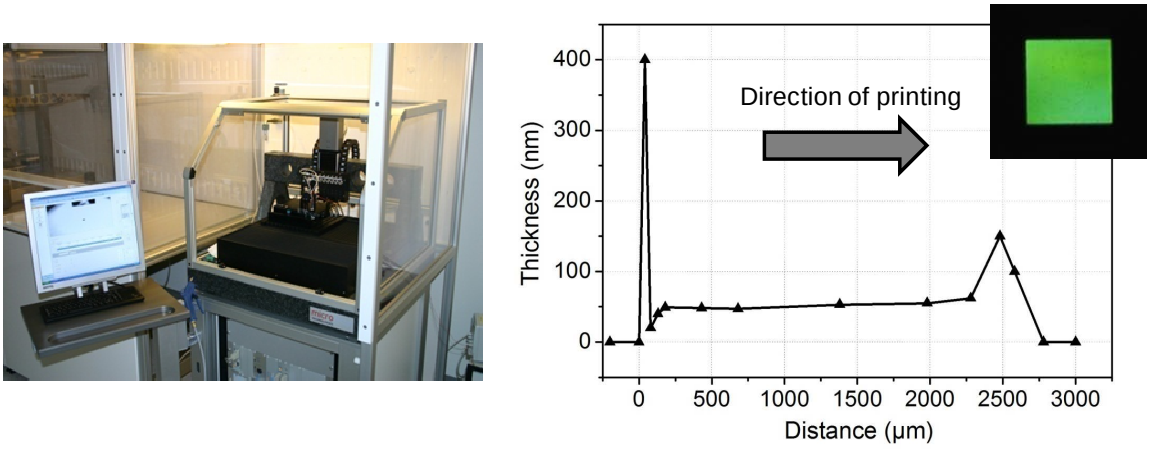

a) b)

Figure III.6: (a) Microdrop ink-jet printer and (b) printed green PLED.

In particular for PLED, layer homogeneity has to be well controlled in order to obtain constant illumination over the complete printed surface. Solvent exhibiting a boiling point higher than 100℃ has to be used in order to obtain stable drop lets and to avoid inhomogeneous layer [131].
Ink-jet printed PLEDs have been realized. The useful printing field, due to the absence of centrifugal force, is strongly affected by surface energy and cleanliness, molecule migration, phase separation and drying process. However by selecting the interior of the pixel as active area, using the appropriate solvent and treating the surface, a homogenous layer has been obtained (Figure III.6 b). In a final step, the cathode was deposited by physical vapour deposition through a shadow mask.

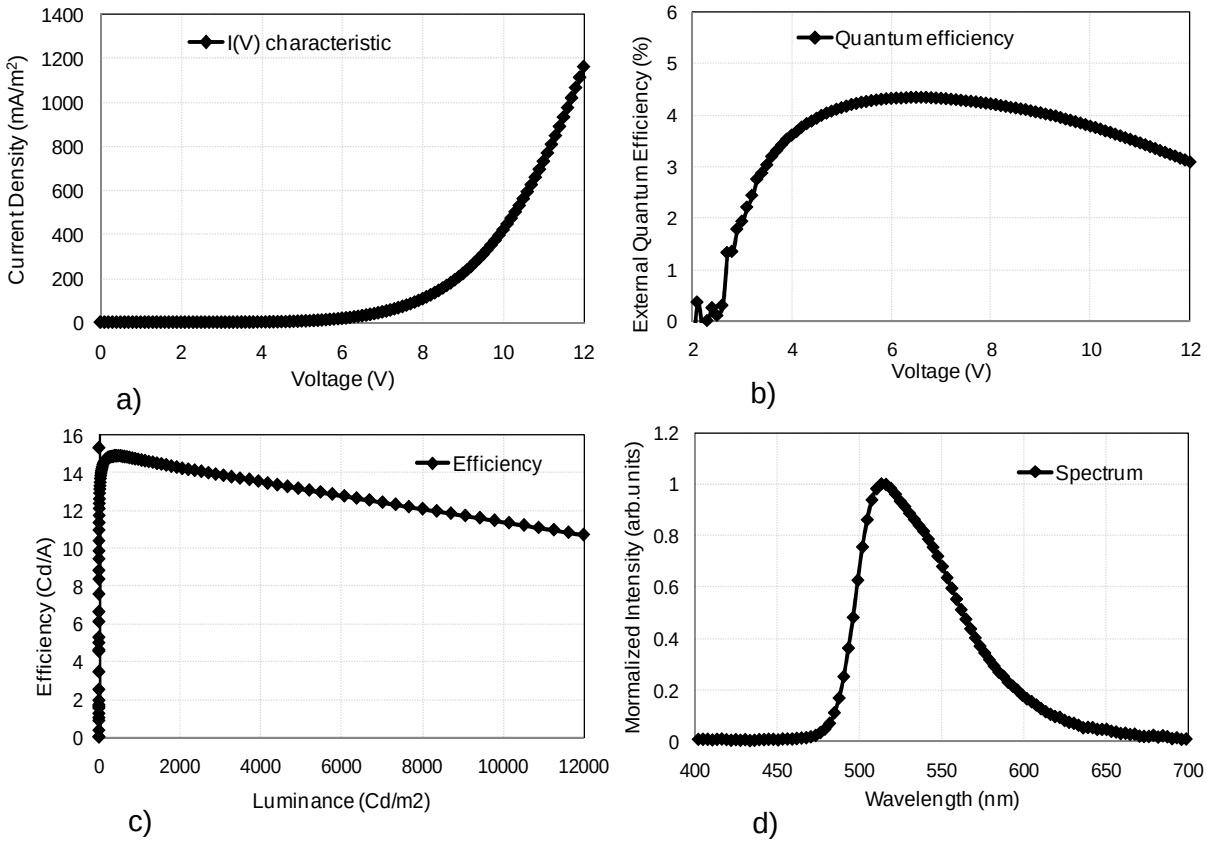

Figure III.7: PLED printed in ambient atmosphere and based on an iridium complex as emitter. (a) I-V characteristic. (b) Spectrum. (c) Efficiency versus luminance. (d) External quantum efficiency.

Performance of such printed PLED remain inferior to the ones obtained by spin coating with characteristics such as turn-on voltage of 6 V (4 V), efficiency of 14 Cd/A (25 Cd/A) and external quantum efficiency of 4.5% (6%) for printed and in bracket spin coated devices, respectively.
This is related to the layer quality of the printed devices which suffer from low homogeneity and to the absence of mechanical driving force (centripetal force) which is important for a good molecule organization and film smoothness in the case of spin coated devices. As a matter of fact, the performance of printed devices is mainly affected by the drying process. To print an active layer, a large number of small droplets (diameter of 50 µm) are deposited close to one another. Then they merge and form a liquid layer finally forming a continuous film. During the drying period, molecules migrate within the film due to capillary flow induced by the differential evaporation rates across the drop: liquid evaporating from the edge is replenished by liquid from the interior. The resulting liquid profile can carry nearly all the dispersed material to the edge. This is called the “coffee ring effect”. The motion of the

molecules is, of course, not controllable and accumulation toward the edge could be different from one molecule to another, according to its ability to move inside the liquid film. Since the PLED is based on 4 different materials that migrate in different way, the finished dry layer might contain locally different mixtures compared to the originally prepared solution.

A special evaporation holder was designed (Figure III.8), which allows a precise mechanical alignment of the shadow mask with respect to the opto-chip. The 5 nm barium layer capped with a 70 nm aluminum layer was evaporated through this shadow mask. As seen in Figure III.10, the width of the PLEDs is defined by the width of the ITO strips, which is 3 mm. The length L_{OLED}, on the other hand, is determined by the width of the cathode. A set of different shadow masks for cathode evaporation was fabricated with cathode widths ranging from 200 µm to 2 mm. As an example, the device shown in Figure III.9 has a cathode width of 2 mm.

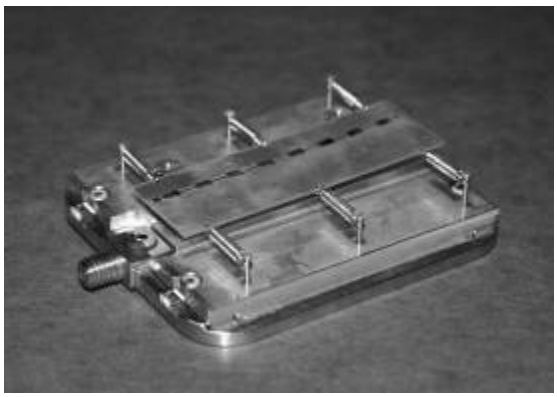

Figure III.8: Evaporation holder with shadow mask that can be aligned by mechanical means.

Figure III.9 shows a finished device integrated onto the opto-chip. The EL polymer film is shown as a yellow-greenish stripe on the left hand side of the sample. The metallic cathodes of the 8 pixels are clearly visible. The cathodes of the four bottom and the four top pixels are connected by a thin metal line.

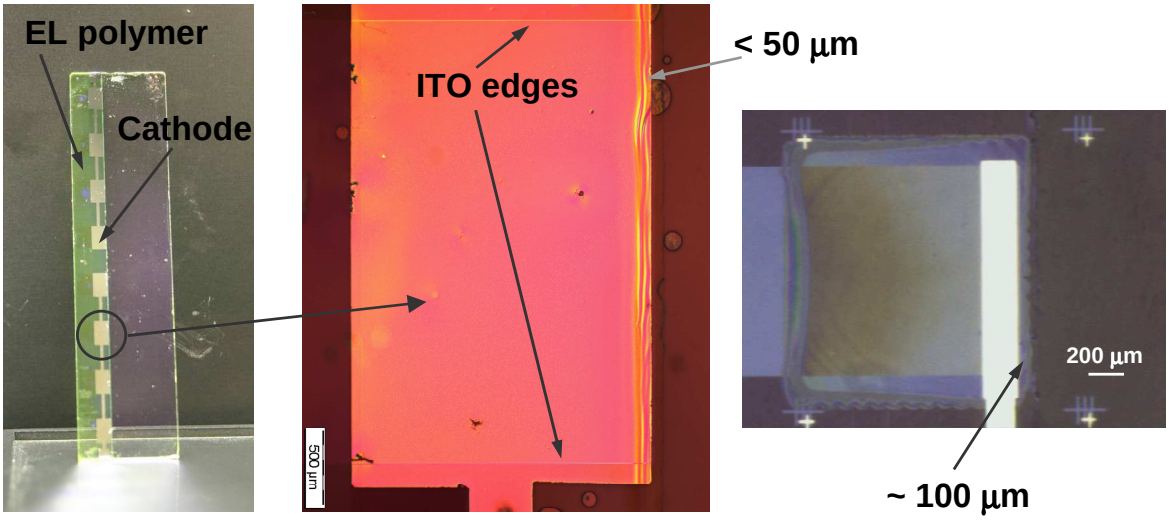

Figure III.9: Left: Photograph of a finished device with a spin coated EL layer. Center: Micrograph of one of the pixels of the device shown in on the left. The cathode shows as an orange-red area (differential interference contrast mode DIC). The edges of the ITO anode appear as thin horizontal lines at the very top and at the bottom of the image. Right: Micrograph of an ink-jet printed device.

The right border of the PLED (Figure III.9) is the important part from where most of the light is coupled into the waveguide. To reduce waveguide losses induced by absorptive media on top of the waveguide, it is of importance that the PLED layers extend as little as possible beyond the edge of the light-emitting part of the PLED, which is defined by the overlap of anode (i.e. the ITO) and cathode. As seen in the middle and right panel of Figure III.9, the polymer layers extend beyond the ITO edge by less than 100 µm.
Note that in order to guarantee an electrically operational device, the active layers between anode and cathode must separate the two electrodes, and thus a polymer coverage beyond the ITO edge is unavoidable. Even of greater importance than the polymer alignment is the cathode layer registration. The cathode consists of metallic layers, which constitute loss channels for the waveguide modes. The mechanical alignment system of the mask holder ensures a precision for the alignment of cathode and anode edges if better than 50 µm, as seen in Figure III.9.
Figure III.10 show the cross section view and the required alignment needed for the integration of the PLED onto the single-mode waveguide.

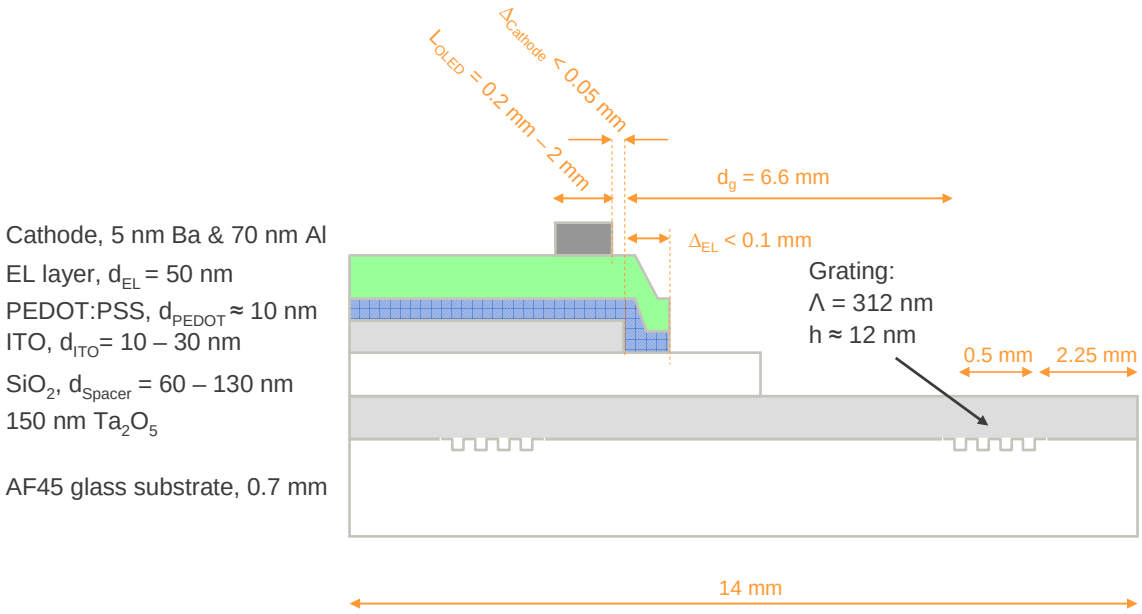

Figure III.10: Cross-section of the integrated PLED device architecture.

After cathode deposition, the devices need to be stored and operated under inert atmosphere. In our case, this is a nitrogen glove-box system, where electrical and optical characterization of the devices can be performed. However, if the devices are to be operated under ambient conditions – e.g. for further characterization or, later on, for clinical tests – they need to be protected from the influence of oxygen and water. This is normally done by encapsulation. As a simple encapsulation technique we used a 100 µm cover glass, which was glued onto the chip with a two-component epoxy. Care had to be taken not to apply any epoxy onto the waveguide since epoxy can induce waveguide losses and thus dampen the guided light significantly. Therefore, the epoxy is only applied to the edges of the chip, outside the area of the grating couplers.
The emission spectrum of an $Ir(mppy)_3$-based green PLED is shown in Figure III.7 d. The peak wavelength is close to 510 nm. PLEDs are broadband emitters, and in the particular case of the $Ir(mppy)_3$ the full-width-at-half-maximum (FWHM) bandwidth is about 70 nm. $Ir(mppy)_3$ PLEDs were optimized in our laboratory prior to integrating them onto the opto-chip. For the optimization work, standard test substrates and procedures for PLED characterization were utilized. The spin coated optimized $Ir(mppy)_3$ PLEDs exhibit the following characteristics: they turn on (1 µW/cm^2) at a voltage of about 4 V. When driven with 10 V, they emit a total optical power (integrated over spectral range and solid angle of

emission) of 3 mW/cm^2 while consuming 20 mA/cm^2. The external quantum efficiency (photons out per electron in) of the PLEDs reaches 6 %. An emission power of more than 20 mW/cm^2 can be achieved when driving the PLEDs at voltages around 15 V.
A red emitting PLED based on poly[{9,9-dihexyl-2,7-bis(1-cyanovinylene)fluorenylene}-alt-co-{2,5-bis(N,N'-diphenylamino)-1,4,phenylene}] has been also used. The disadvantage of the available red emitters is their considerably lower external quantum efficiencies of ≤ 1% around 630 nm and ≤ 0.5% around 680 nm. Moreover, their lifetime is inferior to the one of the green emitting PLEDs. For this reason, the integration of PLEDs onto the SEMOFS sensor chip focused on green-emitting materials, in particular the Ir(mppy)$_3$-based blend described in detail in the previously.

3. State-of-the-art polymer photodiode

Polymer photosensors, fabricated in the metal-polymer-metal configuration, show high photosensitivities of 0.1 - 0.5 A/Watt in the visible; which is comparable to those of inorganic semiconductors. PPDs exhibit low dark currents and a large dynamic range. They can be hybridized with other optical / electronic devices to form integrated systems with added functionality.
In this work, polymer bulk heterojunction photodiodes based on poly(3-hexylthiophene) (P3HT) as donor and [6,6]-phenyl-C61 butyric acid methyl ester (PCBM) as acceptor were investigated (Figure II.2). The performance of the photodiode was maximized in terms of quantum efficiency, on/off ratio and device stability / lifetime, by systematically optimizing cathode, anode, solvent, blending ratio, device thickness and annealing conditions. A simple model, taking into account the optical interference in the thin-film device, was also developed, and it reproduces the thickness-dependence of the quantum efficiency very well.
An optimized photodiode is obtained with a 240 nm thick 1:1 blend (by weight) of PCBM:P3HT spin coated from 1,2dichlorobenzene sandwiched between a transparent indium tin oxide anode and a calcium / aluminum cathode.
These photodetectors show state-of-the-art external quantum efficiencies of 70% at 0 V, on/off current ratios larger than 10^5 at -1 V, dark current densities below 20 nA/cm^2 at -1 V, and an adequate lifetime of several weeks without any encapsulation.

a. Experimental details

i. Materials

We use regioregular head-to-tail P3HT (Figure III.11 a) as hole conductor. Regioregularity denotes the percentage of sterio-regular head-to-tail (HT) attachments of the alkyl side chains to the three-position of the thiophene rings. The HT regio-specific polymers have improved conductivities [132], mobilities, optical non-linearity and magnetic properties over the regiorandom HH (head to head) polymers, due to their ability to form supramolecular self-assembled regions when in the solid state.
We used P3HT from Merck Chemicals Ltd. The HOMO, LUMO and optical gap of P3HT are estimated to be 5.2 eV, 3.5 eV and 1.92 eV, respectively (Figure III.12) [133]. P3HT shows one of the highest field-effect mobilies of all polymer semiconductors with a value of 10^{-1} cm^2/(V.s) [134,135].

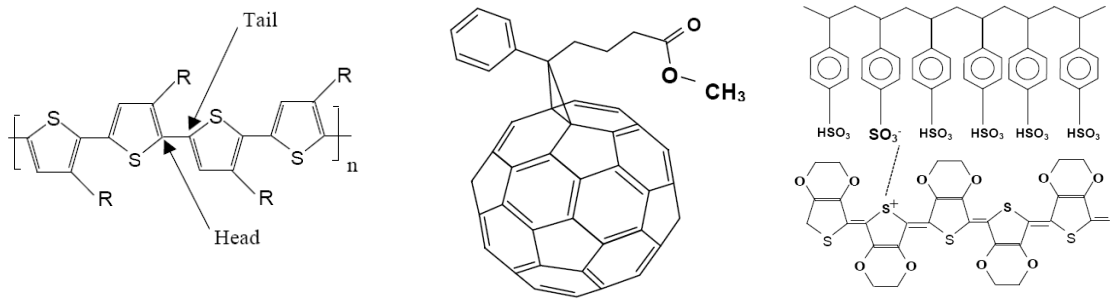

a) b) c)

Figure III.11: Molecular structure of (a) P3HT, (b) PCBM and (c) PEDOT:PSS.

C_{60} is a molecule that consists of 60 carbon atoms, arranged as 12 pentagons and 20 hexagons (buckminsterfullerene). C_{60} is an electron acceptor capable of accepting as many as six electrons. Due to its high electron affinity, it is a promising candidate as the acceptor in blends where conjugated polymers are good photoexcited electron donors. Buckminsterfullerene is a special spherical electron carbon cluster which is not really soluble in common organic solvents. PCBM, purchased from Nano-C Inc, is a C_{60} based material in which a methyl-ester group is attached (see Figure III.11 b) to improve the solubility in common organic solvents. HOMO, LUMO and gap are estimated to be 6.1 eV, 3.7 eV and 2.4 eV respectively (Figure III.12) [136].
A PCBM electron mobility of 10^{-5} $cm^2/(V.s)$ at room temperature has been reported [137]. This PCBM has a low absorption coefficient. This low absorption can be attributed to a high degree of symmetry, making the lowest-energy transitions formally dipole forbidden.

Sputtered indium oxide doped with tin oxide, ITO, has been used as transparent conductive anode. It is one of the few metal oxides that combine technologically interesting properties such as high transparency in the visible range, good electrical conductivity, good hole injection properties into organic materials and excellent substrate adherence.
Poly(3,4-ethylenedioxythiophene) doped with poly(styrenesulfonic acid) (PEDOT:PSS) is commonly used as hole injection layer between indium tin oxide anode and the emitting layer in organic light emitting diodes, where the PEDOT:PSS layer forms effectively the anode in this device architecture. PEDOT:PSS (Al 4084) has been commercialized by H. C. Starck. The formula of PEDOT:PSS is represented in Figure III.11 c. The beneficial effects of PEDOT:PSS arise from the smoothening of the ITO surface and favored hole collection in the anode.
A schematic band diagram Figure III.12, borrowed from inorganic material, illustrates different materials employed for bulk heterojunction photodiodes.

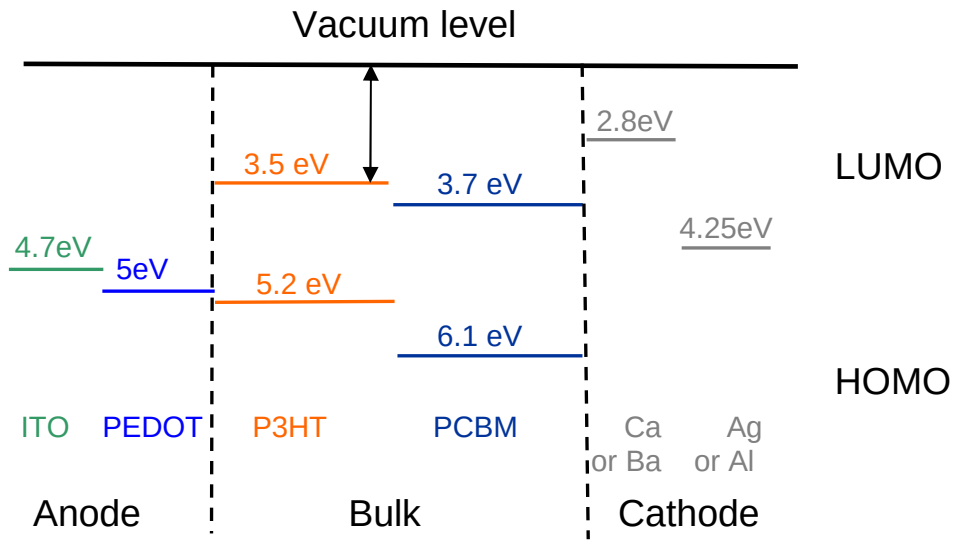

Figure III.12: Band diagram of a bulk heterojunction PD.

Note that P3HT is placed adjacent to the anode and PCBM adjacent to the cathode.

ii. Fabrication procedure

The device were fabricated and characterized in two glove-boxes under nitrogen (less than 10 ppm O_2 + 1 ppm H_2O impurities). The first glove-box is used for device fabrication. The second one contains characterization equipments. The two glove-boxes are connected by a high-vacuum load-lock system to an evaporation chamber, which is used to deposit the metallic cathodes.
The vacuum in the evaporation chamber is close to 10^{-7} Pa (Figure III.13).

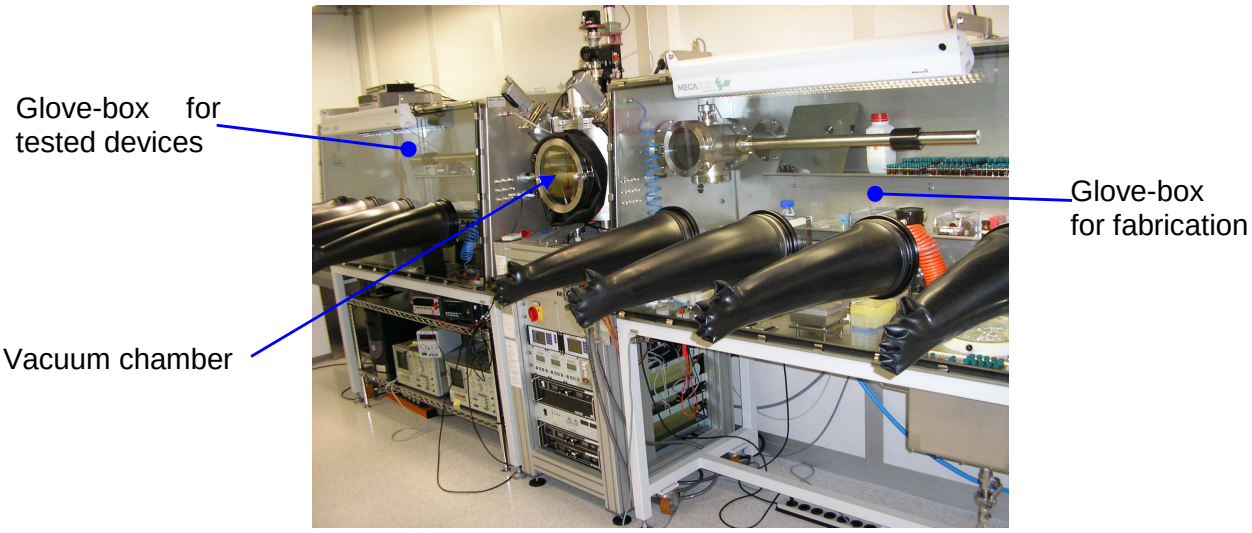

Figure III.13: The two glove-boxes and vacuum chamber with evaporation system.

We work with ITO covered glass samples of (1 inch)^2 (Figure III.14). Finished devices contain eight pixels of 2 mm x 2 mm; each one is defined by the intersection of ITO pattern and cathode aluminum strip.

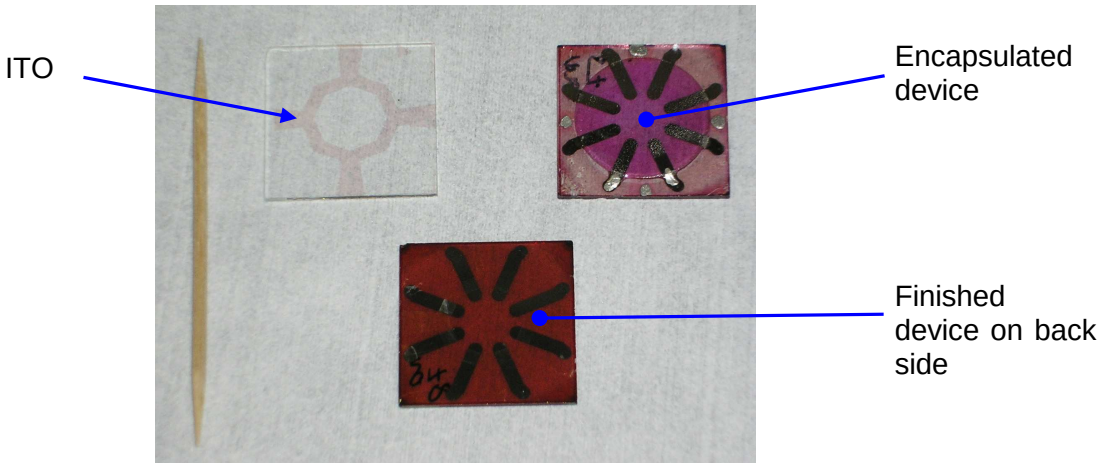

Figure III.14: ITO sample, finished and encapsulated devices.

The fabrication and test procedure is depicted in Figure III.15.

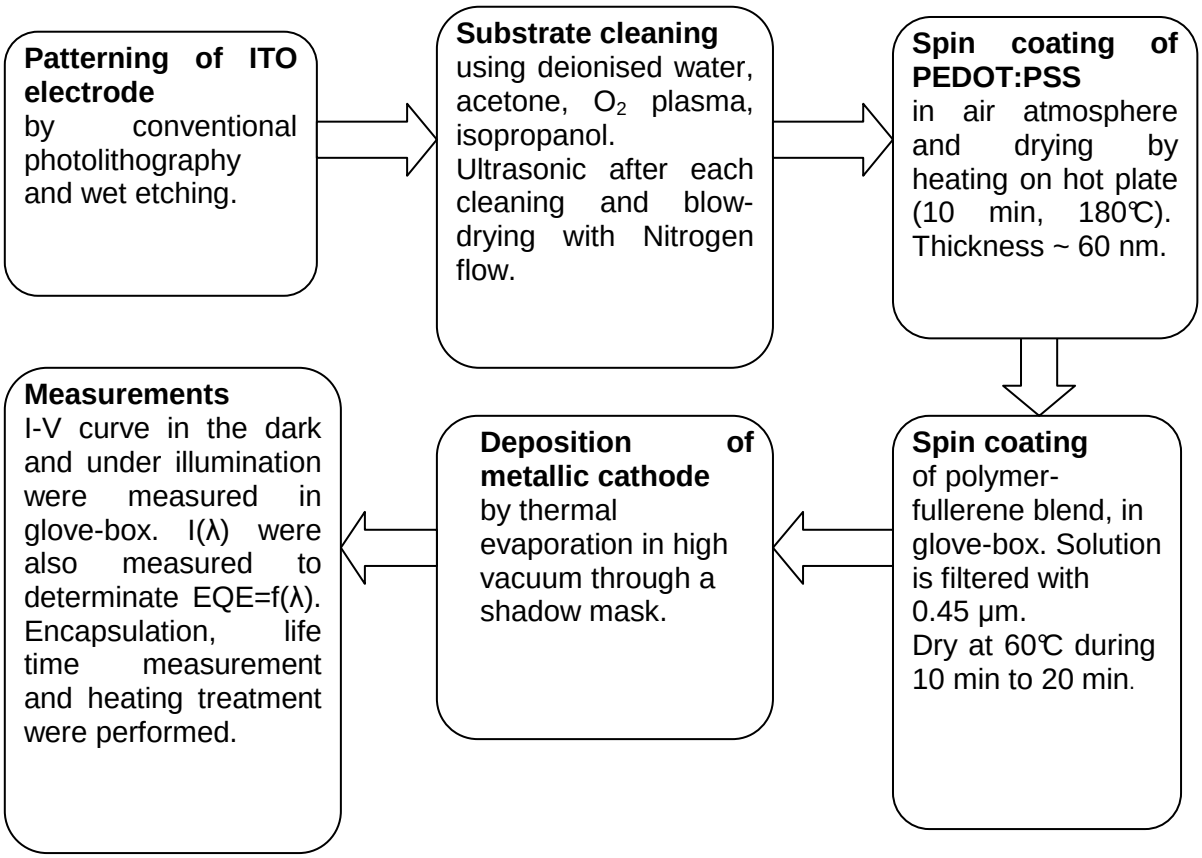

Figure III.15: Steps of fabrication.

Thus, at the end of the process, devices are put on a home-made test holder in which eight metallic rods create contact with metallic cathodes, and twelve other for ITO anode contact (Figure III.16).

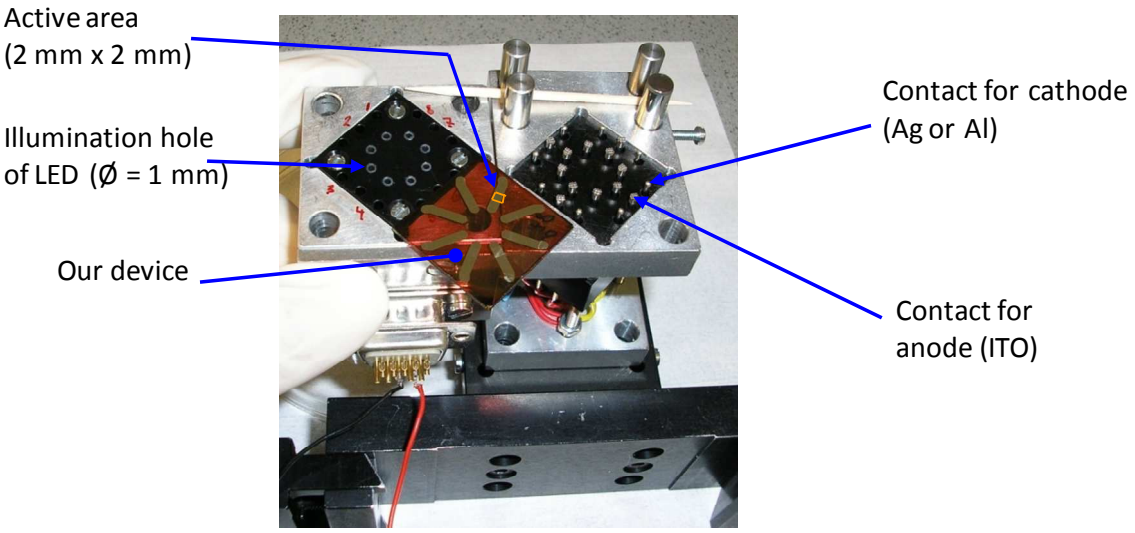

Figure III.16: Photograph of test equipment and of our device.

I-V measurements were performed using a Hewlett-Packard 4145B semiconductor parameter analyzer which was controlled by a computer using Labview software.
Eight inorganic blue light emitting diodes (LED) with peak wavelength of 465 nm were used to illuminate each PPDs. The Labview program was written such that an I-V curve was first recorded in the dark and subsequently under illumination by the blue LED at specified light intensities. The blue LEDs were calibrated with a Newport 818-SL optical power meter. For each device with its eight pixels, we considered median value, quartile 25% as minima and quartile 75% as maxima in order to make a comparison.
EQE versus wavelength was measured with an optical radiation measurement system from Optronic Laboratories, Inc. A monochromator was used to illuminate the device with monochromatic light from 300 to 1800 nm. The intensity was calibrated with a silicon detector (300 nm - 800 nm). Since the Optronics instrument is operated in air, the devices were encapsulated for the EQE-versus-wavelength measurement. The devices were encapsulated with a thin circular glass plate from the back side, as shown in Figure III.14.

b. Results and discussion

The PPDs were systematically optimized in terms of EQE, on/off ratio and stability against oxygen and water vapor. As a result, the performance of the PPDs could be significantly increased and state-of-the-art performance has been equaled or even surpassed.
In the following the individual optimization steps are discussed.

i. Cathode optimization

Choice of materials

Calcium, barium, silver and aluminum are the four different metals that were tested, with work functions 2.9 eV, 2.7 eV, 4.3 eV, 4.3 eV, respectively [133]. Ca and Ba are relevant to reduce the barrier injection and to increase the built-in electric field and V_{oc}. Al and Ag are capping layers for protection. Different combinations such as Ca/Ag, Ca/Al, Ba/Ag, Ba/Al were tested. The resulting performance figures of these combinations are quite similar. Ca generally performs slightly better than Ba, and we therefore use cathodes that are free of Ba

in the following. Ca/Ag is best in terms of EQE. Moreover, Ag is favored over Al because of its superior optical reflection properties, which would make it more suitable for microcavity applications at a later stage of this work. However, stability which is usually a weakness of organic devices, is better for PPDs with Al capping layer.

Thickness of Ca/Ag

For the choice of Ca/Ag as cathode, the thickness of Ca was first optimized. The results are very similar, as seen in Figure III.17. As a consequence, we decided to use 30 Å as thickness for Ca.

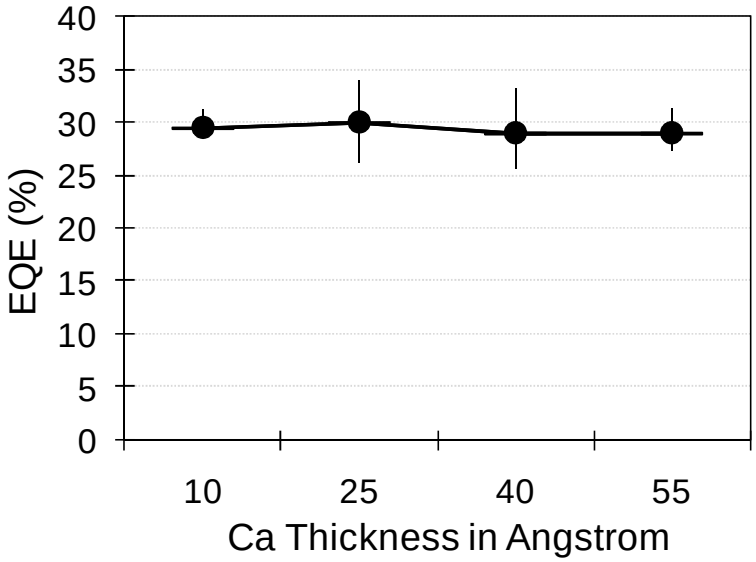

Figure III.17: Influence of Ca thickness on EQE at 465 nm and -2 V. Device structure is ITO/PEDOT:PSS/PCBM:P3HT blend ratio (4:1) (60 nm) and cathode Ca-Ag(60 nm).

Next, the influence of the thickness of the Ag on the performance of the PPD with Ca/Ag cathode was examined. Again, the influence was found to be very weak and a thickness of 500 Å for the silver was chosen.
We conclude that the influence of cathode materials tested here on EQE and on/off ratio is weak. However, as will be seen later, the choice of the cathode has a strong effect on the device stability.

ii. Blend optimization

Here we discuss the influence of the blend ratio, the thickness of the photosensitive polymer layer and the solvent on the device performance.

Ratio of P3HT:PCBM

In the literature, various blending ratios of between 1:1 and 1:5 by weight have been described. The results from the literature are not conclusive and it is not clear which blending ratio works best. (1:1) and (1:4) blending ratios are frequently cited as good ones. We tested different P3HT:PCBM ratios. The results are shown in Figure III.18.

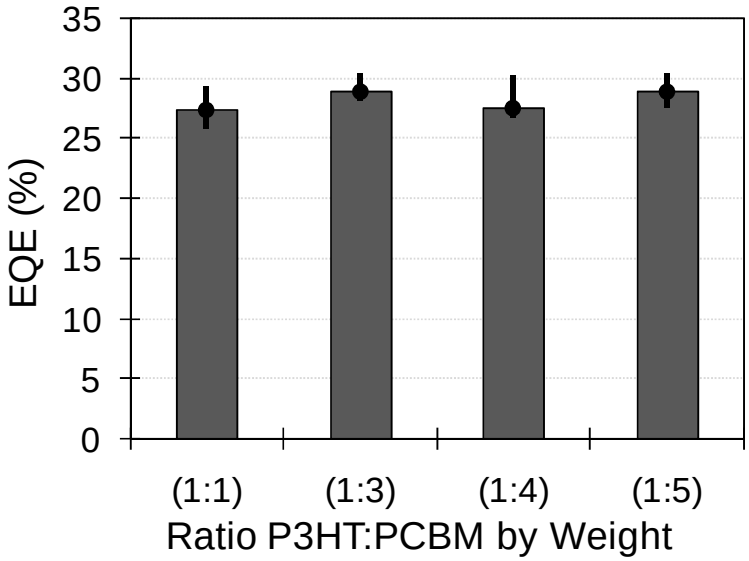

Figure III.18: EQE at 465 nm and -2 V, for different blend ratio of P3HT:PCBM. Device structure is ITO/PEDOT:PSS/PCBM:P3HT blend ratio (60 nm)/Ca-Ag(3 nm/60 nm).

It is clear from Figure III.18 that there is no strong dependence of the EQE on the blending ratio; which explains the inconclusive results described in literature.
We decided to work with a (1:1) ratio, in particular to overcome some problems linked to the weak solubility of PCBM.

Thickness of the photosensitive polymer layer parameter

This is the most important parameter for the on/off ratio. The on/off ratio grows with increasing thickness as seen in Figure III.20. The interference effects in front of the metallic cathode, which acts as an almost perfect mirror in the visible, result in periodic EQE variations with layer thickness.
We use a simple model of a transparent anode/polymer/metallic cathode (Figure III.19), to describe the interference effects observed in polymer PDs.

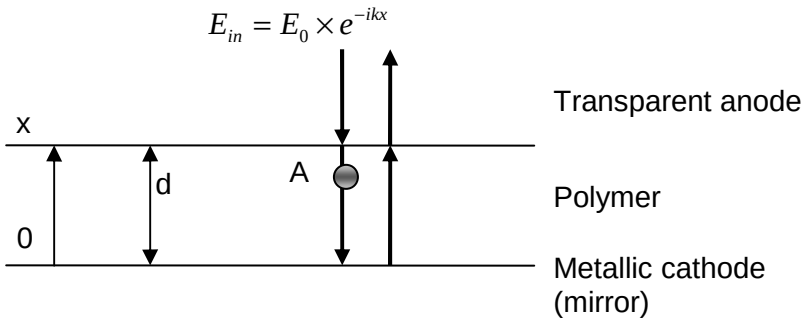

Figure III.19: Interference effect in a simple model.

We assume normal incidence and constant absorption coefficient *α*. At point *A*, at the distance *x* from the mirror, electric field amplitude of the incident electromagnetic radiation is:

$$E = E_0\left(e^{-ikx} \times e^{-\frac{\alpha}{2}(d-x)} + r \cdot e^{-ikx} \times e^{-\frac{\alpha}{2}(d-x)} \times e^{i2kx} \times e^{-\frac{\alpha}{2}\cdot 2x} \right)$$

Equation III-1 : Electric field in organic layer.

where $r = |r| \cdot e^{i\cdot\varphi_r}$ is the complex reflection coefficient of the mirror, $k = \frac{2\pi}{\lambda} n$ is the wave vector, *λ* the wavelength and *n* the refractive index of our blend.
The intensity is given by

$$I \propto |E|^2 = |E_0|^2 \cdot e^{-\alpha(d-x)}\left[1 + |r|^2 \cdot e^{-2\alpha x} + 2|r| \cdot e^{-\alpha x} \cdot \cos\left(\frac{4\pi}{\lambda} n \cdot x + \varphi_r\right)\right]$$

Equation III-2 : Electric field intensity in organic layer.

And the total absorption *A* is:

$$A \propto \int_0^d |E|^2 dx,$$

$$A \propto |E_0|^2 \cdot \left[\frac{1}{\alpha} \cdot \left(1 - e^{-\alpha d}\right) \cdot \left(1 + |r|^2 e^{-\alpha d}\right) + |r| \frac{\lambda}{2\pi \cdot n} e^{-\alpha d} \cdot \left(\sin\left(\frac{4\pi \cdot n}{\lambda} d + \varphi_r\right) - \sin\varphi_r\right)\right]$$

Equation III-3 : Absorption in organic layer.

It follows from Equation III-3 that the total absorption has an oscillating part with a period of $\frac{4\pi \cdot n}{\lambda} \cdot d = m \cdot 2\pi$. If we assume that the fraction of absorbed photons that lead to charge carriers in the external circuit is constant and independent of polymer thickness, EQE will be proportional to the absorption value. Thus, the EQE should also show oscillations with a distance between two maxima of $\Delta d = \frac{\lambda}{2n}$.
With the wavelength *λ* = 465 nm and an estimated *n* of 1.6, we thus calculate *Δd* ≈ 145 nm.
Figure III.20 shows the dependence of the EQE on polymer layer thickness for a ITO/PEDOT:PSS/Polymer/Ca-Ag device. The simple theory from Equation III-3 reproduces the experimental data quite well. For the fit shown in Figure III.20, |*r*| was fixed at 1 and *n* was set to 1.6, which left 3 free fit parameter, namely the proportionality factor E_0, *α* and φ_r. The fitted value for *α* was 9.5 x 10^4 cm^{-1}, which is in perfect agreement with the absorption coefficient of 10^5 cm^{-1} found in literature [138,139].

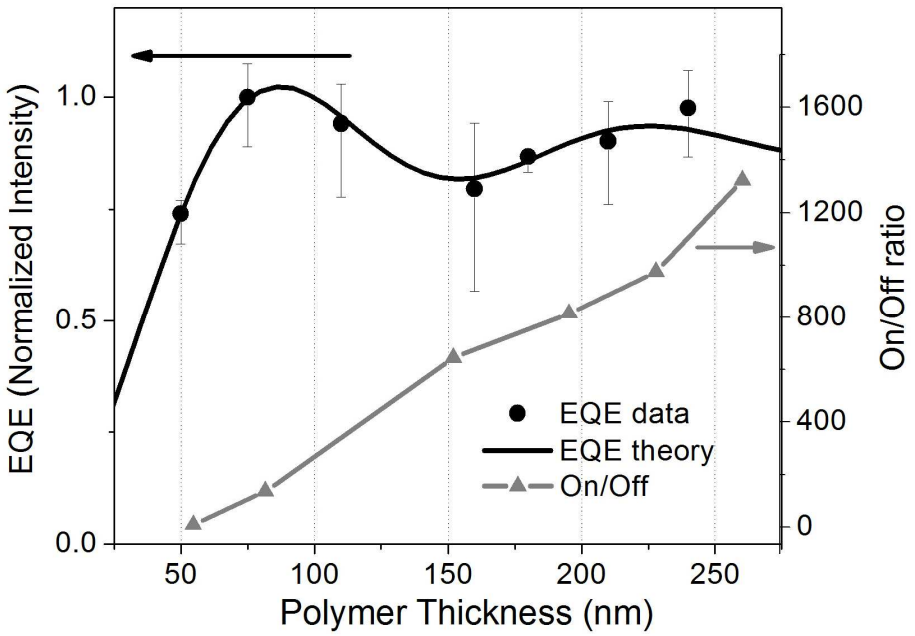

Figure III.20: EQE and on/off ratio, measured at -1 V and wavelength illumination of 468 nm, as a function of the thickness d of the active polymer layer. PPD structure: ITO(70 nm)/PEDOT(60 nm)/PCBM:P3HT (1:1)/Ca(3 nm)/Ag(50 nm).

The EQE shows an absolute maximum at a thickness of about 70 nm. However, for devices of 70 nm polymer layer thickness, the on/off ratio is rather small (Figure III.20). For this reason we decided to work with devices of 240 nm thickness, which leads to much enhanced on/off ratio and is close to the second maximum of the EQE.
We can also plot the electric field intensity (Equation III-2) versus distance from the cathode (Figure III.21), using the parameter obtained from the fit of Figure III.20.

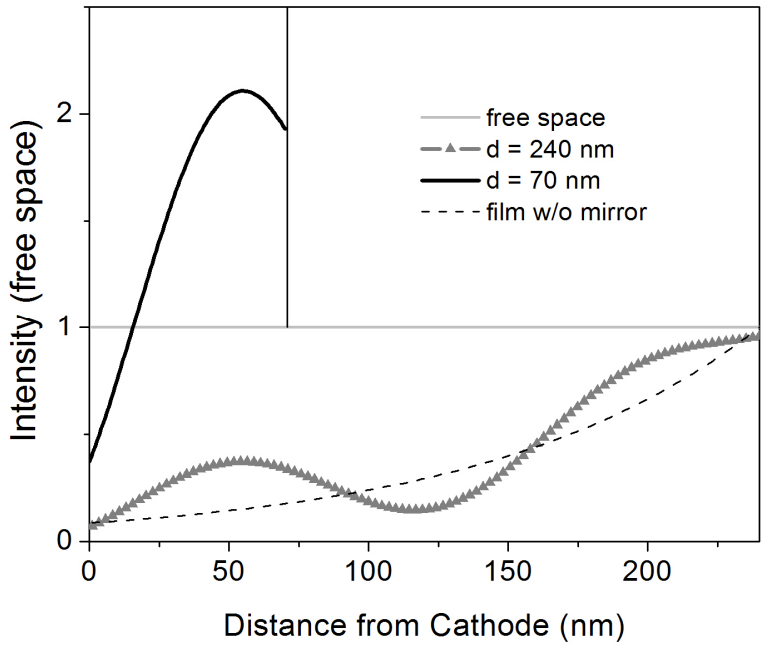

Figure III.21: Optical field intensity versus distance from cathode for thick (grey triangles markers curve) and thin (dark) devices. Also shown is the exponential decay that is expected in a free-standing polymer film without cathode.

Enhancement of the intensity in a thin device is better than in a thick one. Indeed, in a thick device, the electric field is more absorbed before reaching the cathode where it is reflected, so interference effects are low.

iii. Solvent

Solvent is relevant to increase solution concentration, and, in this way, also thickness and on/off ratio. Moreover, the solvent can influence the self-organization of the polymer film during the deposition process.
We first used chloroform, then chlorobenzene and finished by using 1,2dichlorobenzene, all purchased from Aldrich.
EQE comparison for chlorobenzene and 1,2dichlorobenzene is shown on Figure III.22.

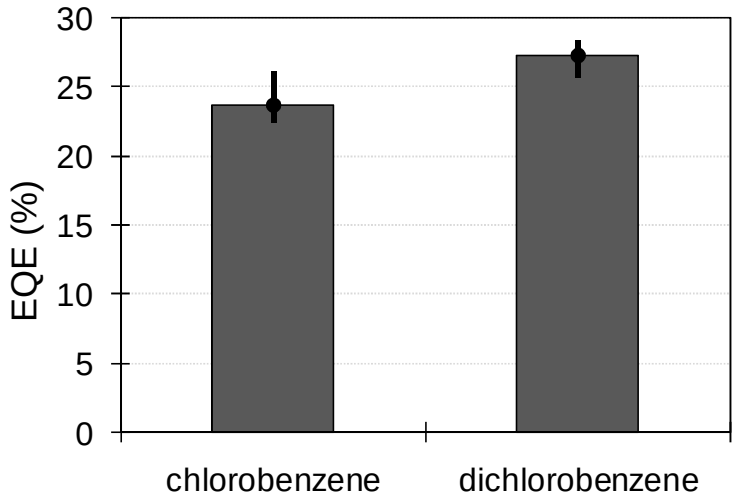

Figure III.22: Influence of the solvent on EQE at 465 nm and -2 V. Device structure is ITO/PEDOT:PSS/PCBM:P3HT (1:1) blend ratio (80 nm)/Ca-Ag(3 nm/60 nm).

Dichlorobenzene simultaneously increases the EQE and the on/off ratio. It allows the dissolution of PCBM, which is the bottleneck for high concentration solutions, at a level of 60 mg/ml which allowed us to produce thicker films than with e.g. chlorobenzene, and thus achieve better on/off ratios.
The enhancement in the EQE of the devices fabricated with dichlorobenzene solutions can be explained by an increased charge carrier mobility. These results indicate that spin coating the active layer blend from a dichlorobenzene solution has the effect of simultaneously enhancing the morphological microstructures of both components, P3HT and PCBM, which results in better interpenetrating networks.

iv. Anode optimization

We performed some experiments by replacing PEDOT:PSS or adding on PEDOT:PSS a layer of poly(N-vinylcarbazole) (PVK) or poly(N-vinylcarbazole):N,N'-diphenyl-N,N'-(3-methyphenyl)-1,1'-biphenyl-4,4'-diamine (PVK:TPD). Outcomes were not very encouraging. However, experiments without PEDOT:PSS gave very interesting results (Figure III.23 and Figure III.24).

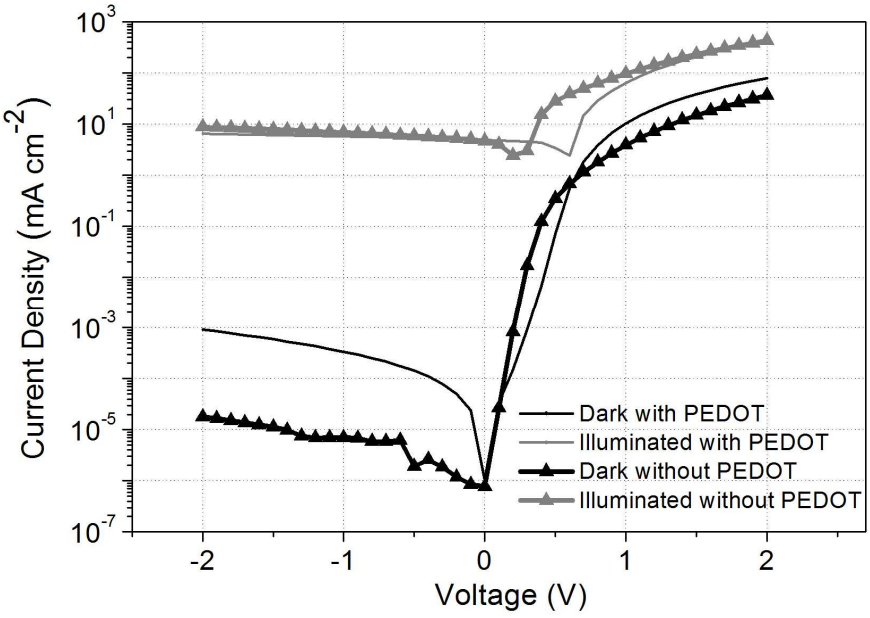

Figure III.23: I-V curve for anode with PEDOT:PSS (solid lines), and without PEDOT:PSS (triangles). Device structure is anode/PCBM:P3HT (1:1) blend ratio (240 nm)/Ca-Al(3 nm/60 nm).

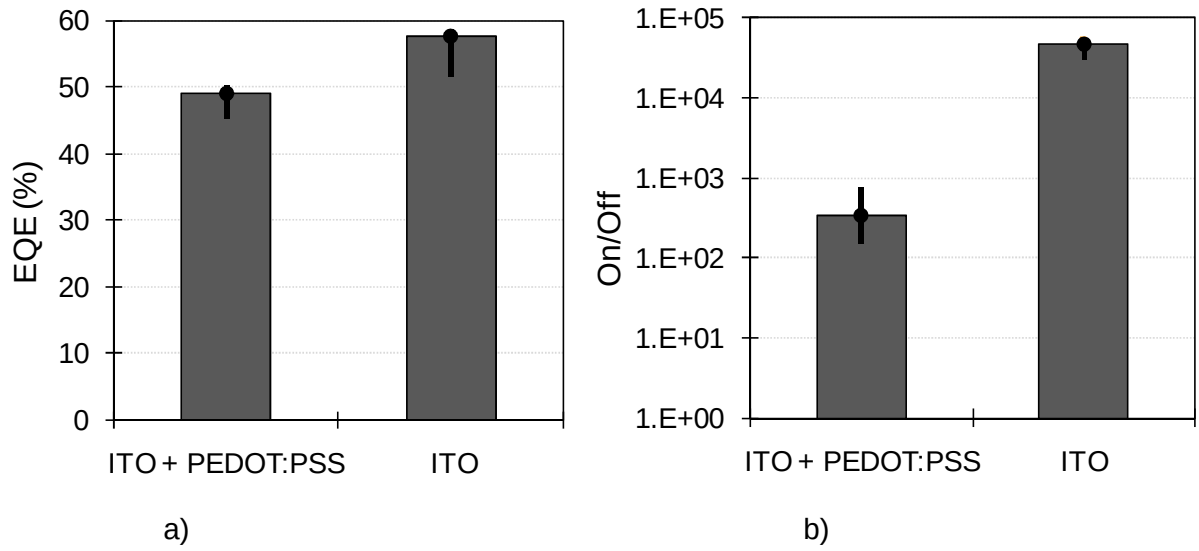

Figure III.24: (a) EQE and (b) on/off ratio for anode with PEDOT:PSS, and without PEDOT:PSS.

The plots of Figure III.23 show different V_{oc} and different behavior under forward bias. V_{oc} is related to the work function difference between anode and cathode. Thus, as seen on Figure III.12, this difference is reduced if PEDOT:PSS is not used as the anode. In the case of the I-V curve for the device without PEDOT:PSS, the variation in forward bias is explained by an increased barrier for hole injection. However, these two characteristics are not very important for PPDs.

Improvement of on/off ratio in the PEDOT:PSS free devices is possible due to the fact that the PEDOT:PSS dopes the semiconductor polymer layer with ionic impurities.

The observed behavior of the EQE can be explained with absorption losses in the PEDOT. These results are consistent with experiments by T. Aernouts *et al*. [71].

v. Various treatments

Reducing dopants

In order to reduce the number of residual dopants in the polymer blend, we conducted several experiments. First, we tried hydrazine, which is a strong reducing agent and has been show to successfully un-dope p-type polymer semiconductor materials [137]. However, the results are not encouraging. The off current is reduced, but the device is strongly degraded by the hydrazine.
Second, we used a new batch of P3HT, which improved the on/off ratio significantly. This is made possibly by a reduction of residual impurity content in the next batch.

Annealing process

Annealing has often been used in the literature to improve device characteristics. According to V. D. Mihailetchi *et al.* [140], annealing treatments mostly act on PCBM and create crystalline aggregates, which improves the percolating pathway for electrons. According to F. Padinger *et al*. [73], who increased their EQE from 20 to 60% in this way, the annealing process is relevant for the P3HT. Their interpretation is an enhanced crystallization of the polymer, leading to an increased hole conductivity of the polythiophene.
Our experiments are less striking, as seen in Figure III.25.

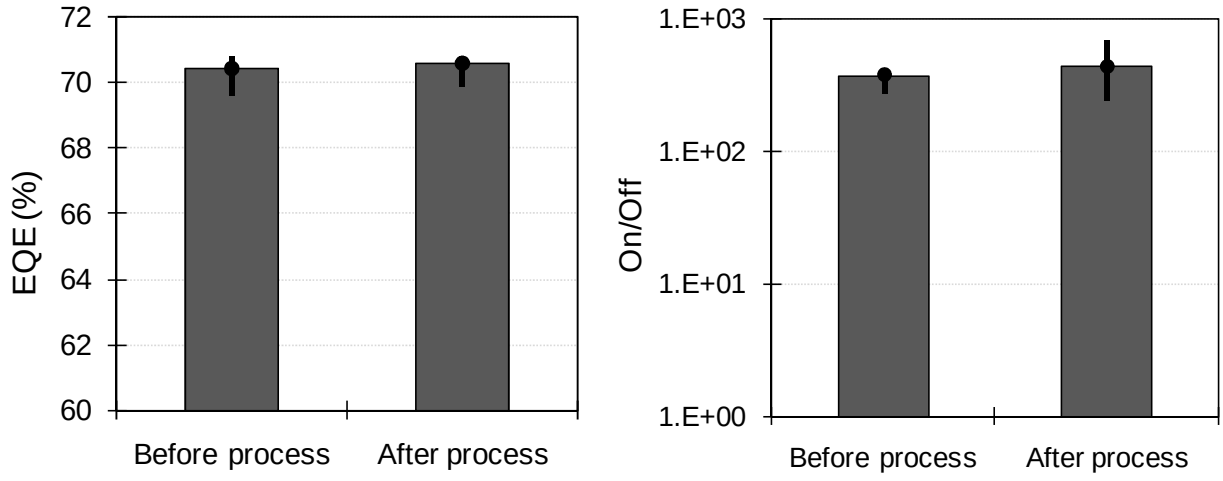

Figure III.25: Effect of the annealing process on the EQE (a) and on/off ratio (b) at 465 nm and -2 V. Device structure is ITO/PEDOT:PSS/PCBM:P3HT (1:1) blend ratio (240 nm)/Ca-Ag(3 nm/60 nm)

Upon annealing at 100℃ for 10 min, the on/off rati o slightly increased, whereas the EQE remained stable. Different times and temperatures conditions were tested; they gave similar results at the end. Note that our EQE was already very good before the annealing process. Using 1,2dichlorobenzene and spin coating the organic solution at low speed (~ 800 rpm) seems to allow for a good self organization of the blend. We conclude that annealing is not really beneficial to our devices.

vi. Response time

The response time of the PPDs was measured by illuminating the device with a pulsed blue LED (465 nm, 6 µW). The resulting current in the PPD was measured with a lock-in technique. Figure III.26 shows the response of two PPDs of different thickness.

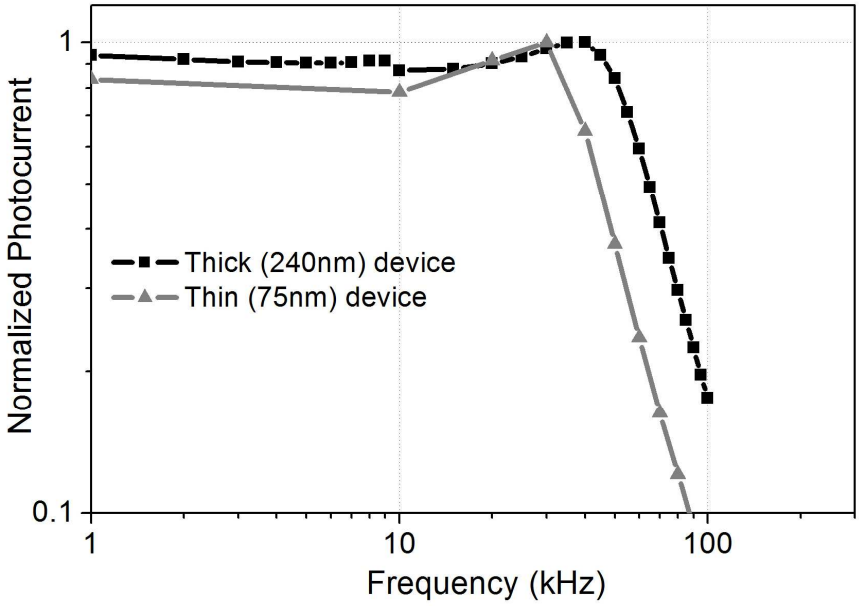

Figure III.26: Response of a thin (grey triangles) and a thick (dark squares) polymer photodiode as a function of frequency, at 465 nm and 0 V. Device structure is ITO/PEDOT:PSS/PCBM:P3HT (1:1) blend ratio/Ca-Ag(3 nm/60 nm).

As seen in Figure III.26, the response time of thin and thick devices are approximately the same. 3 dB attenuation of the response is reached at 45 kHz and 62 kHz for thin and thick devices respectively, and the response rolls off with $\frac{1}{f^2}$.

Since charge separation happens on a sub-picosecond timescale in these bulk heterojunction photodiodes, charge transport is the speed-limiting process. (Note that the device capacitance is smaller than C = 1 nF. Thus the RC time constant with serial resistance that is well below 100 Ω, cannot explain the low response time). In the simplest picture, the transit time τ – that is the time it takes a charge carrier to cross the device – is the limiting time for charge transport: $\tau \propto \frac{d^2}{\mu \times V}$ where d is the thickness, μ the mobility and V the potential.

In this formula, a constant mobility μ and a uniform electric field $E = \frac{V}{d}$ was assumed. Clearly, if the transit time was limiting the PPD response time, one would expect a strong dependence on the thickness. We obviously do not observe this behavior in our devices.
We conclude that E must show non-uniformities, which seems to be closely related to the nanoscale morphology. There are two possible locations causing low response times in thin devices, firstly at the inside of the organic layer, and secondly at the interface between cathodes. Microscopy analysis should help to elucidate the exact mechanisms. Note that the two devices were prepared with the same solution and thus only spin speeds for organic layer deposition were different.

vii. Detector Noise

To quantify the detector noise, a good figure of merit to use is the noise equivalent power (NEP). The NEP is defined as the minimum incident power required in order to generate a photocurrent equal to the noise current of the photodetector at a specified frequency (f), and within a specific bandwidth (B). The NEP for a detector is calculated by the following formula:

$$NEP = \frac{I_N}{\Re(\lambda)}$$

Equation III-4

Where I_N is the noise current in A/Hz^{½} and $\Re$ is the responsivity equal to 0.25 A/W at the wavelength of 468 nm. The NEP given in Equation III-4 is in units of Watts/Hz^{½}. Since the power to current conversion of a diode depends on the wavelength, the NEP is always quoted at a particular wavelength. For a reverse biased photodiode, the shot noise is the dominant component, and the thermal noise contribution can be neglected. The shot noise of the dark current is given by [85]:

$$\mathrm{I_s} = \sqrt{2\,\mathrm{e}\;\mathrm{i_D}\;\mathrm{B}}$$

Equation III-5

Where *e* is the unit charge (1.6 x 10^{-19} coulombs), i_D the dark leakage current and *B* the bandwidth.
With typical values of our diodes (i_D = 1.6 x 10^{-10} A and *B* = 1 Hz) a shot noise current of 7.16 × 10^{-15} amperes/Hz^{½} is obtained, which translates into a dark current NEP of 2.8 × 10^{-14} Watts/Hz^{½} for our device area *A* = 2 × 2 mm^2. For comparison with detectors of different area, we introduce the specific detectivity parameter defined by

$$D^* = \frac{\sqrt{A}}{NEP}$$

Equation III-6

Where D^* is the specific detectivity (cm·Hz^{½}/Watts^{-1}) and *A* the surface area (0.04 cm^2).
A high D^* indicates the ability to detect lower levels of radiant power. This factor produces a figure of merit which is area independent. We obtain a specific detectivity of 7 × 10^{12} cm·Hz^{½}/Watts for our organic photodiode, which is comparable to conventional inorganic silicon photodiodes like, for instance, a Hamamatsu S2551 with a specific detectivity of 1.5 × 10^{13} cm·Hz^{½}/Watts.

viii. Lifetime

Influence of the cathode

Lifetime is a critical parameter for organic devices. In our classic PPDs – that incorporate PEDOT-PSS layer – EQE is stable over time but the on/off ratio decreases quickly and stabilizes after 20 hours (Figure III.27). Even in nitrogen atmosphere, the on/off ratio diminishes quickly.

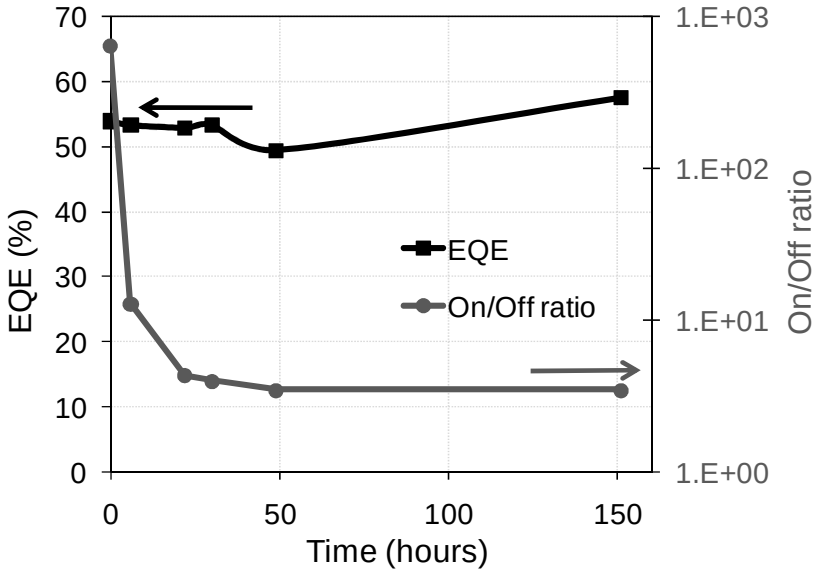

Figure III.27: Stability in air atmosphere of EQE and on/off ratio measured at 465 nm and -2 V. Device structure is ITO/PEDOT:PSS/PCBM:P3HT (1:1) blend ratio (140 nm)/Ca-Ag (3 nm/60 nm).

Experiments made with Ca/Al cathode (Figure III.28), are more promising. For the Al capped devices we observe much improved on/off ratio. On/off ratio and EQE stay constant in air atmosphere.

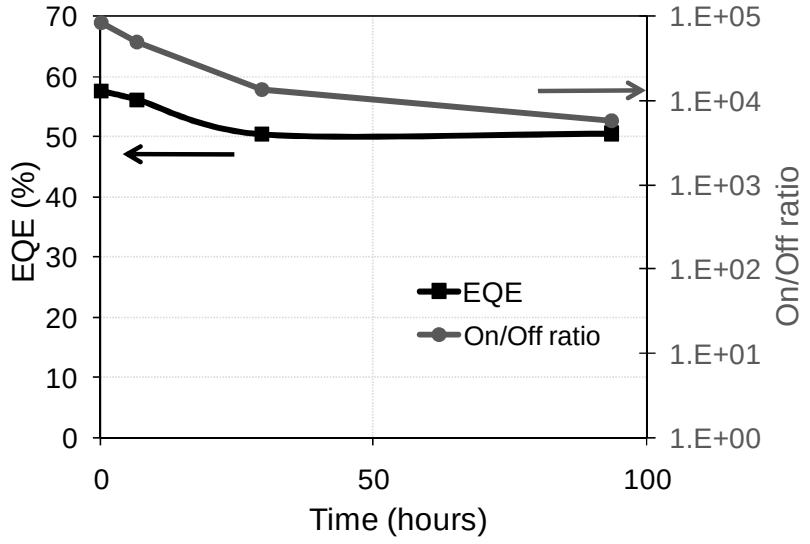

Figure III.28: Stability in air atmosphere of EQE and on/off ratio measured at 465 nm and -2 V. Device structure is ITO/PCBM:P3HT (1:1) blend ratio (240 nm)/Ca-Al(3 nm/60 nm).

It seems that Al protects the organic active area. The EQE is stabilized and the on/off ratio stays large and decreases only slowly. This kind of cathode is very promising. In combination with encapsulation, we expect the PDs with Ca/Al cathode to show satisfactory lifetime.

Influence of the anode

As previously described, a main advantage of the PEDOT:PSS-free devices is their reduced dark current. However, an equally important aspect of omitting the PEDOT:PSS layer is our finding that the operational lifetime of the photodiodes is considerably increased in devices without a PEDOT:PSS layer. On Figure III.29 the normalized photocurrent, measured at -1 V, of a PEDOT:PSS-free diode is plotted as a function of operating hours. The photocurrent is stable for more than 1500 hours. After approximately 1800 hours the photocurrent starts to increase gradually. (This rise of the photocurrent is currently not understood and is subject of further investigations). The on/off ratio decreases monotonically but is larger than 10^3 over the entire measuring period of 3000 hours (4 months). When comparing this with the inset of Figure III.29, which shows similar operational lifetime measurements performed on a photodiode with a PEDOT:PSS layer, it is evident that omitting the PEDOT:PSS is largely beneficial to the device's operational lifetime.

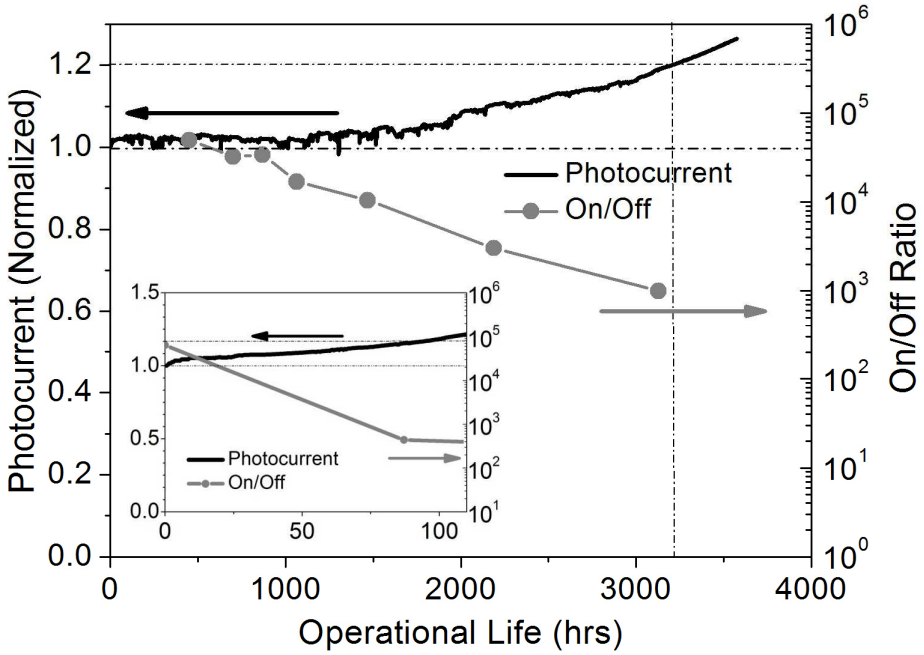

Figure III.29: Stability of the PDs without PEDOT:PSS layer. The normalized photocurrent, measured at -1 V and wavelength illumination of 468 nm, is plotted as a function of operating time at room temperature in N_2 atmosphere. The on/off ratio of the device is also displayed (right axis). PPD structure: ITO(70 nm)/PCBM:P3HT (1:1, 240 nm)/Ca(3 nm)/Al(60 nm). Inset: Equivalent stability measurement for a device with PEDOT:PSS layer. PD structure for the device shown in the inset: ITO (70 nm)/PEDOT:PSS (60 nm)/PCBM:P3HT (1:1, 240 nm)/Ca(3 nm)/Al(60 nm).

It is clear from the above that the absence of the PEDOT:PSS layer does not reduce the quantum efficiency of the photodiodes when a negative bias voltage is applied. Moreover, in this configuration the dark current level is drastically reduced and the lifetime increased.

c. *Best results and comparison with literature*

We present and compare the PPDs develop within this thesis and the state-of-the-art.

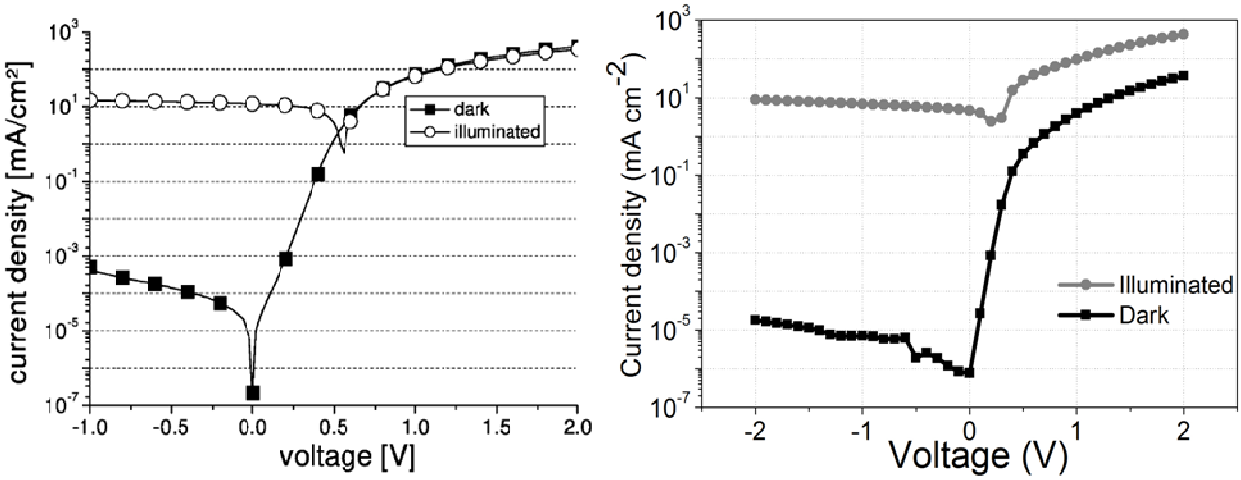

a) b)

Figure III.30: I-V characteristics of the bulk heterojunction. (a) Results from literature [P. Schilinsky et al, (2004)] [72]. (b) Results for an ITO/PCBM:P3HT (1:1) blend ratio (240 nm)/Ca-Al(3 nm/60 nm) device from our work.

Figure III.30 compares I-V characteristics of our photodiodes with literature results. It is evident from this figure that our photodiodes show improved on/off ratio of larger than 10^5 at -1 V for $P_{inc} \approx 17$ mW/cm^2 compared to about 10^4 obtained by Schilinsky *et al*. [72] for $P_{inc} = 100$ mW/cm^2.

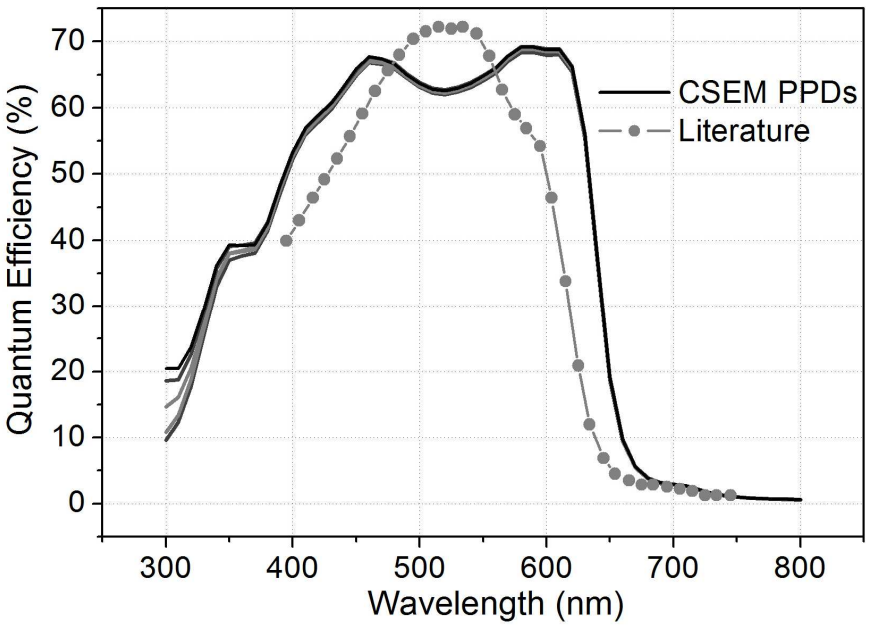

Figure III.31: EQE versus wavelength characteristics comparison of the bulk heterojunction. The light-grey line (round markers) results come from literature [P. Schilinsky et al, (2004)] [72]. The dark lines shows a ITO/PEDOT/PCBM:P3HT (1:1) blend ratio (240 nm)/Ca-Ag (3 nm/60 nm) device from our work, measured at 0 V.

Figure III.31 shows that we obtain as good external quantum efficiencies as in literature. However our devices feature a wider wavelength range. In addition, we have also obtained a good reproducibility for each device.
In conclusion, we developed a polymer bulk heterojunction photodetector based on P3HT:PCBM, which equals or surpasses state-of-the-art performance. Quantum efficiency higher than 70%, corresponding to state-of-the-art in literature, was achieved. Importantly, we were able to improve the on/off ratio to larger than 10^5 at -2 V by reducing the dark current close to 10 nA/cm^2. Our on/off ratio represents the current record for bulk heterojunction polymer photodiodes. Moreover, the stability of the PPDs could be dramatically improved by choosing an ITO-only anode and Ca/Al cathode.

d. Ink-jet printed PPD

In order to deposit the PPDs onto the biochip, we also developed a deposition process based on ink-jet printing.

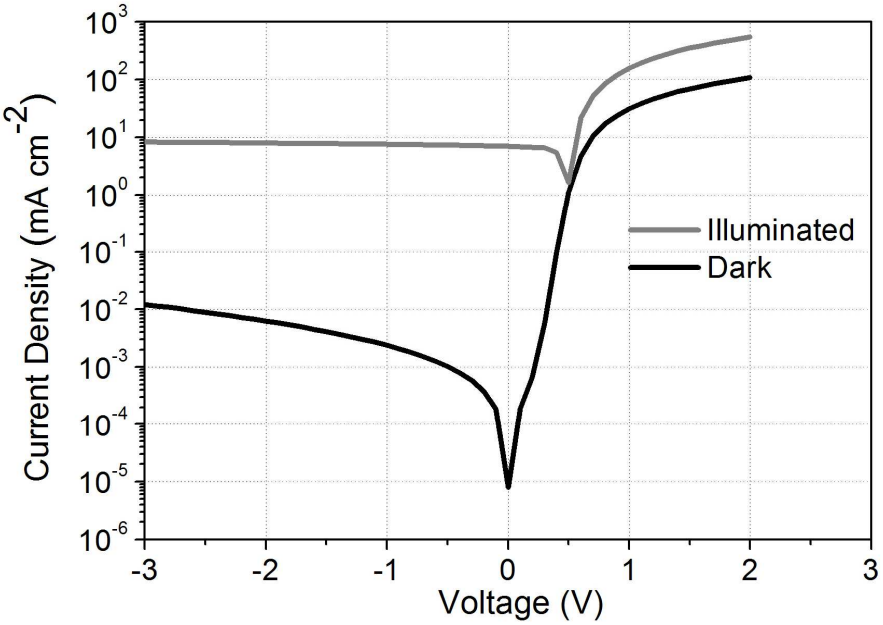

Figure III.32: I-V characteristic of printed PPD. The device is based on P3HT:PCBM (1:1) at 10 mg/ml in chlorobenzene with thickness of 60 nm.

As seen in Figure III.32, the dark current is much higher in the case of printed PPDs compared to spin coated ones. This can mainly be explained by the difference in thickness (60 nm for printed and 240 nm for spin coated) and the fact that the ink-jet printer is used in air atmosphere. The EQE is also slightly reduced in case of printed PPDs due to different layer formation for the two processes. As already explained, the spin coating technique with low spin speed and high boiling point allows self organization of the polymer layer and thus to enhance the conductivity and the EQE. In the case of the ink-jet printing, the layer formation process is totally different. There is no driving force to align the polymer; droplets are just deposited close to each other in order to form a liquid layer which then becomes a solid layer after drying. The process also implies the well known “coffee ring effect” as seen in Figure III.33.

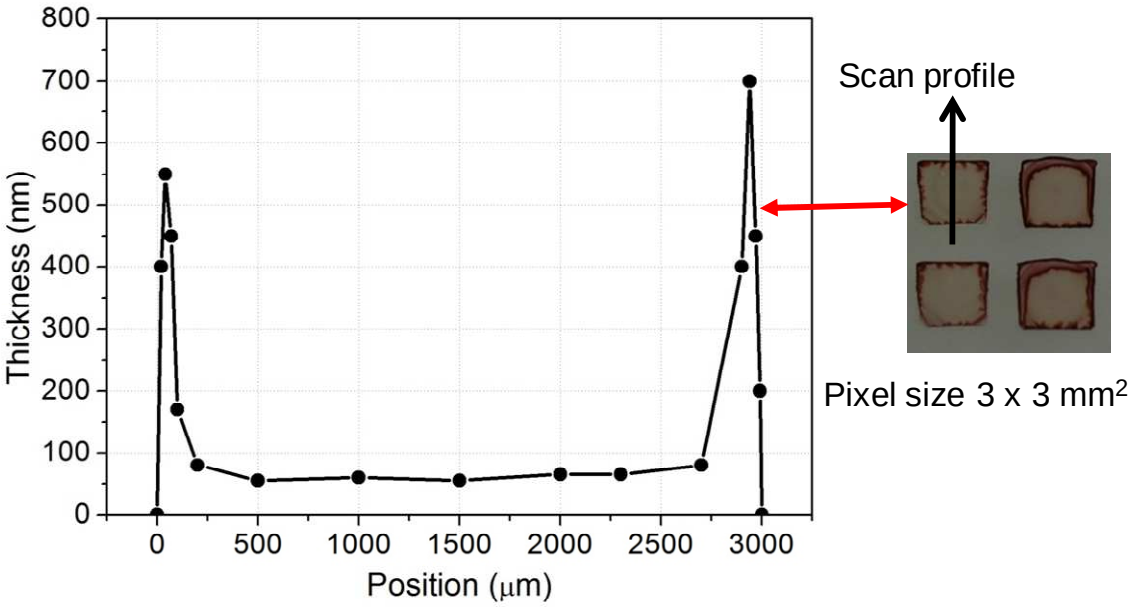

Figure III.33: Thickness profile and picture of printed P3HT:PCBM PPDs.

In spite of the thick layer at the edge of the device, the inner part is homogeneous with a thickness of 60 nm. In order to obtain reproducible results with the printed PPDs, we need to print larger layers and only work with the inner homogeneous part. The small thickness of the layer (60 nm) is also typical for printed layers. It is difficult – in one pass of a printing process – to obtain the thick layers needed for good PPDs. As a matter of fact, it is quite impossible to print concentrated solutions (more than 20 mg/ml) due to clogging of the printing head.

e. Summary on the PPD optimization and deposition

Polymer based photodiodes are interesting because their fabrication process can be less expensive and less complicated compared to their inorganic counterparts. Processing from solution and at temperatures below 100℃ allows them to be deposited on large-area, possibly inexpensive flexible substrates, and they can be integrated monolithically with other organic optoelectronic devices.
We have optimized the P3HT:PCBM bulk heterojunction diode in terms of its photodiode (rather than photovoltaic cell) performance. We have shown that while increasing the thickness of the active layer from 70 nm to 240 nm does not significantly alter the photodiode's quantum efficiency, it results in a 10-fold decrease of the dark current. By omitting the PEDOT:PSS layer the dark current has been reduced by factor of ~ 100. Furthermore device lifetimes were considerably increased by omitting the PEDOT:PSS layer, too. Conversely, a negative voltage has to be applied to maintain the EQE high. Overall, solution-processed organic photodiodes with state-of-the-art EQE of between 60 and 70% over a wide range of the visible part of the spectrum, dark current densities below 10 nA/cm^2 at -1 V, specific detectivities of 7 × 10^{12} cm·Hz^{½}/Watts, and lifetimes above 3000 hours have been demonstrated.

4. Photoluminescent material

For the indirect coupling techniques (PLED to PL material), the choice of the PL material has to meet various requirements – e.g. – match the desired spectroscopic wavelength region, offering a good match of PL absorption and PLED emission, match PL emission and PPD

wavelength sensitivity, high photoluminescent quantum yield (PLQY), large Stokes shift in order to avoid re-absorption, and good lifetime. The plasmon stack is designed to show peak absorption around 600 nm. Thus, PL emission in the 550 - 650 nm range is required. Poly[2-methoxy-5-(2'-ethyl-hexyloxy)-1,4-phenylene vinylene] (MEH-PPV) have been chosen due to its PL emission peak at ~ 600 nm (Figure III.34), large Stokes shift, PL absorption peak at 500 nm which corresponds to the emission of the best solution process PLED.

a. MEH-PPV as PL material

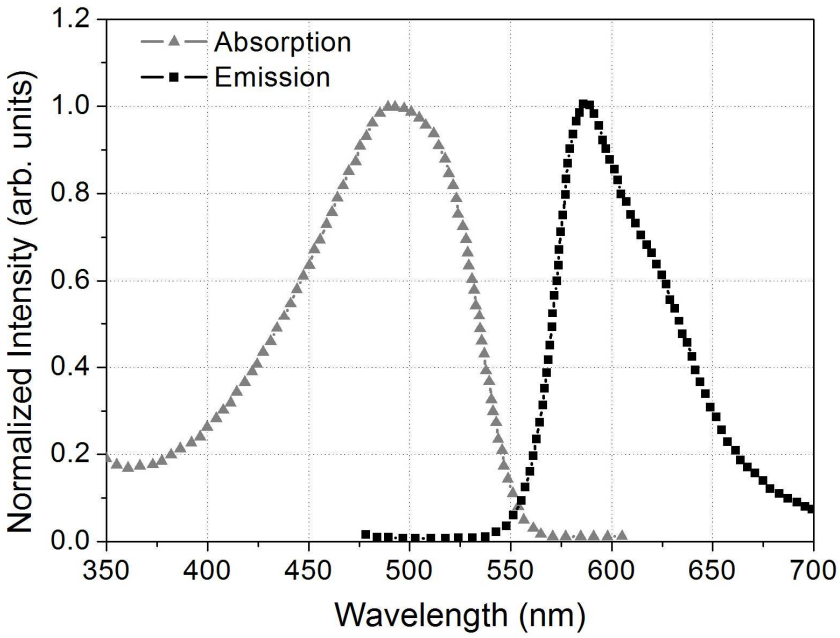

Figure III.34: Datasheet from American Dye Source [141] of the absorption (grey triangles) and emission (dark squares) spectra of MEH-PPV used as the PL material.

The PL emission coupled into the Ta_2O_5 waveguide measured in our lab showed a peak at 620 nm (Figure III.35). For this measurement the light from the out-coupling grating was input into an integrating sphere. A spectrometer from Oceanoptics [142] equipped with optical zoom was used to measure the light at the exit hole of the integrating sphere. The difference in spectrum between Figure III.34 and Figure III.35 can be attributed to different measurement conditions (the spectra depicted in Figure III.34 and Figure III.35 are measured in solution and on film, respectively) and to the influence of passive optical elements such as the out-coupling grating and the waveguide.

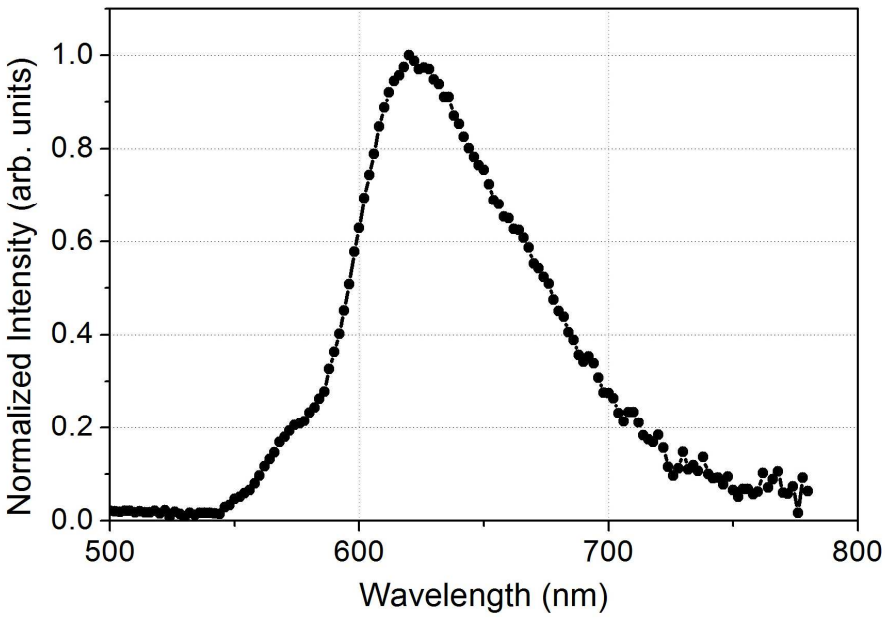

Figure III.35: Spectrum of the guided light measured at the out-coupling grating stage with MEH-PPV as PL material.

All the spectra involved in our biosensor are depicted in Figure III.36.

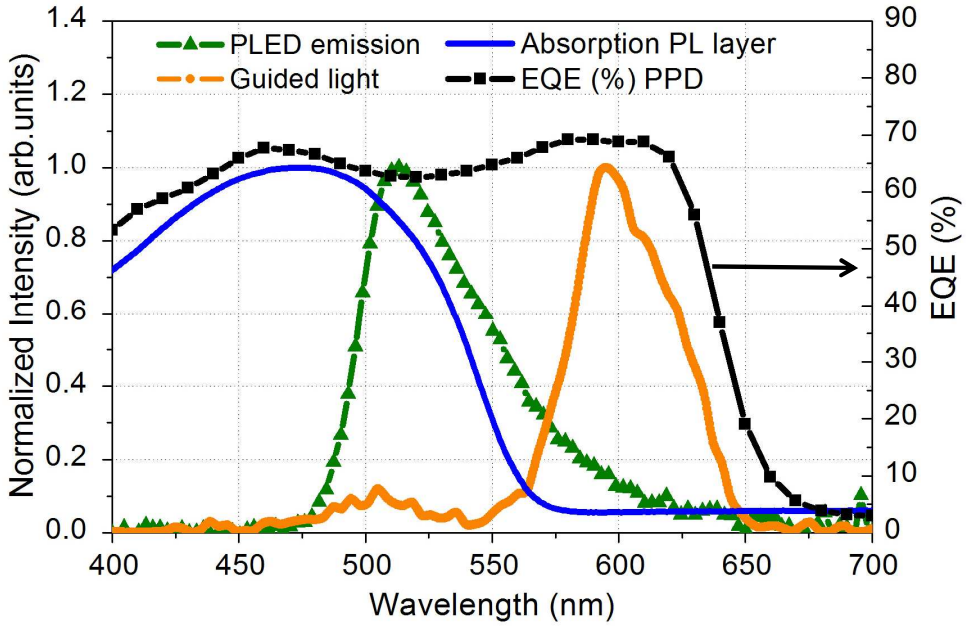

Figure III.36: Spectrum of the EL emission of the PLED (green triangles markers). Spectrum of the coupled / guided light (orange rounds). Spectrum of the response of the PPD (dark squares). Measurement of the absorption spectrum (blue curve) of the PL layer.

We can see that the PLED emission (green triangle markers) does not perfectly match the absorption (blue curve) of the PL material (MEH-PPV). However, the efficiency of this green PLED is the best we could obtain and compensates the small miss-match in spectrum. The guided light – which corresponds to the PL emission spectrum (orange round markers) – presents again a different spectrum compared to Figure III.34 and Figure III.35. In this case, a large core (2 mm) fiber was located on top of the out-coupling grating and was fed into a

spectrometer. Since the red and infra-red light are diffracted and coupled out at grating angles higher than 35° (Figure III.2), they do not couple into the fiber due to the fiber's limited numerical aperture. This case is similar to the one of the PPD array spectrometer presented in the next chapter, where large angles are simply not detected – due to interface reflection and to the fact that too large angles do not fall on the detection array anymore.

b. PL Lifetime

Lifetime studies of the PL material were carried out (Figure III.37). A 200 nm thick layer of MEH-PPV was deposited on the opto-chip. The MEH-PPV layer was pumped by an inorganic LED at constant illumination. An inorganic photodetector, from Hamamatsu [143], detected the optical power at the out-coupling stage. The lifetime in ambient atmosphere decreases significantly due to photo-oxidation. In order to work outside of the glove boxes, the PL material was encapsulated by a glass slide sealed with epoxy glue. The encapsulated PL material showed stable lifetime in ambient atmosphere with a variation of 10% during 1 hour. Within the first minute, the power decreased by 10% and then remained stable with variations below 5%. The initial decay can be attributed to a "burn-in effect" and does not represent a real drawback for our experiments.

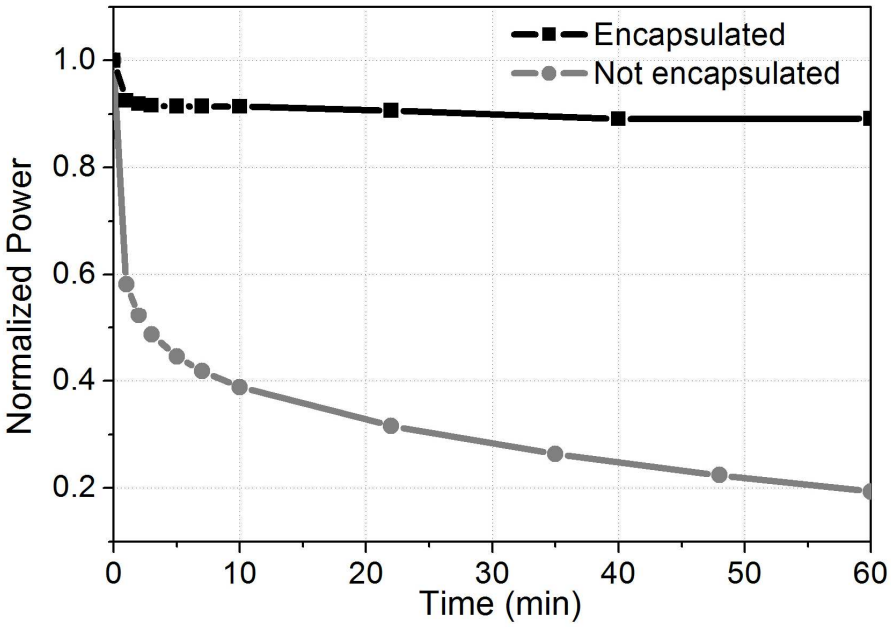

Figure III.37: Normalized PL emission power of MEH-PPV in different environmental atmospheres.

5. Conclusions on the fabrication of organic components

Optimization and deposition processes for the different optoelectronics components represent an important part of this thesis. Ink-jet printed PLEDs and PPDs have been successfully deposited. Homogeneous and respectable electro-optical performances were obtained. Moreover, optimizated PPDs [144] reach and even surpass the state-of-the-art.
Finally and as detailed in the next part, an iridium based green PLED was used to pump a MEH-PPV PL material. The PL emission light was coupled into a single-mode waveguide. Guided light interacted – at the plasmon stack in the case of the SPR test – with the analyte located inside the fluidic channel and was detected by the integrated mini-spectrometer based on P3HT:PCBM polymer photodiodes array (Figure III.38).

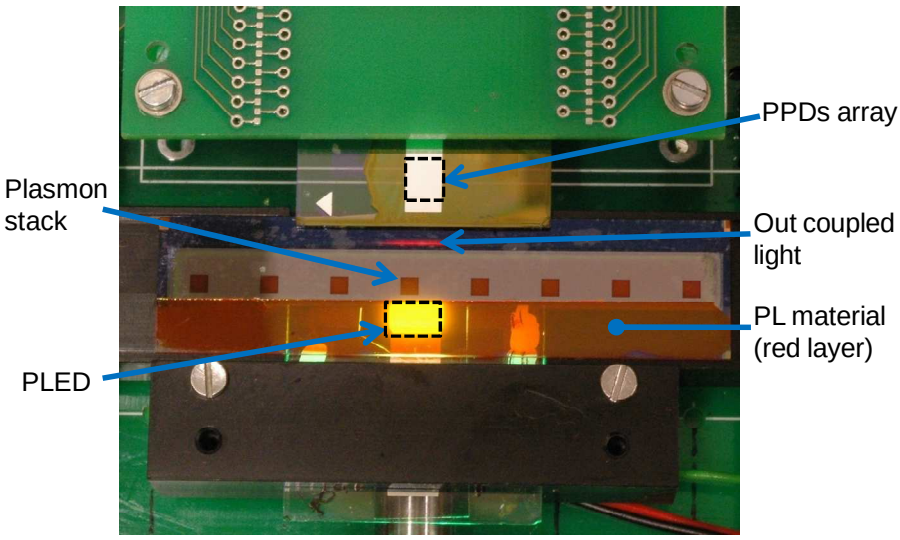

Figure III.38: picture of the biochip with organic optical components.

If higher optical power is required in the waveguide, it would be possible to replace the PLED by a high-intensity inorganic LED.

IV. In and out-coupling light into single-mode waveguide: toward biosensor applications

Polymer optoelectronics has the possibility to be deposit by additive print processes in dedicated patterns and areas forming the desired integrated components and systems.
After the optimization of the different components in terms of efficiency and deposition techniques shown in part III, this section present the integration of active and passive organic components onto an opto-chip forming a hybrid photonic system, representing an intermediate step toward the development of a fully integrated disposable biosensor.
As light source and detection components, organic light emitting diodes and organic photodiodes array have been chosen. Such components allow for a room temperature post-process deposition, especially by printing the active components onto the opto-chip. The working principle of the opto-chip is depicted in Figure I.4. Light, either from a PLED or a PL material is coupled into a single-mode planar waveguide. Within the SEMOFS project, it was foreseen that the guided light interacts with biological species located inside a fluidic channel. The detection scheme is based on SPR, which alters the guided light intensity in a wavelength-dependent way, which is monitored by the integrated organic spectrometer.
This chapter summarizes the in-coupling of light – generated by organic material – into the single-mode waveguide, the out-coupling of light and its detection by an integrated organic spectrometer. Finally, a few biomedical sensing applications of the developed integrated platform will be presented.

1. Coupling light into single-mode waveguide

Two techniques have been used to couple a Lambertian light emitter into the single-mode waveguide. Both are integrated. In a first approach, the PLED is deposited right on top of the waveguide – called direct coupling technique. In a second method, a PL material – deposited onto the waveguide and pumped by a PLED located on the backside of the substrate – is used as an indirect coupling technique.

a. Direct coupling from PLED to single-mode waveguide

According to the theoretical model and simulations detailed in part II, evanescent coupling is used to couple light from a PLED into a planar single-mode waveguide. The PLED is monolithically integrated on top of the waveguide in a stacked configuration. Due to the waveguide's proximity, the emission zone of the PLED and the waveguide modes overlap substantially, so that the PLED can directly excite the modes. The addition of a spacer layer between PLED and waveguide was shown to improve the coupling efficiency by about a factor of 5.

i. Solutions for coupling PLEDs to waveguide

Coupling light from OLED to waveguides has already been described. Ohmori *et al.* [22] coupled the light into a 70 µm thick waveguide by using a 45° cut mirror. Since the optical power that can be coupled scales with the numerical aperture (NA) and the core size of the waveguide, this approach yields insufficient power in the case of low-order mode waveguides Lin and coworker [145] coupled the light into a 100 µm thick planar waveguide. They used SiO_2 diffuser particles achieving a coupling efficiency of the order of 1%. However, diffuser particles, which are of micrometer dimensions, are not compatible with low-order mode waveguides of thicknesses comparable to the wavelength of the light they guide. In both cited cases, the waveguides were several micrometers thick and thus multimode, which is

less relevant for biosensor applications due to reduced interaction between the waveguide modes and the analyte. Punke *et al.* [23] managed to couple light from an optically pumped organic laser into PMMA-based single-mode waveguides. Recently, Gather *et al.* [146] incorporated the OLED into a low order modes waveguide.
An OLED (PLED in our case) is a Lambertian, incoherent, thin-film light source. Channeling light from this "large-area" emitter into a waveguide of typically a few 100 nm thickness is a challenging task. Using standard approaches such as focusing the light source onto an end face of the waveguide yields poor coupling efficiencies in the case of PLEDs due to the fact that it is impossible to focus the light of the "large-area" PLED to a satisfactory degree. This is the reason why an evanescent coupling scheme has been chosen, where the PLED is brought into close vicinity of the waveguide (Figure IV.1).

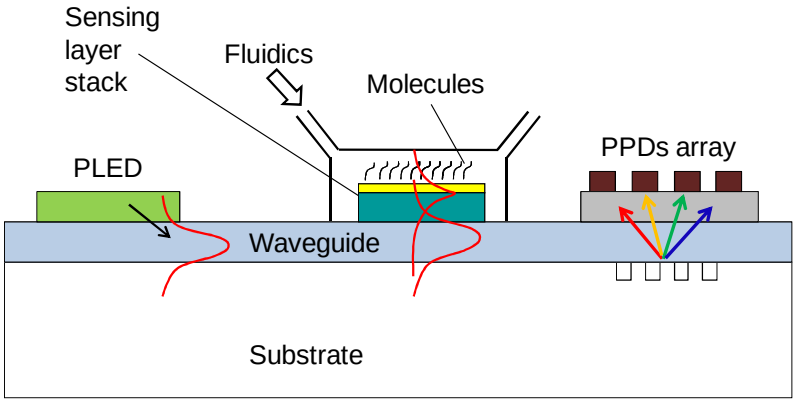

Figure IV.1: Working principle of direct PLED to waveguide coupling.

ii. Achievement for PLED to waveguide coupling

The evanescent coupling allows integration of the light source onto the opto-chip. This lab-on-a-chip has been first tested with a green PLED as emitter. The emission spectrum of an $Ir(mppy)_3$-based green PLED is shown in Figure IV.3. The peak wavelength is close to 510 nm. PLEDs are broadband emitters and in the particular case of the $Ir(mppy)_3$ the FWHM bandwidth is about 70 nm. The $Ir(mppy)_3$ PLEDs characteristics have been detailed in the previous chapter.
Figure IV.2 shows photographs of an operating chip with monolithically integrated PLEDs. The top left picture gives an overall impression. The bright green emission of the PLED can be clearly seen as well as a stripe of greenish light at the out-coupling grating. This stripe is due to light coupled from the PLED into the waveguide, where it is guided toward the out-coupling grating from which it is then being coupled out into free space. Importantly, the light stripe is also observed when substrate modes are completely suppressed by affixing absorptive black tape to the bottom-side of the substrates and its edges, indicating that the observed stripe is not due to substrate modes.

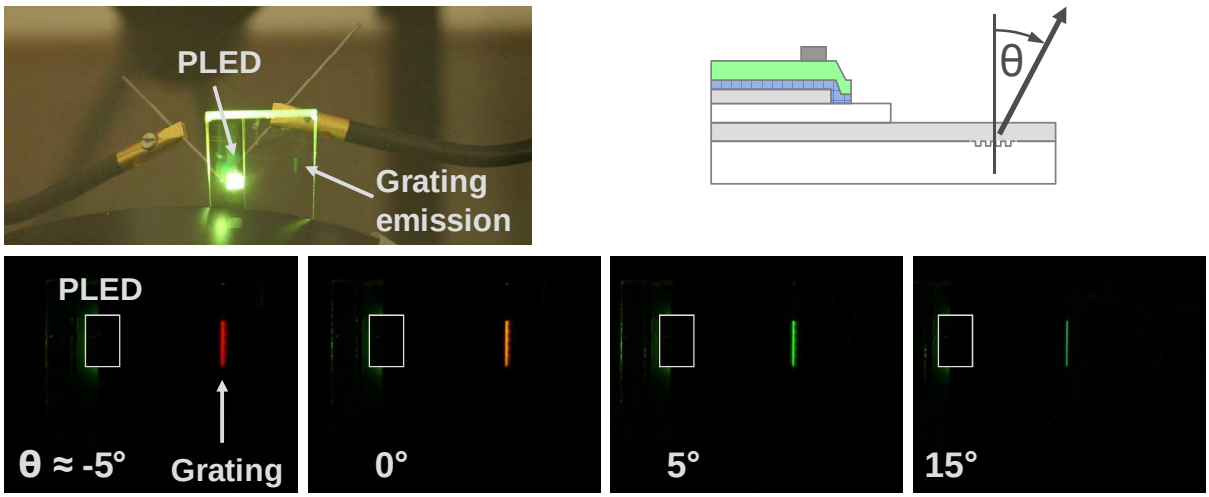

Figure IV.2: Opto-chip under operation. Top left: PLED contacted with probe needles as observed from the substrate-side of the sample. The PLED emission through the substrates is seen as a bright green spot close to the image centre. In the right part of the chip – indicated by a grey arrow – guided light is coupled out of the waveguide by the grating. Bottom: Photographs of the out-coupled light taken under different angles relative to the surface normal. The configuration is displayed in the top right.

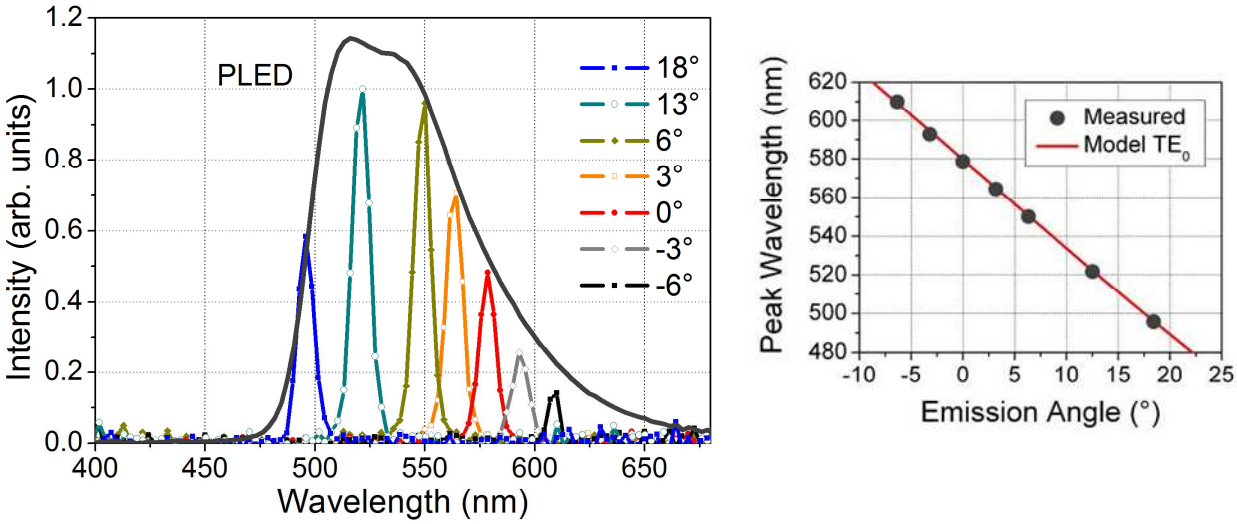

Figure IV.3. (a) Spectra of the out-coupled guided light taken under different out-coupling angles alpha. The spectrum of the PLED is also shown (dark full line). (b) Relationship between peak wavelength and out-coupling angle. The dots show the experimentally measured data and the full line the theoretical prediction from Equation IV-1 for the TE_0 mode using the parameters Λ = 312 nm, $n_{Substrate}$ = 1.5, d_{WG} = 150 nm and n_{WG} = 2.2.

As seen from the photographs in the bottom row of Figure IV.2, the color of the out-coupled light shifts from red for small negative out-coupling angles θ to green-bluish within a narrow range of angles of about 20°. Negative values of θ indicate that the in-plane wave vector changes sign when the light is diffracted by the grating – see diagram in the top right of Figure IV.2. Direct light from the PLED is thus screened by the cathode and only some stray light is visible around the PLED. For clarity, the PLED is highlighted by a grey rectangle. The fact that this color-shift occurs over such a narrow angular range rules out substrate modes

as being the origin of the out-coupled light. Substrate modes have a large distribution of in-plane wave vectors and thus would give rise to a much less distinct angular dependence.
Angle-dependent spectra of the out-coupled light are displayed in Figure IV.3 a. As expected for grating-coupling, the spectra of the out-coupled light show a strong dependency on the out-coupling angle θ. The peak wavelength shifts from about 610 nm for small negative angles to below 500 nm for angles close to 20°. On Figure IV.3 b the out-coupling angle is plotted against the measured peak-wavelength. The theoretical relationship between these two quantities is given by the grating equation:

$$\sin\theta = N_{eff} - \frac{\lambda}{\Lambda}$$

Equation IV-1

where N is the effective refractive index of the waveguide, λ the wavelength and Λ the period of the out-coupling grating. Using a mode-solver to calculate the effective refractive index N of the waveguide, and inserting this into Equation IV-1, the angle-wavelength relationship could be calculated for the mode TE_0 (The parameters used for the calculation are the following: $n_{Substrate}$ = 1.5, d_{WG} = 150 nm and n_{WG} = 2.2). The agreement between data and calculation is excellent (Figure IV.3 b), leaving no doubt that we are indeed observing light guided in the waveguide.
The spectra of the out-coupled light shows a FWHM of about 10 nm, which corresponds to the resolution of the experimental set-up (fiber + spectrometer). The envelope of the spectra measured under different emission angles approximately follows the PLED emission spectrum and covers a spectral range from below 500 nm to above 600 nm.
The efficiency of the light-coupling from PLED to single-mode waveguide will now be addressed. In order to experimentally determine the coupling efficiency, the optical power of the light coupled out of the waveguide by the grating as well as the external optical power of the PLED were measured. The former experimental quantity allows for an estimation of the total optical power coupled into the waveguide, whereas the total optical power produced by the PLED can be estimated from the latter.
The total external optical power of the PLEDs and the power of the out-coupled light have been measured by placing a large-area (11 x 11 mm^2) silicon photodetector (Newport detector 818-ST with optical meter 1835-C) underneath the PLED pixel and the out-coupling grating, respectively. (Distance from bottom of substrate to photodetector surface ≈ 2.5 mm.) In the latter case, absorptive black tape was carefully affixed to the bottom side and the edges of the chip in order to suppress substrate modes and to screen stray light. Only a 4 mm x 2 mm rectangle underneath the grating was left open, such that the photodetector captured the light coupled out by L_g = 4 mm length of the grating.
Figure IV.4 shows the result of such power measurements for a chip with integrated PLED of the following specifications: L_{PLED} = 200 µm, d_{Spacer} = 50 nm, d_{ITO} = 12 nm. The dark curves depicts the measured external optical power of the PLED, $P_{\mathrm{PLED}}^{\mathrm{meas}}$, as a function of the bias voltage applied to the PLED. $P_{\mathrm{Grating}}^{\mathrm{meas}}$, the power of the light coupled out by 4 mm of the grating in the direction of the substrate, is shown as grey curves. In solid lines, a 120 nm thick spacer layer of SiO_2 has been used between the PLED and the waveguide. The dashed lines show the case without spacer. From these curves the ratio between the out-coupled power and the PLED power can be determined, e.g. to $P_{\mathrm{Grating}}^{\mathrm{meas}} / P_{\mathrm{PLED}}^{\mathrm{meas}}$ (8V) = 8 x 10^{-4} with a 120 nm spacer layer and a ratio 5 times lower of 1.5 x 10^{-4} without spacer.
Since this ratio is somewhat dependent on bias voltage (12 % decrease between 7 V and 12 V for the example shown in Figure IV.5), the values for a bias voltage of 8 V are given.
A plausible explanation for the bias voltage dependence of the power ratio is the following: The recombination zone – in other words the region within the PLED where radiation originates – is not at a fixed distance from the anode but can move toward or away from the PLED's anode, depending on the applied bias. Since the PLED-to-waveguide coupling

efficiency depends exponentially on the distance between recombination zone and waveguide, even small voltage-dependent displacements of the recombination zone can result in changes in the coupling efficiency.

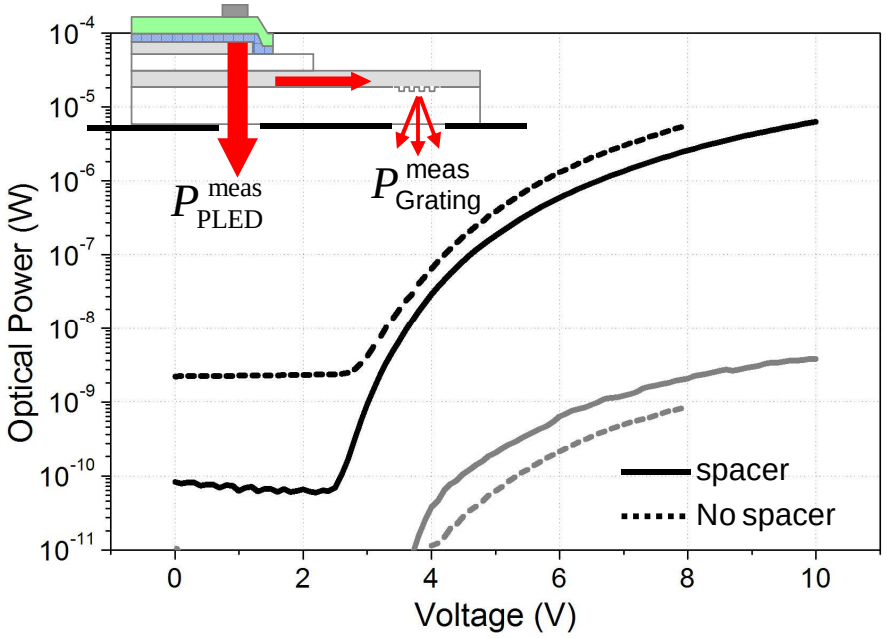

Figure IV.4: Measured optical power. Grey curve: Guided light that is coupled out by 4 mm length of the grating (toward the substrate side). Black curve: Total external PLED power. Solid curve: with 120 nm thick spacer. Dashed curve: without spacer. The inset diagram illustrates the measurement configuration.

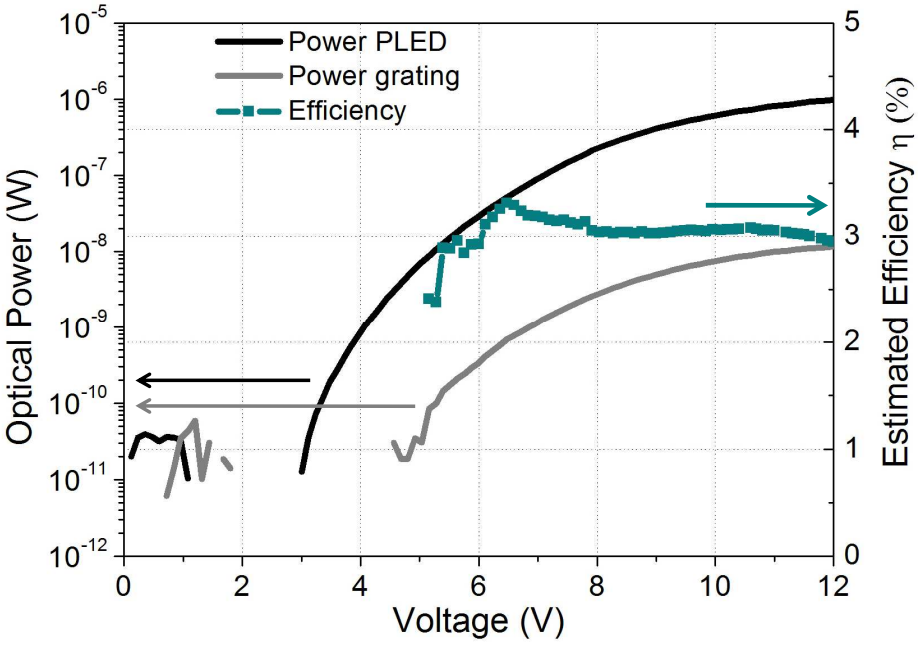

Figure IV.5: Optical power measured underneath the PLED and the grating. The corresponding coupling efficiency (with spacer) as a function of the PLED bias is also shown.

From Figure IV.5, we calculated $P_{\text{Grating}}^{\text{meas}} / P_{\text{PLED}}^{\text{meas}}$ (8V) = 1.2 x 10^{-3}. The measured power ratios for the overall SEMOFS chip with integrated PLEDs are of the order of 0.1 %. In other words, one photon is measured at the out-coupling grating for every thousand measured underneath the PLED for the measurement conditions described above. This ratio is dependent on the experimental configuration – e.g. choosing a larger (smaller) grating aperture L_g results in increased (decreased) power ratios. The actual quantity of interest – the PLED-to-waveguide coupling efficiency η, defined as the ratio between the total optical power coupled into the 2D waveguide P_{WG} and the total optical power generated by the PLED P_{PLED} – can be estimated from the measured power ratio as follows: first of all, P_{PLED} is related to the measured external PLED power by

$$P_{\text{PLED}} = \gamma^{-1} \, P_{\text{PLED}}^{\text{meas}}$$

Equation IV-2

where γ is the external coupling efficiency of the PLED. The type of PLEDs implemented here, which are based on very thin anode and EL polymer layers, do not support waveguide modes within the PLED stack, the external coupling efficiency is predicted to be $\gamma = 0.5$ [147]. Next, the total optical power in the waveguide is estimated. For this, one has to consider that; a) only the fraction of the guided light travelling in the solid angle covered by the detector is captured in the measurement and b) part of the light coupled into the waveguide suffers from waveguide losses. Taking this into account, the total power in the waveguide can be estimated to

$$P_{\text{WG}} = 2\,\pi \frac{d_g}{L_g} \, \xi^{-1} \, \kappa^{-1} \, P_{\text{Grating}}^{\text{meas}}$$

Equation IV-3

Here $d_g \approx 7$ mm is the distance between PLED and out-coupling grating (Figure IV.6), $L_g = 4$ mm is the grating length seen by the detector, ξ the fraction of the guided light that does not suffer from waveguide losses and κ the coupling efficiency of the grating with respect to out-coupling toward the substrate. The product of ξ and the grating coupling efficiency is known from laser characterization measurements of the chip and amounts to $\xi \cdot \kappa \approx 0.2$.

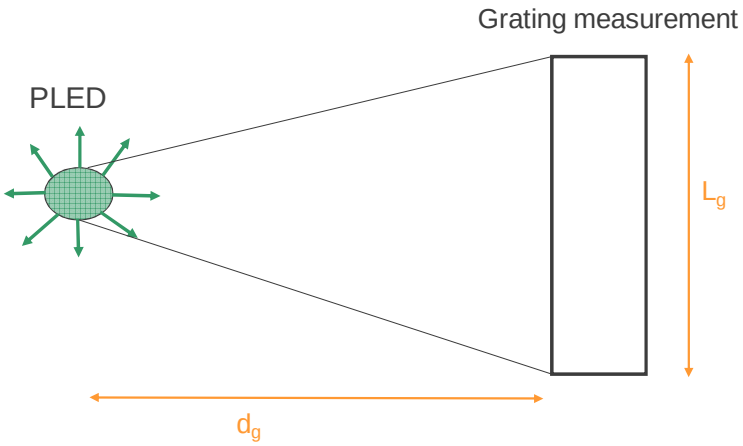

Figure IV.6: Schematic for the estimation of the in-coupling efficiency.

Combining Equation IV-2 and Equation IV-3, and inserting the numbers given in the text the PLED-to-waveguide coupling efficiency can be estimated to

$$\eta = P_{WG} / P_{PLED} = 2\pi \frac{d_g}{L_g} \frac{\gamma}{\xi \cdot \kappa} P_{Grating}^{meas} / P_{PLED}^{meas} \approx 27 \; P_{Grating}^{meas} / P_{PLED}^{meas}$$

Equation IV-4

From the measured power ratios which is in the few per mille regime, a PLED-to-waveguide coupling efficiency of a few percent is thus estimated. For the example taken from Figure IV.5, where $P_{Grating}^{meas} / P_{PLED}^{meas}$ = 1.2 x 10^{-3}, the estimated coupling efficiency amounts to η ≈ 3.2 % when a spacer layer is used.

Sample	d_{Spacer}	d_{ITO}	L_{PLED}	$P_{Grating}^{meas} / P_{PLED}^{meas}$	η @ 8V
S33	130 nm	30 nm	2 mm	2.1 10^{-4}	0.6 %
S34	130 nm	30 nm	0.5 mm	8.1 10^{-4}	2.2 %
S35	130 nm	30 nm	0.2 mm	1.7 10^{-3}	4.6 % @15 V
S44	50 nm	12 nm	0.2 mm	1.2 10^{-3}	3.2 %

Table IV-1: Summary of the performance of those opto-chips with integrated Ir(mppy)$_3$-based PLEDs for which the coupling efficiency was characterized.

The experimentally achieved values for *η* of up to almost 5 % (Table IV-1) are surpassing the theoretical estimation of about 0.6 % (see part II). We explain this by an over-estimation, in the model, of the waveguide loss under the PLED. Although the model calculations are very useful in analyzing the influence of various device parameters, it is difficult to give absolute coupling figures for a particular design. Many material parameters (such as exact location of recombination zone within the electroluminescent layer or complex refractive index of PLED electrode materials) are not exactly known for our structures but have strong influence on coupling efficiencies. Therefore, quantitative values for the coupling figures can only be determined by experimental means.
Moreover, the device optimization is not yet completed and it is very probable that even larger coupling efficiencies will be reached – e.g. by further reducing the optical losses in the anode layer (ITO).
From Table IV-1, we can observe that the efficiency *η* increases when the width (L_{PLED}) of the PLED decreases. This is related to the re-absorption of the guided light by the lossy electrodes (ITO and further away the cathode). By reducing L_{PLED}, the width of re-absorption is limited. However, the total optical power coupled into the single waveguide is reduced compared to larger L_{PLED}.

iii. Conclusions for the direct PLED to waveguide coupling

In this part we propose a device architecture, which – according to our theoretical modeling – guarantees the highest possible efficiency in coupling light from a polymer light-emitting diode into a thin (single-mode) planar waveguide. The coupling mechanism is based on evanescent field coupling, and thus the design must ensure the close proximity of thin-film light source and waveguide. Importantly, the architecture includes an optical spacer layer of

typically 100 nm thickness sandwiched between the waveguide and the lower electrode of the light emitting diode. The function of this spacer layer is to reduce the PLED-induced waveguide losses. Following this concept, light from a PLED was coupled into a single-mode waveguide. The achieved coupling efficiency into the waveguide mode was more than 3 %.
The example given here demonstrates an essential step toward integrated photonic systems based post-processing steps esp. like printing of organic semiconductors. Such an approach opens up the route for system designs like for instance integrated biosensors.
A point that must be underlined here is the fact that the total optical power in the waveguide modes is comparatively small. The PLEDs emit a power of the order of 1 to 10 μW. With a coupling efficiency of the order of a few percent this results in 10 to maximal 1000 nW power in the two-dimensional waveguide.
Moreover, the main problem encountered is the low coupling efficiency of the PLED into the TM waveguide mode. With respect to the polarization state of the out-coupled light, we have only been able to observe TE so far. This is a serious issue. For the SPR detection scheme targeted in SEMOFS, coupling into the TM mode is indispensable, since surface plasmons interact with TM polarized light only. Experimentally, we have verified that the PLED does indeed emit TM light by studying the polarization state of the substrate edge emission. Thus, the TM part is either not coupled into the waveguide, or it suffers from strong losses in the waveguide, or it is not coupled out efficiently by the out-coupling grating. The latter two explanations can be ruled out, since waveguide losses as well as grating efficiency are comparable for the two polarization states. Experimental explanation of the absence of the TM mode is provided in the next paragraph.

b. Influence of the proximity of the PLED on the waveguide modes

There are two drawbacks in the direct PLED-to-waveguide coupling techniques: a) the TM mode is suppressed or not coupled, which is not acceptable for a SPR detection scheme. b) in-coupling light intensity is rather low. As already mentioned, the PLED contains optically lossy layers such as the indium thin oxide and the metallic cathode. Losses of the waveguide underneath the PLED are of the order of 1000 cm^{-1}.

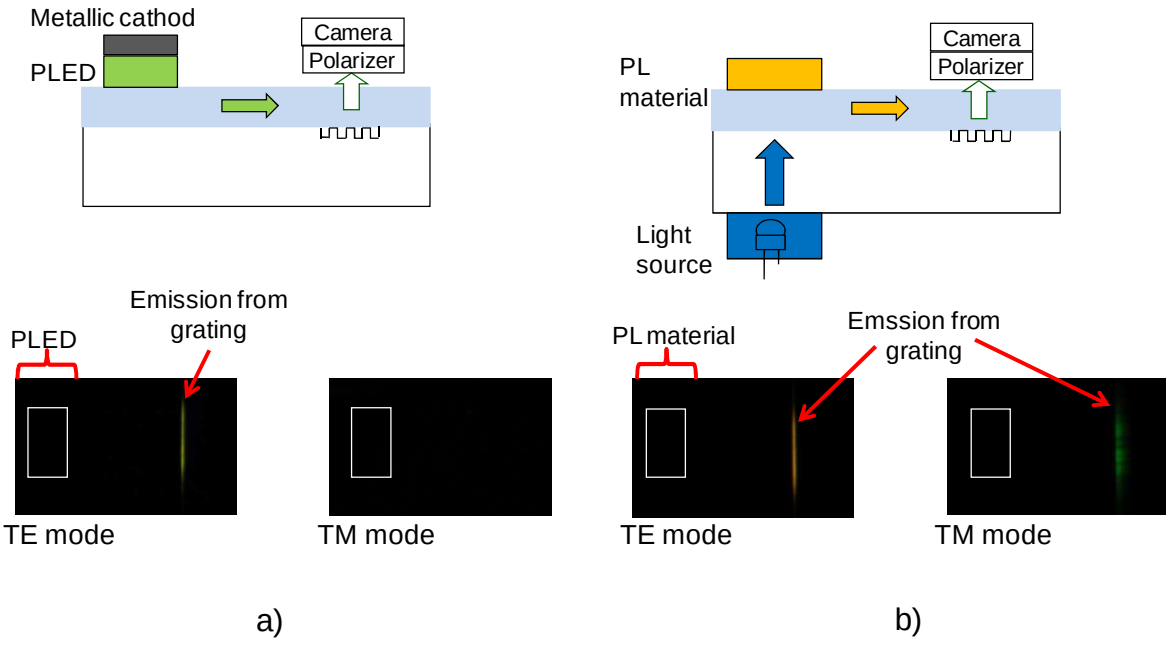

Figure IV.7: Effect of metallic electrode on the coupling of the electroluminescent light to the waveguide modes. Out-coupled light from the grating a) without the metallic electrode, and b) with the metallic electrode.

In other words, the intensity of the guided light is dampened on a characteristic length scale of D = 10 µm. In other terms, only light coupled into the waveguide within a distance of 1 - 2 times D from the PLED edge survives; the remainder is dampened by the proximity of the electrodes. Thus, the in-coupled light intensity remains weak.
Theoretical and experimental work was undertaken to understand why the coupling into the TM polarized waveguide mode was not possible. The absorption in the metallic electrode of the PLED was suspected. The change from aluminum to silver based electrode should have improved the efficiency but it is not sufficient, and the absorption due to the electrode material is too high. This was demonstrated in a simple experiment using an electroluminescent material covered by a metallic electrode pumped optically and compared to the same configuration without the electrode. As it can be seen in the Figure IV.7, the effect of the metallic electrode is clearly seen and it suppresses the coupling with the TM polarized waveguide.
The conclusion is that for TE polarization, the field at the cathode layer is almost zero; however for TM polarization there is a local maximum (see Figure IV.8).

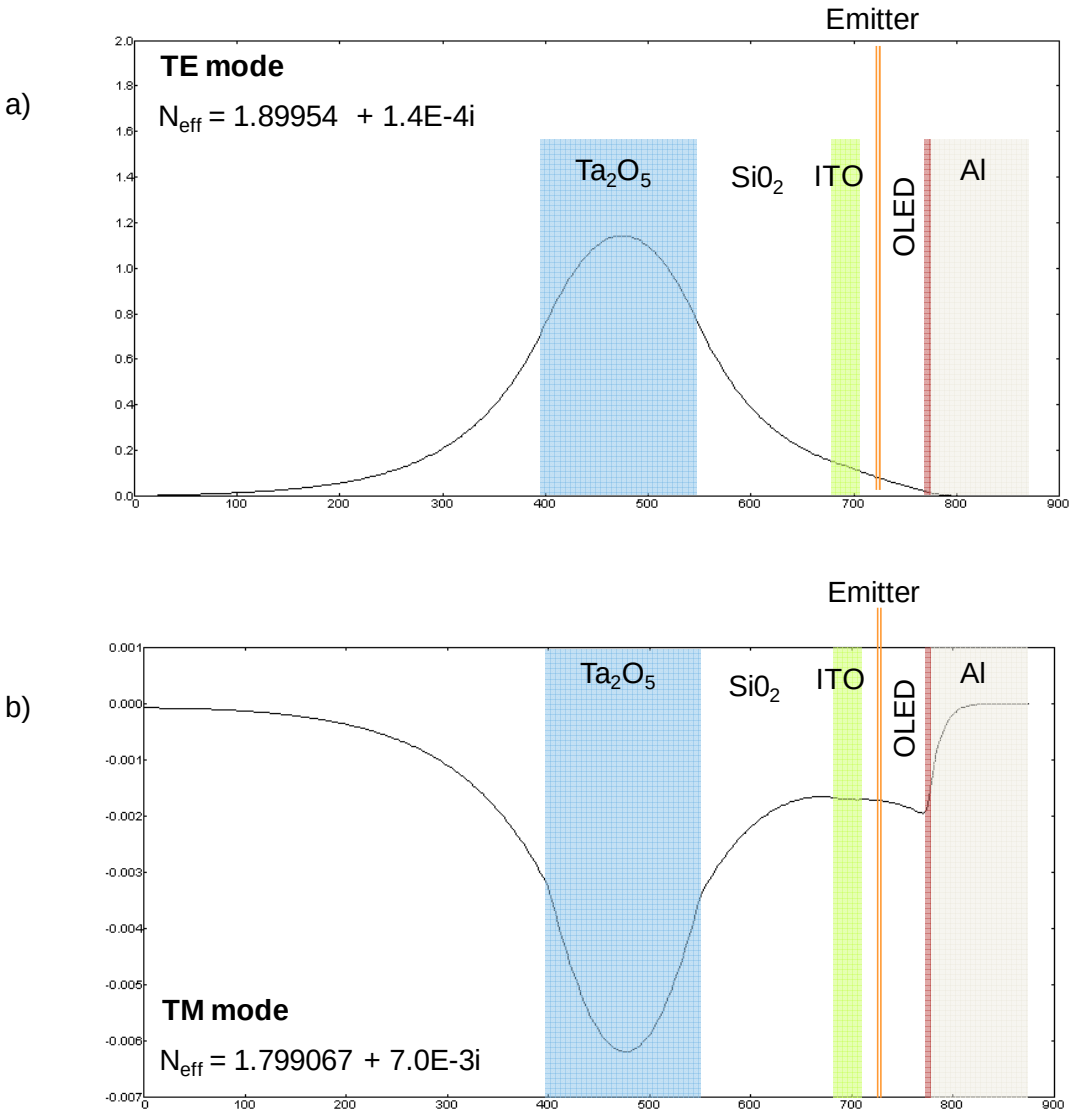

Figure IV.8: Mode solver of (a) TE mode and (b) TM mode for the direct PLED to waveguide configuration.

With the effective index we can see that the waveguide losses are 50 times higher in the case of TM mode compare to TE mode. As seen on Table IV-2, the exchange of metallic cathode does not reduce the large losses related to the TM mode.

Material	TE	TM
Silver	1.886 + 1.7E-4 i	1.767 + 3.7E-3j
Gold	1.886 + 1.7E-4j	1.767 + 7.3E-3j
Al	1.886 + 1.7E-4j	1.776 + 5.1E-3j
Silver / no Ba	1.886 + 1.7E-4j	1.760 + 3.0E-3j
No Metal	1.886 + 1.7E-4j	1.772 + 2.7E-4j

Table IV-2: Effective index of TE and TM modes for different metallic cathodes.

c. *Indirect PLED-to-waveguide coupling*

This new unexpected findings force us to modify the system design in order to be compatible with a design that allows TM coupling to have the plasmon interaction and an integrated version using polymeric source and detection.

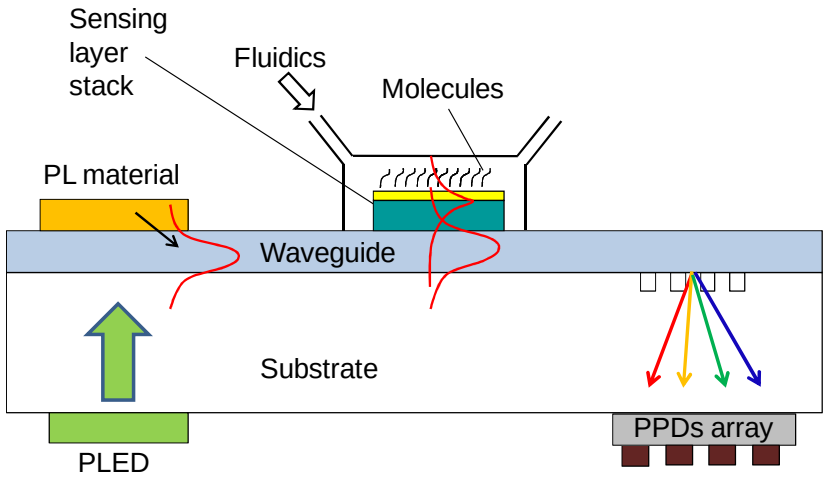

Figure IV.9: Second architecture of the opto-chip with PL material for in-coupling.

i. Advantages of the indirect coupling

The new design proposes an indirect PLED-to-waveguide coupling in the way that the PLED emission was used to pump a PL material layer which is located on top of the waveguide, as depicted in Figure IV.9. This architecture offers the advantage of relocating the lossy electrode layer far from the waveguide and thus allows coupling both TE and TM into the waveguide. Figure IV.7 shows the extracted light at the out-coupling grating under TE or TM polarization with a power TE/TM ratio of 2.5. Another advantage of this second architecture –

with a PL layer as an intermediate material – is the possibility to couple more light into the waveguide by increasing the PL material layer length *L* at the same time as the optical pump power. The advantage of using a PLED as optical pump source is that it can easily be scaled in size dimensions and therefore permits the increase of the optical power in the waveguide, as shown in Figure IV.10. Indeed, the coupled optical power is exponentially proportional to the area of the pumped PL material according to Equation IV-5 with the related drawing in Figure IV.10.

$$P_{out}(L) = \int_{-(L+d)}^{-d} \underbrace{dx \cdot C}_{dP} \cdot \exp[\alpha_L \cdot x] = \frac{C}{\alpha_L} \cdot \exp(\alpha_L \cdot x)\Big|_{-(L+d)}^{-d} = \frac{C}{\alpha_L} \cdot [\exp(-\alpha_L \cdot d) - \exp(-\alpha_L \cdot (L+d))]$$

$$= \frac{C}{\alpha_L} \cdot \exp(-\alpha_L \cdot d) \cdot [1 - \exp(-\alpha_L \cdot L)]$$

Equation IV-5

with *C* the power coupled into waveguide per unit length of the PL layer, α_L waveguide loss, *L* the length of PL material and *d* the distance from the edge of the PL layer to the out-coupling grating.

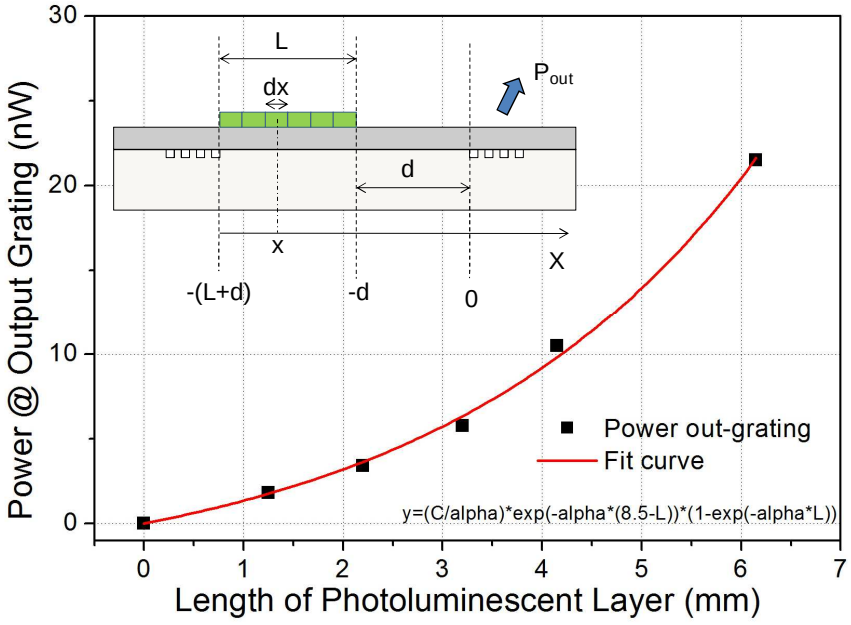

Figure IV.10: Increase of coupled optical power by scaling up the area of the PL material (F8BT).

The exponential behavior is related to waveguide loss that is reduced (*d* ↘) when the PL material length increases. Of course, the power being coupled into the waveguide does not grow infinitely, but it does actually saturate. The highest out-coupled power occurs when the PL layer is of infinite length and reaches the out-coupling grating. In that case, Equation IV-5 simplifies to Equation IV-6:

$$P_{\max} = \frac{C}{\alpha_L} \cdot \underbrace{\exp(-\alpha_L \cdot d)}_{\xrightarrow{d \to 0} 1} \cdot \left[1 - \underbrace{\exp(-\alpha_L \cdot L)}_{\xrightarrow{L \to \infty} 0} \right] \xrightarrow[L \to \infty]{d \to 0} \frac{C}{\alpha_L}$$

Equation IV-6

This power increase is not possible when direct PLED-to-waveguide pumping is used, due to electrode re-absorption as discussed above.
This indirect coupling allows the coupling of a high intensity of light into the waveguide.
Figure IV.11 shows the optical power measured at the out-coupling grating for different in-coupling configurations. The direct PLED to waveguide coupling exhibits the minimum coupled light power into the single-mode waveguide with maximum measured out-coupling light of 11 nW at 12 V. Indirect coupling with PL material was tested with Poly[9,9-dioctylfluorenyl-2,7-diyl)-co-1,4-benzo-{2,1'-3}-thiadiazole) F8BT and MEH-PPV as PL layer. As seen in Figure IV.11, MEH-PPV enables to couple more light inside the waveguide compared to F8BT. Maximum measured out-coupling light with the indirect coupling based on MEH-PPV is about to 650 nW for a surface area of 2 x 10^{-2} cm^2. Thus, we can couple 50 times more light inside the waveguide by using the indirect coupling compared to the direct PLED-to-waveguide coupling.

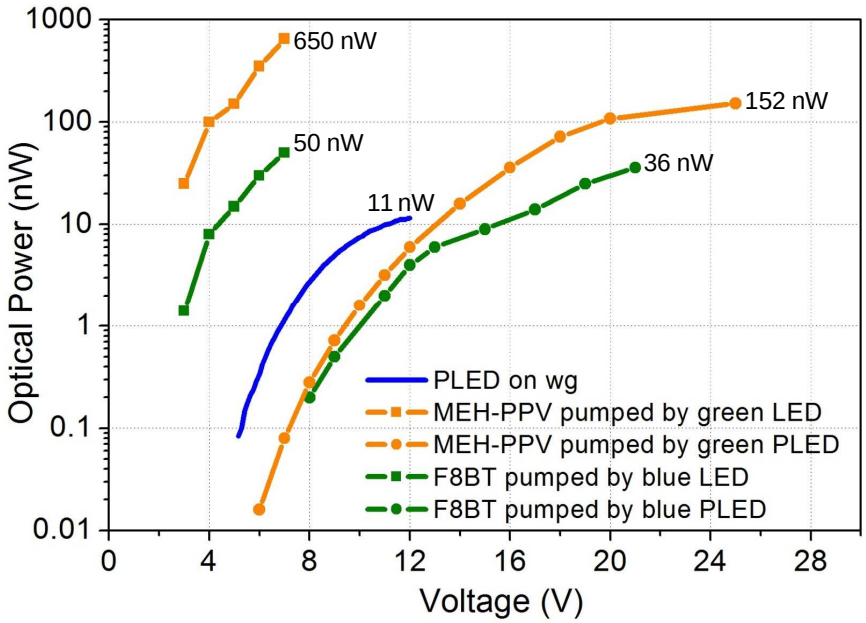

Figure IV.11: Comparison of the coupling power measured at the out-coupling grating stage (surface 0.5 x 4 mm^2) for the direct PLED to waveguide (blue curve) coupling techniques and the indirect PL material to waveguide technique. F8BT (green curves) and MEH-PPV (orange curves) have been tested as PL materials. Inorganic (square markers) and organic (round markers) light source have been used to pump the PL materials.

ii. Estimation of the indirect PL material to waveguide coupling

By following the same approach as for the estimation of the coupling efficiency from the PLED to the waveguide, we measured the power at the PL material stage and the power at the out-coupling grating with values of $P_{\mathrm{PL}}^{\mathrm{meas}}$ = 8.2 µW and $P_{\mathrm{Grating}}^{\mathrm{meas}}$ = 0.075 µW, respectively. By applying Equation IV-4, we obtain an in-coupling PL to waveguide efficiency of $\eta \approx 31\%$ with $d_g = 5.5$, $L_g = 5$ and $\gamma = 1$ (assuming complete extraction of PL generated photons).

From a theoretical point of view, we also estimate the PL material-to-waveguide efficiency as schematized in Figure IV.12.

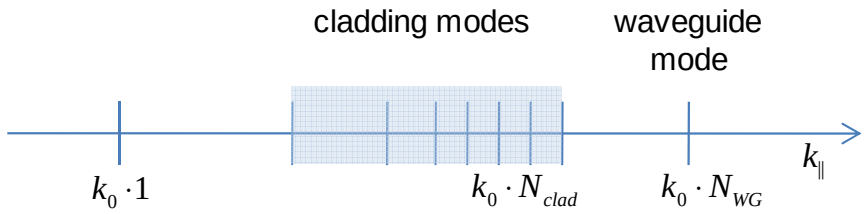

Figure IV.12: Simple modes representation.

As already mentioned in part II, the density of modes in free space follows n^2. So the power coupled into all modes is proportional to the square of the effective index of the waveguide:

$$P \propto N_{WG}^2$$

Equation IV-7

The power coupled into all modes apart from the waveguide is proportional to the square of the highest effective index of the cladding modes:

$$P \propto N_{clad}^2$$

Equation IV-8

In our case, cladding is the glass substrate.
The relative power inside the waveguide, which correspond to the efficiency, is defined by

$$\eta = 1 - \frac{N_{clad}^2}{N_{WG}^2}$$

Equation IV-9

With N_{wg} = 1.8 and N_{clad} = n_{glass} = 1.45, we obtain η = 35%. This is similar to what we observed experimentally.

The guided light has now to be sensed via a detection system. The out-coupling grating combined with an array of PPDs acts as an integrated organic spectrometer.

2. Detection at the out-coupling stage: integrated organic spectrometer

A fully organic mini-spectrometer compatible with monolithical integration on optical chips was developed within the framework of this thesis. It consists of a single-mode waveguide with integrated diffraction grating and a dense array of PPDs as sensing elements.
The out-coupling grating diffracts the guided light of a given wavelength to a specific out-coupling angle. The integration of the organic PPD array onto the chip allows to track – in a straightforward and inexpensive way – the spectral changes due to interaction with the analyte.
As detailed in the previous chapter, PPDs have been optimized in order to be used as detection elements of a miniaturized organic spectrometer. External Quantum Efficiency of 70%, on/off ratio of 10^6, dark current below 10 nA/cm^2 at -1 V and a lifetime larger than 3000 hours have been obtained [144].

a. *Mask design*

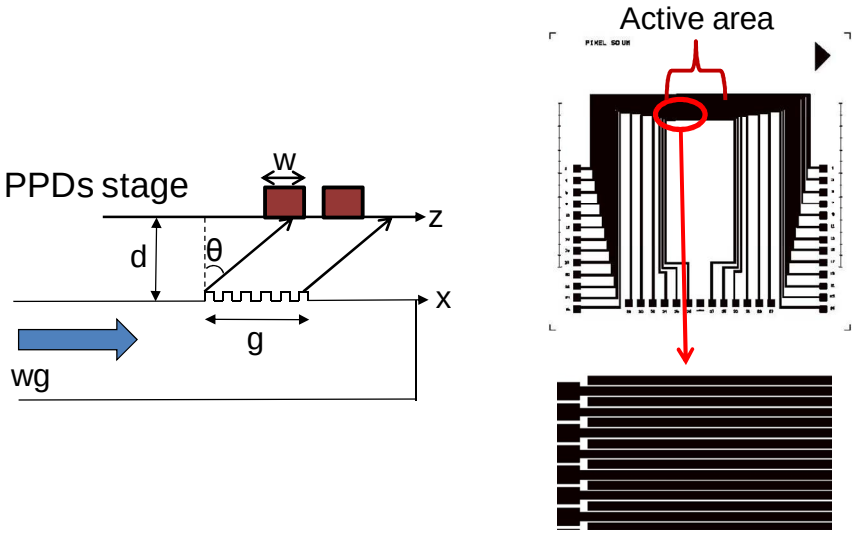

a) b)

Figure IV.13: a) Sketch of a simple model to calculate the spectral resolution. b) ITO mask for organic spectrometer.

A simple model has been used to design the ITO mask for the PPD array (Figure IV.13). Starting from the modified grating equation, guided light is diffracted into angles θ according to Equation IV-1.
According to Figure IV.13 a, varying the abscisse and taking into account that sin(θ) ≈ tg(θ) for small angles results in:

$$Z = X + d \cdot tg(\theta) \approx X + d(N - \frac{\lambda}{\Lambda})$$

Equation IV-10

This approximation leads to a linear relationship between wavelength and spatial *z* position. Without this approximation, which is only valid for small angles theta, the relationship becomes non-linear.
The pixel or digital resolution is the spectral bandwidth which is detected by one pixel and is determined by the width *w* of the pixel and the linear dispersion *dλ/dz* of the spectrum (see Figure IV.13) according to

$$\Delta\lambda = w \cdot \frac{d\lambda}{dz}$$

Equation IV-11

For small variations, *dz* is defined by

$$dz \approx d \cdot \frac{d\theta}{\cos\theta}$$

Equation IV-12

So, Equation IV-11 becomes:

$$\Delta\lambda \approx w \cdot \frac{d\lambda}{\frac{d}{\cos\theta} \cdot d\theta}$$

Equation IV-13

Combining Equation IV-13 and the derivative of Equation IV-1 with respect to λ, we obtain:

$$\Delta\lambda \approx \frac{w \cdot \cos^2\theta}{d \cdot \left(\frac{dN}{d\lambda} - \frac{1}{\Lambda}\right)}$$

Equation IV-14

With $dN/d\lambda$ = -5.10^{-4} m^{-1}, w the pixel width, Λ = 312 nm the grating period, d = 0.8 mm the distance between the grating and the PPD array, and θ the out-coupling angle.
For a theoretical resolution of $\Delta\lambda$ = 5 nm, the pixel width has to fix at 13 µm. Thus, the PPDs were patterned into a 40 pixels linear array of w = 10 µm pixel width and p = 15 µm pitch using standard photolithography. Different masks were designed which allowed achieving spectral resolutions ranging from 50 nm down to 5 nm.
The highest spectral resolution mask, as illustrated in Figure IV.13 b, consists of 10 µm x 3.4 mm (width x length) PPD pixels with 5 µm spacing between two adjacent PPD pixels. The detected photocurrent is amplified and converted into a voltage. This photovoltage is then read out using a Keithley 2701 with a 40 channel Diff Mux module Keithley 7702.

b. Results

The guided light is diffracted by the grating and is detected by the organic spectrometer. The PL material has been pumped either by a green PLED – for a fully organic test – or by an inorganic LED. The solution processed PLEDs are less bright compared to the high-efficiency and high-power inorganic LEDs with a luminance of 10 cd at 20 mA.
It should be mentioned that the periodic grating used has several drawbacks. According to the grating equation, discrete wavelengths are coupled out into to discrete angle. As seen in Figure IV.14 a, there is no linear relationship between the PPDs response and the spectral resolution. Indeed, for a given out-coupling angle variation $\Delta\theta$, the illuminated surface of the PPD array and therefore the spectral resolution can be different according to the out-coupling angle. Furthermore, the grating has a lateral extent of 500 µm and therefore cannot be considered as a point source in this detection geometry. As seen in Figure IV.14 b, the diffraction along the length of the grating results in spectral crosstalk on individual detector pixels. Ideally, one PPD pixel would detect preferentially only one wavelength from one point of the grating. These problems can be significantly reduced by using either a hemispherical PPD array or a chirped grating and will be the subject of further experiments. The hemispherical PPD array mitigates the problem that the wavelength resolution depends on angle and wavelength, respectively. The hemispherical pixel array avoids making the pixels at the periphery of the array wider. The chirped grating mitigates the problem of spectral cross-talk.

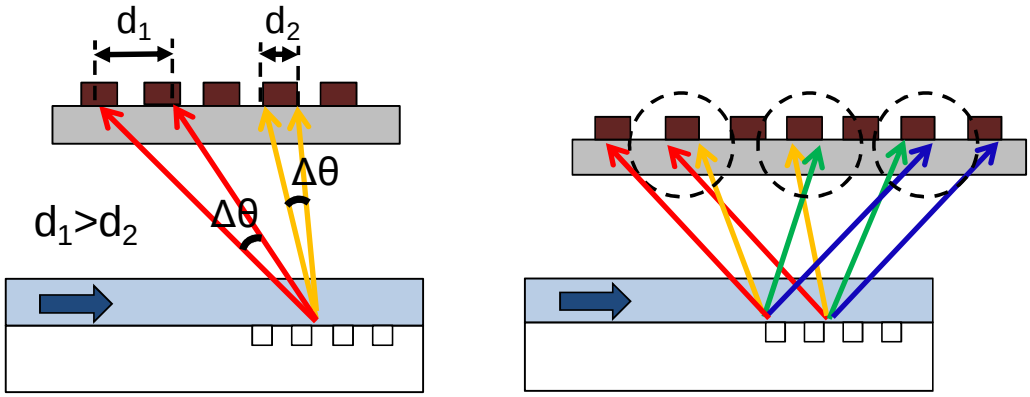

Figure IV.14: Artefacts present in the integrated organic spectrometer relate to the periodic nature of the grating; (a) for a fixed Δθ, the illumination area according to the wavelength (out-coupling angle) is different and (b) crosstalk between pixels is due to the spatial extent of the grating.

Figure IV.15 shows spectra obtained with the organic spectrometer with inorganic LED (a) and PLED (b) as pump light source for the PL material. In Figure IV.15 a, width and separation between individual PPDs are 10 µm and 7 µm, respectively. The estimated spectral resolution is $\Delta\lambda \approx 5$ nm. In Figure IV.15 b, width and separation between individual PPDs are 20 µm and 10 µm, respectively. The estimated spectral resolution is $\Delta\lambda \approx 7$ nm.
Due to the lower intensity of the PLED, we had to choose a larger pixel size in order to still obtain a satisfactory signal-to-noise ratio.

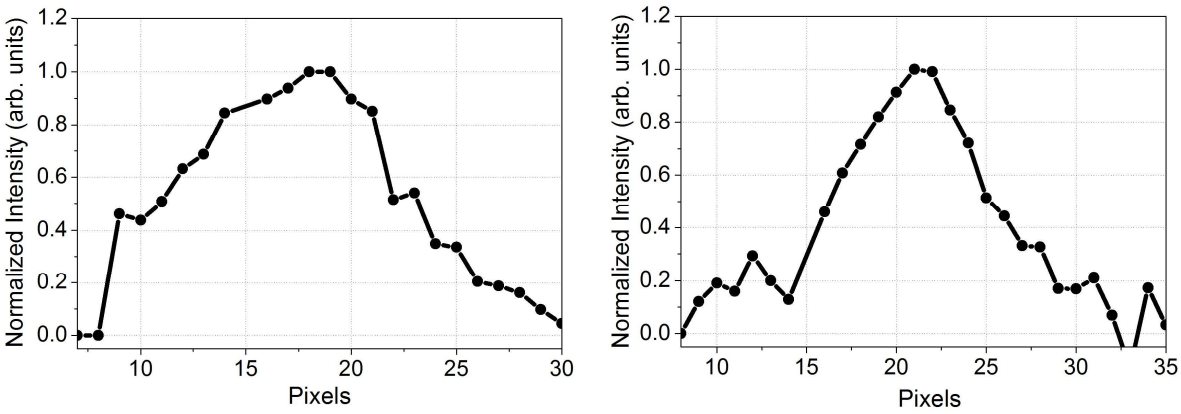

Figure IV.15: Spectra measured with the organic spectrometer with an indirect coupling technique as the in-coupling scheme: (a) PL pumped by inorganic LED, (b) PL pumped by organic green LED.

Experimental spectral resolution was inferred by comparing the FWHM bandwidth (70 nm) of the guided light from the PL material and a green laser with the spectra obtained with the PPD array (Figure IV.16) and with a standard lab spectrometer. By taking into account that the PPDs have a sensitivity cut-off at 640 nm (Figure III.36), we could estimate the FWHM of the guided light at 60 nm. We fit the spectrum measured by the PPD array to the one measured with a fiber – located right on top of the out-coupling grating – connected to an inorganic spectrometer. Fitting parameters were the central wavelength and intensity values at 20% of the maximum. In the case, for e.g., of the laser guided light, two pixels of the

organic spectrometer are above the FWHM of the laser which is 10 nm. From this analysis we derive a spectral resolution of the organic spectrometer of $\Delta\lambda \approx 5$ nm.

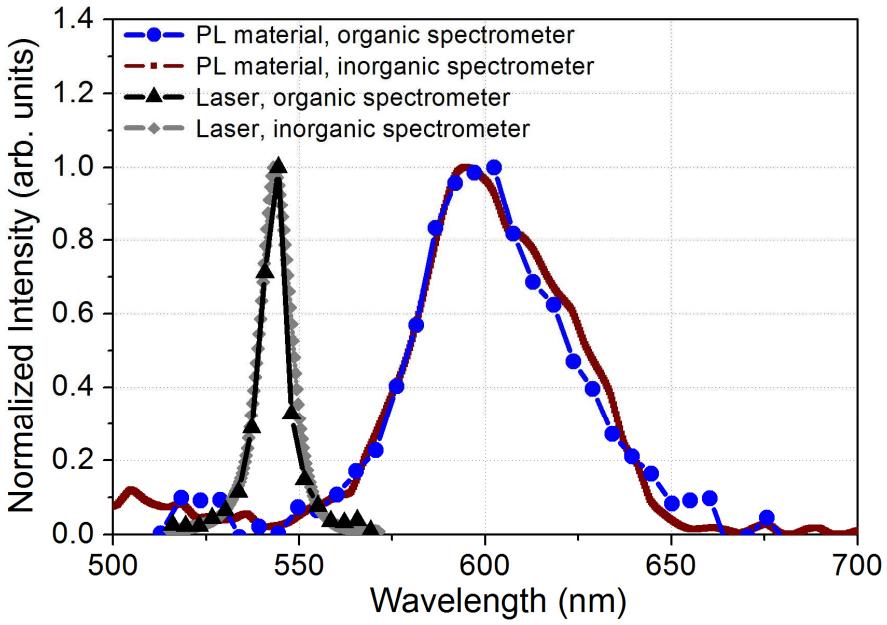

Figure IV.16: Spectrum of the guided light after out-coupling by the grating as detected by the organic spectrometer (blue line and rounds markers). For comparison the spectrum as detected by a standard lab spectrometer is also shown (red squares). The standard spectrometer integrates over an area similar to the PPD-spectrometer's area. Thus, the influence of the grating out-coupling angle is similar for both measurements. Spectra of guided green laser measured with the organic spectrometer (dark triangles) and the inorganic spectrometer (grey diamonds) is shown.

This experiment allows to calibrate our organic spectrometer, and thus to relate pixel numbers to wavelength values (Figure IV.16). Alternatively and for a better calibration, different lasers have been used to precisely calibrate the organic spectrometer.

c. *Summary on the organic spectrometer*

In summary, we have demonstrated – for the first time – the fabrication of an integrated organic spectrometer based on an array of PPDs. Pixel to pixel spectral resolution of $\Delta\lambda \approx 5$ nm FWHM was achieved with this set-up when the PL material is pumped by an inorganic LED (Figure IV.15 a). By using a PLED (Figure IV.15 b), a spectral resolution of $\Delta\lambda \approx 7$ nm was achieved. Signal-to-noise ratio in both cases was about 10.
The presented results validate the grating / PPD line sensor as a fully functional spectrometer that can be easily integrated into a lab-on-chip platform and as such represents an important building block for disposable low-cost bio- and chemical sensors. Other applications requiring low cost and / or fully integrated spectrometers can be pursued based on the present results.

3. Toward biosensing applications

a. Absorption biotest

With the organic platform (PLED, PL material and PPD array), we performed absorption tests. An opto-chip without plasmon stack was used together with a simple fluidic system (Figure IV.17). A flow-through cell was micromilled in polymethyl methacrylate (PMMA) and had two steel tubing fluidic connectors. Double-sided laser cut tape of 200 µm in thickness defined the shape of the channel and was used to bond the fluidic cartridge to the test chips. The cartridges were transparent for the first tests and black at a later stage to suppress light scattering. The channel had a width of 1 mm and a height of 200 µm.

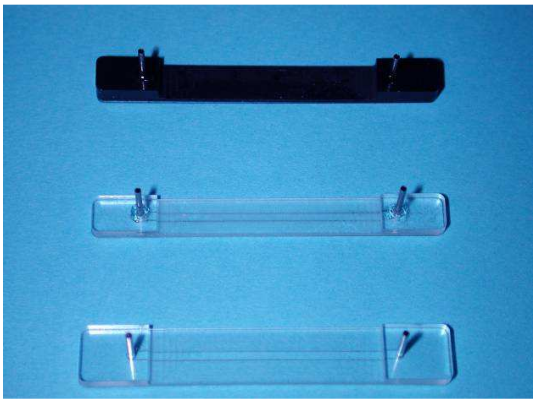

Figure IV.17 : Fluidic flow-through cartridges. The channels are defined by laser-cut bonding tape.

An anti-mouse immunoglobulin G (IgG) marked with Cy5 fluorophore was placed in close vicinity of the waveguide. First, the waveguide was functionalized by a mouse IgG that was injected into the fluidic cell. Then, the anti-mouse IgG with the fluorescent marker was injected into the fluidic cell which then linked to the mouse IgG (Figure IV.18 b).
As fluorophore marker, we used Cy5 with peak absorption at 650 nm (Figure III.36). As seen in this figure, the absorption spectrum of the Cy5 overlaps with the guided light.
In a first step and before any fluid was injected into the channel, an initial spectrum was taken at time t1. This reference spectrum is marked with blue line and squares in Figure IV.18 a. Next, the waveguide's surface was functionalized with mouse immunoglobulin G (mIgG) that was injected into the fluidic system with a syringe. A schematic diagram of the situation after functionalization is given in the middle panel of Figure IV.18 b. After functionalization with mIgG a spectrum was again taken at time t2 (dark red line and triangles in Figure IV.18 a). The presence of the mIgG at the waveguide's surface led to a clear red-shift in the spectrum of the guided light.
At this stage, a 50 µg/mL solution of anti-mouse IgG with the fluorescent marker Cy5 (α-mIgG) was injected into the fluidic channel and bound to the available mIgG at the waveguide's surface, as sketched in the lower panel of Figure IV.18 b. As seen from the spectrum taken after binding had occurred at time t3 (red line and circles in Figure IV.18 a) the presence of the α-mIgG at the surface of the waveguide induced an almost total absorption of the guided light. Due to its absorption properties – strong absorption over the entire spectrum of the guided light as seen in Figure III.36 – Cy5 had the ability to quench the initial spectrum of the guided light almost completely. Note that rather than using Cy5 as a fluorescent marker as is usually done in biological experiments it was used as a pure quencher here. Moreover, the fluorescence of the Cy5 lies outside the wavelength range of the detector.

In a next step Integra cleaner, which is a surfactant, was injected into the fluidic system, as an effect of which the α-mIgG is specifically removed. The spectrum taken, at time t4, is marked with light orange line and reverse triangles in Figure IV.18 a. Its similarity to the spectrum taken at t2, just after functionalization of the surface, is obvious and proves the almost complete specific removal of the α-mIgG from the waveguide's surface. The observed differences between the spectra t2 and t4 are very likely due to residues of α-mIgG in the vicinity of the surface of the waveguide.
As a last step, a solution of hydrochloric acid (HCl) at 0.1 mol/L was injected into the fluidic channel. As a result, the mIgG was removed from the surface of the waveguide and the initial situation – top panel of Figure IV.18 b – should ideally be restored. The spectrum measured after cleaning at time t5 (dark blue line and pentagons in Figure IV.18 a) closely resembled the initial reference spectrum t1. The observed differences between the spectra t1 and t5 (mainly a suppression of t5) are very likely a result of residues in the vicinity of the surface of the waveguide.
From the concentration of the α-mIgG solution (50 µg/mL) and the mass of the mIgG molecule (150 kDaltons), the sensitivity of the immunoassay can be estimated to better than 50 x 10^{-3} / 150 000 = 333 nanomolar.
It is clear from Figure IV.18 a, that the situation "no specific binding of α-mIgG has occurred" can easily be differentiated from the situation "specific binding of α-mIgG has taken place" on the basis of the LOC experiment performed here. Therefore, this experiment is a proof of concept for absorption biological tests based on an organic integrated platform.

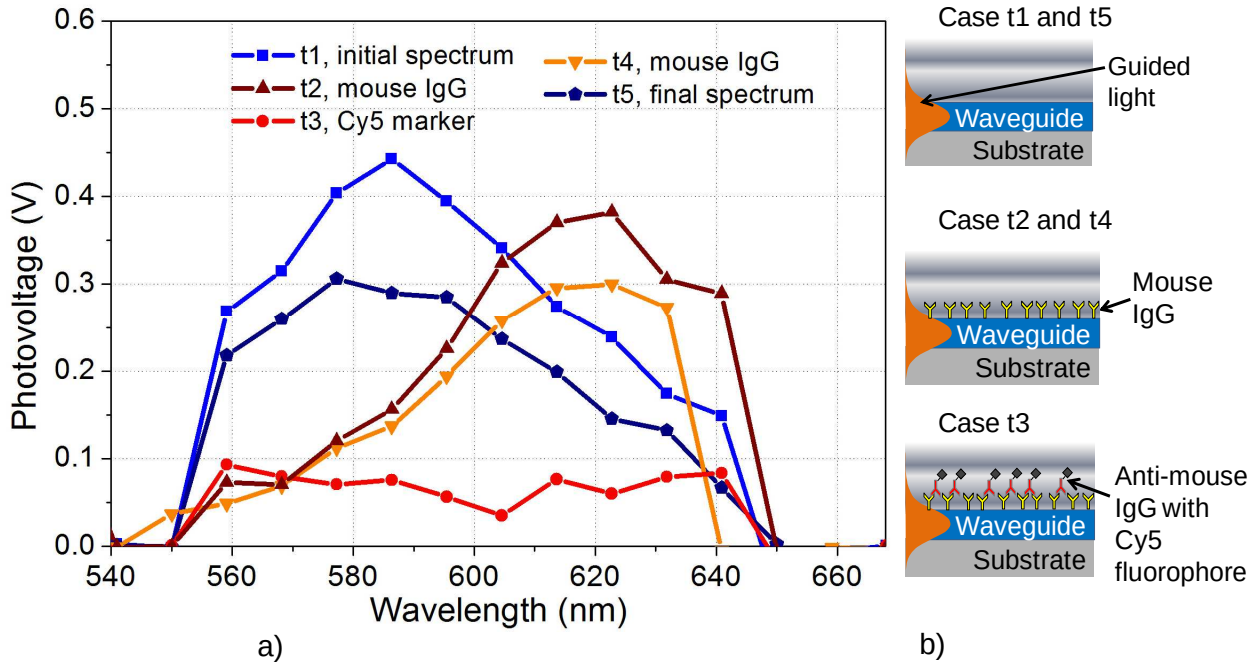

Figure IV.18: (a) Evolution of the out-coupled spectrum of guided light according to the evanescent interaction with the component located in the fluidic channel. (b) Principle of the different cases of the absorption bio-test.

b. *Proof of concept of refractive index sensing reaction with a plasmon stack*

In order to obtain a high sensitivity biosensor, the use of a resonant system is of key importance. On one opto-chip including the plasmon stack we tried to detect a wavelength shift of the plasmon peak by changing the refractive index of the fluid in contact with the

stack. For a specific wavelength range fulfilling the phase-matching condition, light couples from the waveguide into the surface plasmon mode and is subsequently absorbed. The resulting absorption dip is sensitive to the surrounding media and shifts to longer wavelengths for increasing refractive index of the surrounding media. The refractive index was changed by depositing water on the stack. The principle of the SPR is that solution – located on top of the stack – with refractive index higher than 1 induces a partial absorption of the spectrum. As a matter of fact, this experiment is a first step toward a label-free high-sensitivity biosensor based on organic optoelectronic material.
The opto-chip and the plasmon stack used for these experiments had been characterized (grey plot on Figure IV.19) with an inorganic system; providing a comparative test.

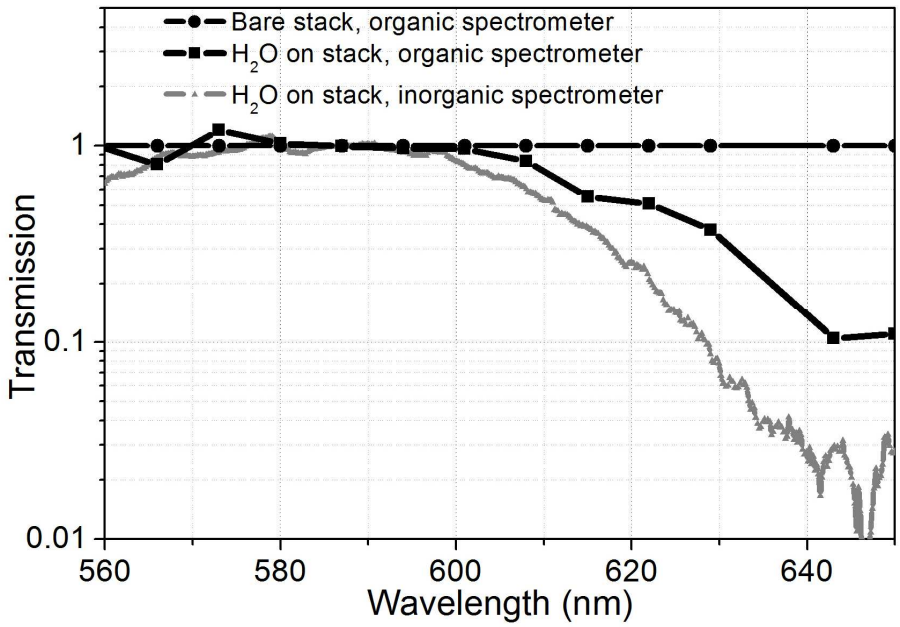

Figure IV.19: Experiment based on the surface plasmon resonance detection scheme. The change of transmission of the SPR stack upon deposition of a water droplet (n = 1.33) on the stack's surface is shown, as measured with the organic mini-spectrometer (black line and squares) and the standard lab spectrometer (grey line and triangles). A clear suppression of transmission in the red part of the spectrum can be observed when water is placed on the SPR stack.

Since the SPR is by definition polarized TM, a polarizer was inserted between the out-coupling grating and the PPD array in order to observe the SPR interaction only. Consequently, the signal was a bit weaker and the medium spectral resolution PPD mask had to be used in order to maintain a good signal to noise ratio.
As seen in Figure IV.19, the plasmon stack – based on gold – does not present an absorption peak as sharp as expected. In the presence of water, one observes a transmission cut-off at 600 nm rather than a transmission dip. The problem of achieving a good plasmon stack is attributed to the high refractive index of the Ta_2O_5 waveguide which renders the phase-matching between the waveguide and the plasmon stack mode difficult.
Without the presence of an analyte (just air), the plasmon stack does not modify the guided light. After depositing regular tap water (n = 1.33) onto the plasmon stack, absorption of the guided light is detected for wavelengths > 600 nm. When the PPD array of spectral resolution of 10 nm was used, we observed a decrease in intensity in the red part of the spectrum.

To determine the sensitivity (in pg/mm^2) of this SPR platform, we use the spectral resolution of the organic spectrometer which is $\Delta\lambda \approx 5$ nm. The theoretical peak width of SPR is ≈ 20 nm. So we can determine the number of effective pixels as $n_{pix} \approx 4$. There is no exact definition of this number, but for an estimate we can take the number of pixels that "see the

peak“, i.e. that fall in the range of say 10% to 100% of the maximum peak high. The detector spectral resolution $\Delta\lambda$ is replaced by the peak (or rather dip) position determination accuracy $\delta\lambda_{adv}$ resulting in the biosensor resolution. For a “typical“ situation, a sub-pixel resolution in the order of

$$\delta\lambda_{adv} = 2\,\Delta\lambda / n_{pix} \qquad \text{(nm)}$$

Equation IV-15

gives a reasonable estimate. Thus $\delta\lambda_{adv} = 10 / 4 = 2.5$ nm.
The sensitivity is defined by

$$\delta\Gamma_{adv} = \delta\lambda_{adv} / S_{CO} \qquad \text{(ng/mm}^2\text{)}$$

Equation IV-16

where the chemo-optical sensitivity S_{CO} is expressed by the change $\Delta\lambda$ per $\Delta\Gamma$ (pg/mm^2) mass adsorption to the surface according to

$$S_{CO} = \Delta\lambda / \Delta\Gamma$$

Equation IV-17

where Γ denotes the surface mass coverage on the sensing pad (pg/mm^2). As an example of the studied SPR sensing pad, the wavelength shift due to adsorption of one IgG monolayer is $\Delta\lambda_{SPR}$ = 10.5 nm. For a monolayer of IgG, $\Delta\Gamma$ is estimated at 5 ng/mm^2 [148] Thus S_{CO} = 2.1 nm/(ng/mm^2).
And finally, using Equation IV-16, we can estimate the device sensitivity at $\delta\Gamma_{adv} = \delta\lambda_{adv} / S_{CO} \approx 2.5 / 2.1 \approx 1.2$ ng/mm^2. The reason for this large value is that the number of pixels is too low and dynamic range is too large.
By increasing the spectral resolution of the integrated organic spectrometer to the best designed mask resolution of $\Delta\lambda$ = 2 nm, the device sensitivity could reach $\delta\Gamma_{adv}$ = 480 pg/mm^2.

In summary, a proof of concept for spectral changes correlated to refractive index modification on the surface of the plasmon stack was demonstrated. This is an important step forward toward label-free sensitive biosensors based on organic electronic light source and / or detector.

4. Summary on the biosensor applications

A biosensor based on organic optoelectronic building blocks was successfully implemented on a single-mode waveguide, which represents an important step toward lab-on-a-chip sensors. PLED Lambertian emitters were coupled into single-mode waveguides by an evanescent scheme either directly or indirectly by optically pumping a PL material. As detection stage, a PPD line sensor array and a grating were used as integrated organic spectrometer. Pixel-to-pixel spectral resolution down to 5 nm was reached. An absorption biotest was successfully achieved with this biosensor platform based on organic materials. In order to reach higher sensitivity, a resonant plasmon stack was implemented. Proof of concept of a spectral change induced by the refractive index change of the fluid surrounding the plasmon stack was demonstrated.
Optimization of the spectral resolution of the organic spectrometer can be achieved in different ways – e.g. by reducing the dimension of each PPD or by increasing the distance between the PPD array and the grating. In order to maintain a good signal-to-noise ratio, the coupled light can be significantly increased by up-scaling the dimension of the PLED and PL material.

V. Conclusions and outlook

Our information society has a seemingly insatiable need for microelectronic devices for cheaper price, while offering at the same time identical functionality. This need spurred research for alternative processing methods for semiconductors. In particular, the novel field of organic semiconductors appears very promising for many applications: compared to their inorganic counterparts, organic semiconductor materials and devices offer numerous desirable properties and technological advantages, i.e. their mechanical flexibility, the large area of the produced devices and systems, the simplicity of processing and, consequently, their low cost.
In the present thesis work, we investigated the integration of active and passive organic components onto an opto-chip forming a hybrid photonic system. The motivation for this research was the development of a fully integrated, cost-effective and therefore disposable biosensor. This lab-on-a-chip system has to be compatible with large-scale mass production techniques in order to become a truly low-cost disposable product.

To this end, solution-processed organic optoelectronic components were deposited by spin coating or ink-jet printing techniques onto an inorganic opto-chip made of a Ta_2O_5 single-mode waveguide on a glass substrate with a grating for out-coupling and detecting the guided light. Alternatively, this concept can be easily adapted to cheaper polymer waveguides with embossed gratings.

Coupling light from a Lambertian, extended light source into a single-mode planar waveguide chip with practically useful efficiency was successfully demonstrated by employing an evanescent coupling scheme.
In a first realization, a PLED – monolithically integrated on top of the waveguide – directly excites the waveguide mode by using a spacer layer. A second embodiment consists of a PLED pumping a photoluminescent material layer – based on MEH-PPV – located directly onto the waveguide. We addressed the advantages – in terms of coupling modes and coupled power – using an indirect PLED-to-waveguide coupling scheme. The achieved coupling efficiency into the waveguide mode is more than 31% for the indirect PL material-to-waveguide coupling, compared to 3% in the case of the direct PLED-to-waveguide coupling. The possibility to arbitrarily select the PL and the PLED materials with desired spectra represents an enormous benefit of using organic semiconductors. The possibility to in-couple the light without any alignment requirements, is also of large practical interest. Expensive in-coupling optics can be omitted in the design of potential external reader.

The out-coupling grating diffracts the guided light onto an array of polymer photodiodes acting as an integrated miniaturized spectrometer.
We optimized the P3HT:PCBM bulk heterojunction diode in terms of its photodiode (rather than photovoltaic cell) performance. We showed that, while increasing the thickness of the active layer from 70 nm to 240 nm does not significantly alter the photodiode's quantum efficiency, it results in a 10-fold decrease of the dark current. By omitting the PEDOT:PSS layer, the dark current is reduced by a factor of about 100. Furthermore, device lifetimes were also considerably increased by omitting the PEDOT:PSS layer. Conversely, a negative voltage has to be applied to maintain the EQE high. Overall, solution-processed organic photodiodes with state-of-the-art EQE of between 60 and 70% over a wide range of the visible part of the spectrum, dark current densities below 10 nA/cm^2 at -1 V, specific detectivities of 7×10^{12} $cm \cdot Hz^{1/2}/Watts$, and lifetimes above 3000 hours were demonstrated.
A spectral resolution of down to 7 nm and 5 nm was achieved with our integrated optoelectronic spectrometer, by either using a PLED, or, alternatively, an inorganic LED to pump the PL material.

Practical biosensing tests were successfully carried out using the developed organic sensing platform. Firstly, absorption tests were performed with the use of an immunoglobulin labeled

with Cy5. Secondly, a resonant system – based on SPR – was incorporated in the optical path to use our sensor as a label-free biodetection system and also to improve its sensitivity. The guided light interacted with biochemical receptors located inside a fluidic channel made of PMMA.
The immunoassay sensitivity of the absorption biosensing experiment was estimated at 333 nanomolar. The device sensitivity of the biosensor incorporating the SPR stack was estimated at $\delta\Gamma_{adv}$ = 1.2 ng/mm^2.

The work carried out in the framework of the present thesis represents an essential step toward integrated photonic systems utilizing inexpensive, rapid and low-temperature processing steps such as ink-jet printing of organic semiconductors. Such an approach opens up the way to affordable, fully integrated biosensors.
Our work represents an alternative to the non integrated in-coupling (with diode or laser) and out-coupling (with CMOS, Si-PD, photomultiplier) techniques for optical biosensors. We demonstrated that it is possible to integrate all required active and passive optical components into one miniaturized system, by making use of our simple yet powerful integration concept of organic optoelectronics devices.

Further optimization of the integrated organic spectrometer can be achieved in different ways. First, the spectral resolution can be increased to about 1 nm by either reducing the dimension of the individual PPDs or by increasing the distance between the out-coupling grating and the PPD array. Of course, in order to maintain a good signal-to-noise ratio, the guided light power could be increased by enlarging the area of the PL layer or by replacing it with a better PL material offering higher PL quantum yield.
The non-linear response of the organic spectrometer can be improved by using either a hemispherical PPD array or a chirped grating. These developments necessitate a variety of technological improvements and could become the subject of further research work. The hemispherical PPD array would mitigate the problem that the wavelength resolution depends on the angle and the wavelength, respectively. The hemispherical pixel array avoids enlargement of the pixels toward the periphery of the array. The chirped grating reduces the problem of spectral cross-talk.

The implementation of a resonant system like the SPR is useful for increasing the sensitivity, and it allows the use of label-free measurement techniques. However, the fabrication of such a system onto the high-refractive index waveguide turned out to be very demanding; in particular, the silver stack SPR system, which was originally designed to be sensitive in the green spectrum part, is challenging to manufacture. SPR stack precision requirements in terms of refractive index and thickness of each layer make it difficult to achieve a low-cost biosensor. The possibility of implementing a resonant system for example by employing a Bragg grating is preferable since it allows the simultaneous creation together with the out-coupling grating in one process step.
An additional shortcoming of the sensing platforms presented here is the weaker power intensity of the TM mode compare to the TE mode. This is detrimental for SPR methods but not for a resonant system based on a Bragg grating, which can indiscriminately work with TE or TM modes.

In summary, during this thesis, state-of-the-art PPDs with improved lifetime were developed. For the first time, light generated by PLED was in-coupled in a single-mode waveguide by evanescent scheme. The use of PL material allows to in-couple both TE and TM polarized light. Moreover, this technique enhances the in-coupled optical power dramatically. A dense array of PPDs was, for the first time, used as integrated organic spectrometer. Spectral resolution as good as $\Delta\lambda \approx 5$ nm was reached. Finally, biological absorption bio-test and use of plasmon resonant structure was demonstrated with test sensitivity of 333 nanomolar (for α-mIgG) and device sensitivity of $\delta\Gamma_{adv}$ = 1.2 ng/mm^2, respectively.
More generally, this work shows the strong potential of organic optoelectronic devices as candidates for the fabrication of totally integrated and low-cost chemical / biological sensors.

References

[1] J. Khandurina et A. Guttman, “Bioanalysis in microfluidic devices,” *Journal of Chromatography A*, vol. 943, 2002, pp. 159-183.

[2] G. Kost, *Principles & practice of point-of-care testing*, Philadelphia: Lippincott Williams & Wilkins, 2002.

[3] “Semofs WebSite: Home,” *http://www.semofs.com/*.

[4] D. Wild, *The immunoassay handbook*, Amsterdam ;;Boston: Elsevier, 2005.

[5] R. Narayanaswamy et Europt(r)ode Conference, *Optical sensors : industrial environmental and diagnostic applications [some of the contributions made at the scientific sessions of the Europt(r)ode VI Conference that was held in April 2002 in*, Berlin [u.a.]: Springer, 2004.

[6] R.F. Service, “PROTEOMICS: Searching for Recipes for Protein Chips,” *Science*, vol. 294, 2001, pp. 2080-2082.

[7] T.O. Joos, M. Schrenk, P. Hopf, K. Kroger, U. Chowdhury, D. Stol, D. Schorner, M. Durr, K. Herick, S. Rupp, K. Sohn, et H. Hammerle, “A microarray enzyme-linked immunosorbent assay for autoimmune diagnostics,” *Electrophoresis*, vol. 21, 2000, pp. 2641-2650.

[8] K. Cottier, “Label-free highly sensitive detection of (small) molecules by wavelength interrogation of integrated optical chips,” *Sensors and Actuators B: Chemical*, vol. 91, 2003, pp. 241-251.

[9] J. Homola, “Surface plasmon resonance sensors: review,” *Sensors and Actuators B: Chemical*, vol. 54, 1999, pp. 3-15.

[10] “Biacore,” *www.biacore.com/*.

[11] R. Cush, J. Cronin, W. Stewart, C. Maule, J. Molloy, et N. Goddard, “The resonant mirror: a novel optical biosensor for direct sensing of biomolecular interactions Part I: Principle of operation and associated instrumentation,” *Biosensors and Bioelectronics*, vol. 8, 1993, pp. 347-354.

[12] R. Tünnemann, M. Mehlmann, R.D. Süssmuth, B. Bühler, S. Pelzer, W. Wohlleben, H. Fiedler, K. Wiesmüller, G. Gauglitz, et G. Jung, “Optical Biosensors. Monitoring Studies of Glycopeptide Antibiotic Fermentation Using White Light Interference,” *Analytical Chemistry*, vol. 73, 2001, pp. 4313-4318.

[13] G. Ladam, P. Schaad, J.C. Voegel, P. Schaaf, G. Decher, et F. Cuisinier, “In Situ Determination of the Structural Properties of Initially Deposited Polyelectrolyte Multilayers,” *Langmuir*, vol. 16, 2000, pp. 1249-1255.

[14] R.E. Kunz, “Totally integrated optical measuring sensors,” *Proceedings of SPIE*, Boston, MA, USA: 1992, pp. 98-113.

[15] A. Sheridan, “Phase interrogation of an integrated optical SPR sensor,” *Sensors and Actuators B: Chemical*, vol. 97, 2004, pp. 114-121.

[16] “Zeptosens - Bioanalytical Solutions,” *http://www.zeptosens.com/en/*.

[17] H. Sirringhaus, N. Tessler, et R.H. Friend, “Integrated Optoelectronic Devices Based on Conjugated Polymers,” *Science*, vol. 280, 1998, pp. 1741-4.

[18] A. Dodabalapur, Z. Bao, A. Makhija, J.G. Laquindanum, V.R. Raju, Y. Feng, H.E. Katz, et J. Rogers, “Organic smart pixels,” *Applied Physics Letters*, vol. 73, 1998, pp. 142-4.

[19] S. Ohta, T. Chuman, S. Miyaguchi, H. Satoh, T. Tanabe, Y. Okuda, et M. Tsuchida, “Active Matrix Driving Organic Light-Emitting Diode Panel Using Organic Thin-Film Transistors,” *Japanese Journal of Applied Physics*, vol. 44, 2005, pp. 3678-3681.

[20] I. Nausieda, K. Ryu, I. Kymissis, A. Ibitayo (Tayo) Akinwande, V. Bulovi¿, et C.G. Sodini, "An Organic Active-Matrix Imager," *IEEE Transactions on Electron Devices*, vol. 55, 2008, pp. 527-532.

[21] T. Someya, S. Iba, Y. Kato, T. Sekitani, Y. Noguchi, Y. Murase, H. Kawaguchi, et T. Sakurai, "A large-area, flexible, and lightweight sheet image scanner integrated with organic field-effect transistors and organic photodiodes," *IEDM Technical Digest. IEEE International Electron Devices Meeting, 2004.*, San Francisco, CA, USA: , pp. 365-368.

[22] Y. Ohmori, H. Kajii, M. Kaneko, K. Yoshino, M. Ozaki, A. Fujii, M. Hikita, H. Takenaka, et T. Taneda, "Realization of Polymeric Optical Integrated Devices Utilizing Organic Light-Emitting Diodes and Photodetectors Fabricated on a Polymeric Waveguide," *IEEE Journal of Selected Topics in Quantum Electronics*, vol. 10, 2004, pp. 70-78.

[23] M. Punke, "Organic semiconductor devices for micro-optical applications," *Proceedings of SPIE*, Strasbourg, France: 2006, pp. 618505-618505-13.

[24] L. Bürgi, R. Pfeiffer, M. Mücklich, P. Metzler, M. Kiy, et C. Winnewisser, "Optical proximity and touch sensors based on monolithically integrated polymer photodiodes and polymer LEDs," *Organic Electronics*, vol. 7, 2006, pp. 114-20.

[25] V. Savvate'ev, Z. Chen-Esterlit, J.W. Aylott, B. Choudhury, C. Kim, L. Zou, J.H. Friedl, R. Shinar, J. Shinar, et R. Kopelman, "Integrated organic light-emitting device/fluorescence-based chemical sensors," *Applied Physics Letters*, vol. 81, 2002, p. 4652.

[26] O. Hofmann, P. Miller, P. Sullivan, T.S. Jones, J.C. deMello, D.D.C. Bradley, et A.J. deMello, "Thin-film organic photodiodes as integrated detectors for microscale chemiluminescence assays," *Sensors and Actuators B: Chemical*, vol. 106, 2005, pp. 878-884.

[27] J. Shinar et R. Shinar, "Organic light-emitting devices (OLEDs) and OLED-based chemical and biological sensors: an overview," *Journal of Physics D: Applied Physics*, vol. 41, 2008, p. 133001.

[28] B. Choudhury, R. Shinar, et J. Shinar, "Glucose biosensors based on organic light-emitting devices structurally integrated with a luminescent sensing element," *Journal of Applied Physics*, vol. 96, 2004, pp. 2949-54.

[29] A. Pais, A. Banerjee, D. Klotzkin, et I. Papautsky, "High-sensitivity, disposable lab-on-a-chip with thin-film organic electronics for fluorescence detection," *Lab on a Chip*, vol. 8, 2008, p. 794.

[30] A. Banerjee, A. Pais, I. Papautsky, et D. Klotzkin, "A Polarization Isolation Method for High-Sensitivity, Low-Cost On-Chip Fluorescence Detection for Microfluidic Lab-on-a-Chip," *IEEE Sensors Journal*, vol. 8, 2008, pp. 621-627.

[31] R. Shinar, D. Ghosh, B. Choudhury, M. Noack, V. Dalal, et J. Shinar, "Luminescence-based oxygen sensor structurally integrated with an organic light-emitting device excitation source and an amorphous Si-based photodetector," *Journal of Non-Crystalline Solids*, vol. 352, 2006, pp. 1995-1998.

[32] K. Shin, Y. Kim, K. Paek, J. Park, E. Yang, T. Kim, J. Kang, et B. Ju, "Characterization of an Integrated Fluorescence-Detection Hybrid Device With Photodiode and Organic Light-Emitting Diode," *IEEE Electron Device Letters*, vol. 27, 2006, p. 746.

[33] O. Hofmann, X. Wang, J.C. deMello, D.D.C. Bradley, et A.J. deMello, "Towards microalbuminuria determination on a disposable diagnostic microchip with integrated fluorescence detection based on thin-film organic light emitting diodes," *Lab on a Chip*, vol. 5, 2005, p. 863.

[34] J.B. Edel, N.P. Beard, O. Hofmann, J.C. deMello, D.D.C. Bradley, et A.J. deMello, “Thin-film polymer light emitting diodes as integrated excitation sources for microscale capillary electrophoresis,” *Lab on a Chip*, vol. 4, 2004, pp. 136-40.
[35] “Bioident Technologies, Inc..”
[36] R. Pieler, E. Füreder, et M. Sonnleitner, “Printed photonics for lab-on-chip applications,” *Proceedings of SPIE*, Florence, Italy: 2007, pp. 673919-673919-8.
[37] M. Pope, H. Kallmann, et P. Magnante, “Electroluminescence in organic crystals,” *The Journal of Chemical Physics*, vol. 38, 1963, pp. 2042-3.
[38] W. Helfrich et W.G. Schneider, “Recombination radiation in anthracene crystals,” *Physical Review Letters*, vol. 14, 1965, p. 229.
[39] C.W. Tang, “Two-layer organic photovoltaic cell,” *Applied Physics Letters*, vol. 48, 1986, pp. 183-5.
[40] C.W. Tang et S.A. Van Slyke, “Organic electroluminescent diodes,” *Applied Physics Letters*, vol. 51, 1987, pp. 913-5.
[41] J.H. Burroughes, D.D.C. Bradley, A.R. Brown, R.N. Marks, K. Mackay, R.H. Friend, P.L. Burns, et A.B. Holmes, “Light-emitting diodes based on conjugated polymers,” *Nature*, vol. 347, 1990, pp. 539-41.
[42] R.H. Friend, J. Burroughes, et D.D.C. Bradley, “Electroluminescent devices,” U.S. Patent WO 90/13148.
[43] M. Kiy, “Charge injection and transport in organic semiconductors,” ETHZ, 2002.
[44] J. Shinar, *Organic Light-Emitting Devices: A Survey*, New York: Shinar, J., 2004.
[45] P.V. Pesavento, R.J. Chesterfield, C.R. Newman, et C.D. Frisbie, “Gated four-probe measurements on pentacene thin-film transistors: Contact resistance as a function of gate voltage and temperature,” *Journal of Applied Physics*, vol. 96, Déc. 2004, pp. 7312-7324.
[46] V. Podzorov, E. Menard, A. Borissov, V. Kiryukhin, J.A. Rogers, et M.E. Gershenson, “Intrinsic Charge Transport on the Surface of Organic Semiconductors,” *Physical Review Letters*, vol. 93, 2004.
[47] U. Lemmer, M. Scheidler, R. Kersting, R. Mahrt, H. Kurz, H. Bässler, E. Göbel, et P. Thomas, “Hopping Dynamics of Photoexcitations in Conjugated Polymers,” 1995.
[48] A. Miller et E. Abrahams, “Impurity Conduction at Low Concentrations,” *Physical Review*, vol. 120, 1960, pp. 745-755.
[49] V.I. Arkhipov, E.V. Emelianova, Y.H. Tak, et H. Bässler, “Charge injection into light-emitting diodes: Theory and experiment,” *Journal of Applied Physics*, vol. 84, 1998, pp. 848-56.
[50] S. Barth, U. Wolf, et H. Bässler, “Current injection from a metal to a disordered hopping system. III. Comparison between experiment and Monte Carlo simulation,” *Physical Review B*, vol. 60, 1999, pp. 8791-8797.
[51] A.J. Campbell, D.D.C. Bradley, et D.G. Lidzey, “Space-charge limited conduction with traps in poly(phenylene vinylene) light emitting diodes,” *Journal of Applied Physics*, vol. 82, 1997, pp. 6326-42.
[52] U. Wolf, V.I. Arkhipov, et H. Bässler, “Current injection from a metal to a disordered hopping system. I. Monte Carlo simulation,” *Physical Review B*, vol. 59, 1999, pp. 7507-13.
[53] M. Matsumura, T. Akai, M. Saito, et T. Kimura, “Height of the energy barrier existing between cathodes and hydroxyquinoline–aluminum complex of organic electroluminescence devices,” *Journal of Applied Physics*, vol. 79, 1996, p. 264.
[54] H.N. Cho, J.K. Kim, D.Y. Kim, C.Y. Kim, N.W. Song, et D. Kim, “Statistical Copolymers for Blue-Light-Emitting Diodes,” *Macromolecules*, vol. 32, 1999, pp. 1476-1481.

[55] L. Bozano, S.A. Carter, J.C. Scott, G.G. Malliaras, et P.J. Brock, “Temperature- and Field-dependent electron and hole mobilities in polymer light-emitting diodes,” *Applied Physics Letters*, vol. 74, 1999, pp. 1132-4.
[56] P.W.M. Blom, M.J.M. de Jong, et J.J.M. Vleggaar, “Electron and hole transport in poly(p-phenylene vinylene) devices,” *Applied Physics Letters*, vol. 68, 1996, p. 3308.
[57] “universaldisplay,” *www.universaldisplay.com*.
[58] N. Ide, T. Komoda, et J. Kido, “Organic light-emitting diode (OLED) and its application to lighting devices,” *Proceedings of SPIE*, San Diego, CA, USA: 2006, pp. 63330M-63330M-10.
[59] R. Meerheim, K. Walzer, M. Pfeiffer, et K. Leo, “Ultrastable and efficient red organic light emitting diodes with doped transport layers,” *Applied Physics Letters*, vol. 89, 2006, p. 061111.
[60] N. Tessler, N.T. Harrison, et R.H. Friend, “High Peak Brightness Polymer Light-Emitting Diodes,” *Adv. Mater.*, vol. 74, p. 64.
[61] R.F. Service, “ELECTRONICS: Organic LEDs Look Forward to a Bright, White Future,” *Science*, vol. 310, 2005, pp. 1762-1763.
[62] C. Adachi, M.A. Baldo, M.E. Thompson, et S.R. Forrest, “Nearly 100% internal phosphorescence efficiency in an organic light emitting device,” *Journal of Applied Physics*, vol. 90, 2001, pp. 5048-51.
[63] P. van Hal, “Full temporal resolution of the two-step photoinduced energy–electron transfer in a fullerene–oligothiophene–fullerene triad using sub-10 fs pump–probe spectroscopy,” *Chemical Physics Letters*, vol. 345, 2001, pp. 33-38.
[64] N. Sariciftci, “Role of Buckminsterfullerene, C60, in organic photoelectric devices,” *Progress in Quantum Electronics*, vol. 19, 1995, pp. 131-159.
[65] P. Peumans, A. Yakimov, et S.R. Forrest, “Small molecular weight organic thin-film photodetectors and solar cells,” *Journal of Applied Physics*, vol. 93, 2003, p. 3693.
[66] P. Peumans, A. Yakimov, et S.R. Forrest, “Erratum: "Small molecular weight organic thin-film photodetectors and solar cells" [J. Appl. Phys. 93, 3693 (2003)],” *Journal of Applied Physics*, vol. 95, 2004, p. 2938.
[67] H. Hoppe et N.S. Sariciftci, “Organic solar cells: An overview,” *Journal of Materials Research*, vol. 19, 2004, pp. 1924-1945.
[68] G. Yu, J. Gao, J.C. Hummelen, F. Wudl, et A.J. Heeger, “Polymer Photovoltaic Cells: Enhanced Efficiencies via a Network of Internal Donor-Acceptor Heterojunctions,” *Science*, vol. 270, 1995, pp. 1789-1791.
[69] S.E. Shaheen, R. Radspinner, N. Peyghambarian, et G.E. Jabbour, “Fabrication of bulk heterojunction plastic solar cells by screen printing,” *Applied Physics Letters*, vol. 79, 2001, p. 2996.
[70] S.E. Shaheen, C.J. Brabec, N.S. Sariciftci, F. Padinger, T. Fromherz, et J.C. Hummelen, “2.5% efficient organic plastic solar cells,” *Applied Physics Letters*, vol. 78, 2001, p. 841.
[71] T. Aernouts, “Extraction of bulk and contact components of the series resistance in organic bulk donor-acceptor-heterojunctions,” *Thin Solid Films*, vol. 403-404, 2002, pp. 297-301.
[72] P. Schilinsky, C. Waldauf, et C.J. Brabec, “Recombination and loss analysis in polythiophene based bulk heterojunction photodetectors,” *Applied Physics Letters*, vol. 81, 2002, p. 3885.
[73] F. Padinger, R. Rittberger, et N. Sariciftci, “Effects of Postproduction Treatment on Plastic Solar Cells,” *Advanced Functional Materials*, vol. 13, 2003, pp. 85-88.
[74] J. Drechsel, B. Männig, F. Kozlowski, D.G.A. Werner, M. Koch, K. Leo, et M. Pfeiffer, “High efficiency organic solar cells based on single or multiple PIN structures,” *Thin Solid Films*, vol. 451, 2004, pp. 515-7.

[75] G. Li, V. Shrotriya, J. Huang, Y. Yao, T. Moriarty, K. Emery, et Y. Yang, "High-efficiency solution processable polymer photovoltaic cells by self-organization of polymer blends," *Nature Materials*, vol. 4, 2005, pp. 864-868.
[76] J. Kim, S. Kim, H. Lee, K. Lee, W. Ma, X. Gong, et A. Heeger, "New Architecture for High-Efficiency Polymer Photovoltaic Cells Using Solution-Based Titanium Oxide as an Optical Spacer," *Advanced Materials*, vol. 18, 2006, pp. 572-576.
[77] M.M. Wienk, M. Turbiez, J. Gilot, et R.A.J. Janssen, "Narrow-Bandgap Diketo-Pyrrolo-Pyrrole Polymer Solar Cells: The Effect of Processing on the Performance," *Advanced Materials*, vol. 20, 2008, pp. 2556-2560.
[78] J. Peet, J.Y. Kim, N.E. Coates, W.L. Ma, D. Moses, A.J. Heeger, et G.C. Bazan, "Efficiency enhancement in low-bandgap polymer solar cells by processing with alkane dithiols," *Nature Materials*, vol. 6, 2007, pp. 497-500.
[79] S.H. Park, A. Roy, S. Beaupré, S. Cho, N. Coates, J.S. Moon, D. Moses, M. Leclerc, K. Lee, et A.J. Heeger, "Bulk heterojunction solar cells with internal quantum efficiency approaching 100%," *Nature Photonics*, vol. 3, 2009, pp. 297-302.
[80] D. Lozofsky, "Challenges of Transforming a Research Product into a Commercial Product," 2009.
[81] Wu, "Solarmer."
[82] B.P. Rand, J. Li, J. Xue, R.J. Holmes, M.E. Thompson, et S.R. Forrest, "Organic Double-Heterostructure Photovoltaic Cells Employing Thick Tris(acetylacetonato)ruthenium(III) Exciton-Blocking Layers," *Advanced Materials*, vol. 17, 2005, pp. 2714-2718.
[83] D. Chirvase, J. Parisi, J.C. Hummelen, et V. Dyakonov, "Influence of nanomorphology on the photovoltaic action of polymer–fullerene composites," *Nanotechnology*, vol. 15, 2004, pp. 1317-1323.
[84] N.S. Sariciftci, L. Smilowitz, A.J. Heeger, et F. Wudl, "Photoinduced Electron Transfer from a Conducting Polymer to Buckminsterfullerene," *Science*, vol. 258, 1992, pp. 1474-1476.
[85] S. Sze, *Semiconductor devices, physics and technology*, New York: Wiley, 1985.
[86] V. Bulovic, "Study of localized and extended excitons in 3,4,9,10-perylenetetracarboxylic dianhydride (PTCDA) II. Photocurrent response at low electric fields," *Chemical Physics*, vol. 210, 1996, pp. 13-25.
[87] J. Huang, G. Li, et Y. Yang, "Influence of composition and heat-treatment on the charge transport properties of poly(3-hexylthiophene) and [6,6]-phenyl C[sub 61]-butyric acid methyl ester blends," *Applied Physics Letters*, vol. 87, 2005, p. 112105.
[88] F. Ligler, *Optical biosensors : today and tomorrow*, Amsterdam ;;Boston: Elsevier, 2008.
[89] T. Vo-Dinh et B. Cullum, "Biosensors and biochips: advances in biological and medical diagnostics," *Fresenius' Journal of Analytical Chemistry*, vol. 366, 2000, pp. 540-551.
[90] X. Fan, I. White, S. Shopova, H. Zhu, J. Suter, et Y. Sun, "Sensitive optical biosensors for unlabeled targets: A review," *Analytica Chimica Acta*, vol. 620, 2008, pp. 8-26.
[91] K. Schmitt, K. Oehse, G. Sulz, et C. Hoffmann, "Evanescent field Sensors Based on Tantalum Pentoxide Waveguides – A Review," *Sensors*, vol. 8, 2008, pp. 711-738.
[92] B. Lu, C. Lu, et Y. Wei, "A planar quartz waveguide immunosensor based on TIRE principle," *Anal. Lett.*, vol. 25.
[93] G. Duveneck, D. Neuschafer, et M. Ehrat, "Process for detecting evanescently excited luminescence," U.S. Patent 21/77,21/64.
[94] A.N. Asanov, W.W. Wilson, et P.B. Oldham, "Regenerable Biosensor Platform: A Total Internal Reflection Fluorescence Cell with Electrochemical Control," *Analytical Chemistry*, vol. 70, 1998, pp. 1156-1163.

[95] T.E. Plowman, J.D. Durstchi, H.K. Wang, D.A. Christensen, J.N. Herron, et W.M. Reichert, "Multiple-Analyte Fluoroimmunoassay Using an Integrated Optical Waveguide Sensor," *Analytical Chemistry*, vol. 71, 1999, pp. 4344-4352.
[96] G. Duveneck, M. Pawlak, D. Neuschafer, E. Bar, W. Budach, U. Pieles, et M. Ehrat, "Novel bioaffinity sensors for trace analysis based on luminescence excitation by planar waveguides," *Sensors and Actuators B: Chemical*, vol. 38, 1997, pp. 88-95.
[97] A. Brecht, "Optical immunoprobe development for multiresidue monitoring in water," *Analytica Chimica Acta*, vol. 362, 1998, pp. 69-79.
[98] K.R. Rogers, "Principles of Affinity-Based Biosensors," *Molecular Biotechnology*, vol. 14, 2000, pp. 109-130.
[99] "Invitrogen.com a Provider of Essential Life Science Technologies," *http://www.invitrogen.com/site/us/en/home.html*.
[100] R. Ulbrich, R. Golbik, et A. Schellenberger, "Protein adsorption and leakage in carrier-enzyme systems," *Biotechnology and Bioengineering*, vol. 37, 1991, pp. 280-287.
[101] S. Bhatia, L. Shriverlake, K. Prior, J. Georger, J. Calvert, R. Bredehorst, et F. Ligler, "Use of thiol-terminal silanes and heterobifunctional crosslinkers for immobilization of antibodies on silica surfaces," *Analytical Biochemistry*, vol. 178, 1989, pp. 408-413.
[102] F.S. Ligler, K.E. Sapsford, J.P. Golden, L.C. Shriver-Lake, C.R. Taitt, M.A. Dyer, S. Barone, et C.J. Myatt, "The Array Biosensor: Portable, Automated Systems," *Analytical Sciences*, vol. 23, 2007, pp. 5-10.
[103] J. Gordonii et S. Ernst, "Surface plasmons as a probe of the electrochemical interface," *Surface Science*, vol. 101, 1980, pp. 499-506.
[104] C. Nylander, B. Liedberg, et T. Lind, "Gas detection by means of surface plasmon resonance," *Sensors and Actuators*, vol. 3, 1982, pp. 79-88.
[105] B. Oh, "Immunosensor for detection of Legionella pneumophila using surface plasmon resonance," *Biosensors and Bioelectronics*, vol. 18, 2003, pp. 605-611.
[106] M. Shimomura, "Simple and rapid detection method using surface plasmon resonance for dioxins, polychlorinated biphenylx and atrazine," *Analytica Chimica Acta*, vol. 434, 2001, pp. 223-230.
[107] M. Minunni et M. Mascini, "Detection of Pesticide in Drinking Water Using Real-Time Biospecific Interaction Analysis (BIA)," *Analytical Letters*, vol. 26, p. 1441.
[108] C. Mouvet, "Determination of simazine in water samples by waveguide surface plasmon resonance," *Analytica Chimica Acta*, vol. 338, 1997, pp. 109-117.
[109] J.R. Sambles, G.W. Bradbery, et F. Yang, "Optical excitation of surface plasmons: An introduction," *Contemporary Physics*, vol. 32, 1991, pp. 173-183.
[110] W.L. Barnes, A. Dereux, et T.W. Ebbesen, "Surface plasmon subwavelength optics," *Nature*, vol. 424, 2003, pp. 824-830.
[111] M. Cooper, *Label-free biosensors : techniques and applications*, Cambridge ;;New York: Cambridge University Press, 2009.
[112] A.M. Armani, R.P. Kulkarni, S.E. Fraser, R.C. Flagan, et K.J. Vahala, "Label-Free, Single-Molecule Detection with Optical Microcavities," *Science*, vol. 317, 2007, pp. 783-787.
[113] N.L. Anderson, "The Human Plasma Proteome: History, Character, and Diagnostic Prospects," *Molecular & Cellular Proteomics*, vol. 1, 2002, pp. 845-867.
[114] J.P. Smith, "Medical and biological sensors: a technical and commercial review," *Sensor Review*, vol. 25, 2005, pp. 241-245.
[115] D. Thévenot, "Electrochemical biosensors: recommended definitions and classification," *Biosensors and Bioelectronics*, vol. 16, 2001, pp. 121-131.
[116] M. Ramuz, L. Bürgi, R. Stanley, et C. Winnewisser, "Coupling light from an organic light emitting diode (OLED) into a single-mode waveguide: Toward monolithically integrated optical sensors," *Journal of Applied Physics*, vol. 105, 2009, p. 084508.

[117] H. Benisty, R. Stanley, et M. Mayer, “Method of source terms for dipole emission modification in modes of arbitrary planar structures,” *Journal of the Optical Society of America A*, vol. 15, 1998, p. 1192.
[118] M. Born, *Principles of optics electromagnetic theory of propagation, interference, and diffraction of light*,, Oxford ;New York: Pergamon Press, 1975.
[119] R.R. Chance,, A. Prock, et R. Silbey, “Molecular Fluorescence and Energy Transfer Near Interfaces,” *Advances in Chemical Physics*, New York: I. Prigogine, Stuart A. Rice, .
[120] R.R. Chance, “Lifetime of an emitting molecule near a partially reflecting surface,” *The Journal of Chemical Physics*, vol. 60, 1974, p. 2744.
[121] G. Ford, “Electromagnetic interactions of molecules with metal surfaces,” *Physics Reports*, vol. 113, 1984, pp. 195-287.
[122] W. Lukosz, “Theory of optical-environment-dependent spontaneous-emission rates for emitters in thin layers,” *Physical Review B*, vol. 22, 1980, pp. 3030-3038.
[123] W. Lukosz et R.E. Kunz, “Light emission by magnetic and electric dipoles close to a plane interface I Total radiated power,” *Journal of the Optical Society of America*, vol. 67, 1977, p. 1607.
[124] W. Lukosz, “Light emission by magnetic and electric dipoles close to a plane dielectric interface. III. Radiation patterns of dipoles with arbitrary orientation,” *Journal of the Optical Society of America*, vol. 69, pp. 1495-1503.
[125] W. Lukosz, “Light emission by multipole sources in thin layers I Radiation patterns of electric and magnetic dipoles,” *Journal of the Optical Society of America*, vol. 71, 1981, p. 744.
[126] R.E. Kunz et W. Lukosz, “Changes in fluorescence lifetimes induced by variable optical environments,” *Physical Review B*, vol. 21, 1980, pp. 4814-4828.
[127] W.H. Weber, “Enhanced Raman Scattering by Adsorbates Including the Nonlocal Response of the Metal and the Excitation of Nonradiative Modes,” *Physical Review Letters*, vol. 44, 1980, pp. 1774-1777.
[128] H. De Neve, J. Blondelle, R. Baets, P. Demeester, P. Van Daele, et G. Borghs, “High efficiency planar microcavity LED's: comparison of design and experiment,” *IEEE Photonics Technology Letters*, vol. 7, 1995, pp. 287-289.
[129] “Fluxim,” *http://www.fluxim.com/*.
[130] “Microdrop Technologies GmbH - Advancing the Art of Microdispensing,” *http://www.microdrop.de/*.
[131] E. Tekin, B.D. Gans, et U.S. Schubert, “Ink-jet printing of polymers — from single dots to thin film libraries,” *Journal of Materials Chemistry*, vol. 14, 2004, pp. 2627-32.
[132] M. Erwin, “Effects of impurities on the optical properties of poly-3-hexylthiophene thin films,” *Thin Solid Films*, vol. 409, 2002, pp. 198-205.
[133] Z. Kafafi et Society of Photo-optical Instrumentation Engineers., *Organic photovoltaics IV : 7-8 August, 2003, San Diego, California, USA*, Bellingham Wash.: SPIE, 2004.
[134] E.J. Meijer, D.M. De Leeuw, S. Setayesh, E.V. Veenendaal, B.-. Huisman, P.W.M. Blom, J.C. Hummelen, U. Scherf, et T.M. Klapwijk, “Solution-processed ambipolar organic field-effect transistors and inverters,” *Nature Materials*, vol. 2, 2003, pp. 678-682.
[135] H. Sirringhaus, N. Tessler, et R. Friend, “Integrated, high-mobility polymer field-effect transistors driving polymer light-emitting diodes,” *Synthetic Metals*, vol. 102, 1999, pp. 857-860.
[136] H. Mao, B. Xu, et S. Holdcroft, “Synthesis and structure-property relationships of regioirregular poly(3-hexylthiophenes),” *Macromolecules*, vol. 26, 1993, pp. 1163-1169.

[137] B. Kramer, *Advances in Solid State Physics 39*, Berlin, Heidelberg: Springer Berlin Heidelberg, 1999.
[138] S. Lu, S. Sun, X. Jiang, J. Mao, T. Li, et K. Wan, "In situ 3-hexylthiophene polymerization onto surface of TiO2 based hybrid solar cells," *Journal of Materials Science: Materials in Electronics*, 2009.
[139] U. Zhokhavets, T. Erb, G. Gobsch, M. Alibrahim, et O. Ambacher, "Relation between absorption and crystallinity of poly(3-hexylthiophene)/fullerene films for plastic solar cells," *Chemical Physics Letters*, vol. 418, 2006, pp. 347-350.
[140] V. Mihailetchi, J. van Duren, P. Blom, J. Hummelen, R. Janssen, J. Kroon, M. Rispens, W. Verhees, et M. Wienk, "Electron Transport in a Methanofullerene," *Advanced Functional Materials*, vol. 13, 2003, pp. 43-46.
[141] "American Dye Source, Inc. - Providing Innovative Materials to the World," *http://www.adsdyes.com/*.
[142] "Ocean Optics - Smart, Innovative, Flexible, Solvers," *http://www.oceanoptics.com/*.
[143] "Hamamatsu Photonics," *http://www.hamamatsu.com/*.
[144] M. Ramuz, L. Burgi, C. Winnewisser, et P. Seitz, "High sensitivity organic photodiodes with low dark currents and increased lifetimes," *Organic Electronics*, vol. 9, 2008, pp. 369-376.
[145] Y. Lin, C. Cheng, H. Liao, S. Horng, H. Meng, et C. Hsu, "Integration of polymer light-emitting diode and polymer waveguide on Si substrate," *Applied Physics Letters*, vol. 89, 2006, p. 063501.
[146] M.C. Gather, F. Ventsch, et K. Meerholz, "Embedding Organic Light-Emitting Diodes into Channel Waveguide Structures," *Advanced Materials*, vol. 20, 2008, pp. 1966-1971.
[147] M. Lu et J.C. Sturm, "Optimization of external coupling and light emission in organic light-emitting devices: modeling and experiment," *Journal of Applied Physics*, vol. 91, 2002, p. 595.
[148] J. Duebendorfer, "Sensing and reference pads for integrated optical immunosensors," *Journal of Biomedical Optics*, vol. 2, 1997, p. 391.

List of publications and patents

1. Scientific journals

"**High sensitivity organic photodiodes with low dark currents and increased lifetimes**" Marc Ramuz, Lukas Bürgi, Carsten Winnewisser and Peter Seitz, *Organic Electronics* 9, 369–376 (2008)

"**Coupling light from an organic light emitting diode (OLED) into a single-mode waveguide: Toward monolithically integrated optical sensors**" Marc Ramuz, Lukas Bürgi, Ross Stanley and Carsten Winnewisser, *Journal of Applied Physics* 105, 1 (2009)

"OLED and OPD-based mini-spectrometer integrated on a single-mode planar waveguide chip" Marc Ramuz, David Leuenberger, Reto Pfeiffer, Lukas Bürgi and Carsten Winnewisser, *European Physical Journal Applied Physic* 46, (2009)

Paper submitted to Journals:

"Optical biosensors based on integrated polymer light source and polymer photodiode", Marc Ramuz, David Leuenberger and Lukas Bürgi, *Advanced Functional Materials*

2. Book chapter

"**The Microflow Cytometer**", David Leuenberger and Marc Ramuz, Editors J. S. Kim and F. S. Ligler, *PanStanford Publishing*, (2009)

3. Patents

"**Light coupling device and system, and method for manufacturing the device and system**", Marc Ramuz, David Leuenberger, Lukas Bürgi, Carsten Winnewisser and Ross P. Stanley, *US Patent Application*: US 09163266.1 and *European Patent Application*: EP 09163266.1